Quantum Chemical Investigation of the Interaction of Hydrogen with Solid Surfaces

Dissertation

Zur Erlangung des akademischen Grades
Doctor rerum naturalium (Dr. rer. nat.)

im Fach Chemie

eingereicht an der

Mathematisch-Naturwissenschaftlichen Fakultät der Humboldt-Universität zu Berlin

von

Herrn Thomas Mullan, M.Sc.

Präsident der Humboldt-Universität zu Berlin
Prof. Dr. Peter Frensch (Kommisarisch)

Dekan der Mathematisch-Naturwissenschaftlichen Fakultät
Prof. Dr. Elmar Kulke

Gutachter:
1. PD Dr. Denis Usvyat
2. Prof. Dr. Hans-Joachim Freund
3. Prof. Dr. Bernd Meyer

Tag der mündlichen Prüfung: 8.6.2022

Eigenständigkeitserklärung

Ich erkläre hiermit, dass ich die Dissertation selbständig und nur unter Verwendung der von mir angegebenen Hilfsmittel gemäß §7 Abs. 3 der Promotionsordnung der Mathematisch-Naturwissenschaftlichen Fakultät, veröffentlicht am 11.07.2018 im amtlichen Mitteilungsblatt der Humboldt-Universität zu Berlin № 42/2018, angefertigt habe.

Berlin, den _____ _____

(Thomas Mullan)

Nothing in life is to be feared, it is only to be understood.
Now is the time to understand more, so that we may fear less.

Marie Curie

Abstract

The present thesis aims at investigating the interactions of hydrogen with solid surfaces and materials. We first offer a brief historical context for surface science, as well as quantum mechanics and science is general, before deriving the mathematical apparatus necessary to investigate our systems of interest. We then move on to explore the potential energy surface of the water-formation-reaction on a partially oxidized ruthenium(0001) surface when confined under a two-atom thick sheet of silica (SiO_2). We further employ our findings in conjunction with experimental observations and mathematical modeling to set up a fully theoretical model of the system in order to explain its behavior. In the second chapter we investigate the chemical alteration of the ultra-thin silica bilayer by means of exposing it to hydrogen plasma. We elucidate possible defects formed during the process and pin-point the most likely structure found. In the last chapter, we investigate the possible error sources that are inherent in quantum mechanical modeling and employ the so called embedded fragment approach to lift the approximations up to the coupled cluster singles and doubles with perturbative triples (CCSD(T)) level of theory. We then apply this methodology to the diffusion of hydrogen on aluminum oxide to obtain a diffusion barrier of chemical accuracy that may both be used to benchmark other approaches such as density functional theory, as well as experimental findings.

Zusammenfassung

In dieser Arbeit werden die Wechselwirkungen von Wasserstoff mit festen Materialien und Oberflächen untersucht. Zunächst wird der Kontext unserer Untersuchung durch eine kurze Einordnung in die Geschichte der Naturwissenschaften im Allgemeinen, und der Oberflächenforschung im Speziellen, hergestellt. Anschließend wird der quantenmechanische Apparat, welcher nötig ist um die betrachteten Systeme zu beschreiben, eingeführt um dann detailliert die Potentialhyperfläche der Entstehung von Wasser durch Adsoprtion von Wasserstoff auf einer teilweise oxidierten Ruthenium(0001) Metalloberfläche zu studieren. Zudem wird das gleiche System betrachtet, wenn die Metalloberfläche zusätzlich von einer biatomaren, kristallinen Lage Siliziumdioxid (SiO_2) bedeckt ist, wodurch eine räumliche Beengung eintritt. Wir verwenden unsere Ergebnisse zusammen mit experimentellen Beobachtungen und mathematischen Methoden um ein vollständig theoretisches Modell zu entwerfen und das System grundlegend verstehen zu können. In einem weiteren Schritt werden die chemischen Änderungen der Siliziumdioxid Doppellage untersucht, wenn das System Wasserstoffplasma ausgesetzt wird. Es werden diverse mögliche Defektstrukturen diskutiert und mithilfe experimenteller Befunde die wahrscheinlichste Struktur isoliert. Im letzten Kapitel werden die typischen Näherungen untersucht, welche notwendig sind um quantenmechanische Methoden mit Hilfe von Computern durchführbar zu machen. Wir verwenden den sogenannten embedded-fragment Ansatz um die Diffusionsbarriere von Wasserstoff auf Aluminiumoxid mit chemischer Genauigkeit zu berechnen. Unsere Ergebnisse auf dem coupled-cluster with singles, doubles and perturbative triples (CCSD(T))-Niveau können sowohl als Referenz für experimentelle Untersuchungen, als auch für andere quantenmechanische Methoden wie z.B. die Dichtefunktionaltheorie, angesehen werden.

Acknowledgements

The completion of this thesis would not have been possible without the help and encouragement of many people.

I would like to first mention Prof. Dr. Martin Schütz, who sadly passed away shortly after I began my research activities in his group. Without him I would not have had the same scientific opportunities.

Next, I would like to thank my supervisor Dr. Denis Usvyat, who managed to do an exceptional job in taking over the duties after Prof. Schütz was no longer with us. His way of conducting research and interacting with students and other people encouraged me to continuously improve on my own work and ask many questions.

Of course, I owe thanks to my parents, who made it possible for me to study chemistry in the first place and pursue my interest in science.

Many thanks are also due to the entire group of Dr. Usvyat and also the groups of Dr. Bischoff and Prof. Sauer, with which I had many lively and inspiring discussions. In particular, I would like to thank Dr. Evelin Christlmaier, Ernst-Christian Flach and Alexander Krach for proofreading this manuscript.

Furthermore, I would like to thank Prof. Dr. Bernd Meyer from the Interdisciplinary Center for Molecular Materials (ICMM) of the University Erlangen/Nuremberg for first of all providing me with the scientific foundation during my master's thesis, as well as for providing the pseudopotentials and the optimized ruthenium crystal structure that were used in this thesis. In addition to Prof. Meyer, I would also like to thank Prof. Görling from the Friedrich-Alexander University Erlangen/Nuremberg, whose excellent lecture scripts on quantum chemistry were of great help at many points.

I would also like to extend my gratitude towards Dr. Mauricio Prieto, Dr. Thomas Schmidt and Prof. Dr. Hans-Joachim Freund from the Fritz Haber Institute of the Max Planck Society Berlin, as well as Dr. Mark Schlutow of the Freie Universität Berlin and Prof. Dr. Joachim Sauer of the Humboldt University Berlin for the close and fruitful collaboration that made large parts of this thesis possible.

Special thanks are dedicated to Erik Jäger, whose exceptional personality and friendship I very much cherish and to whom I owe many thanks for continuously proofreading manuscripts.

I would also like to show appreciation for an army of dedicated people providing a myriad of freely available open source programs and tools. While not possible to name all of them, I would in particular like to mention the LaTeX package and all of its many extensions, in particular the Ti*k*Z and PGF package by Till Tantau and Christian Feuersänger, which was used extensively in this thesis. Furthermore, I would like to mention the VIPSTER program for visualization and editing of molecular and periodic structures created by Sebastian Gsänger which was used to obtain the molecular graphics in this thesis.

Lastly, I would like to thank all those whose name I did not explicitly mention but who deserve credit in one way or another. Please forgive me for not being able to remember everyone.

Contents

List of Abbreviations

AO ..... Atomic Orbital
a.u. ..... Arbitrary Unit, Atomic Unit
BE ..... Binding Energy
CC ..... Coupled Cluster
CI ..... Configuration Interaction
DFT ..... Density Functional Theory
FC ..... Frozen Core
GGA ..... Generalized Gradient Approximation
GTO ..... Gaussian Type Orbital
HF ..... Hartree-Fock
HREELS ..... High Resolution Electron Energy Loss Spectroscopy
IR ..... Infrared
IRAS ..... Infrared Reflection Absorption Spectroscopy
LCAO ..... Linear Combination of Atomic Orbitals
LDA ..... Local Density Approximation
LEED ..... Low-Energy Electron Diffraction
LEEM ..... Low-Energy Electron Microscopy
MEP ..... Minimum Energy Pathway
ML ..... Monolayer
MOF ..... Metal-Organic Framework
MP ..... Møller-Plesset
NEB ..... Nudged Elastic Band
NMR ..... Nuclear Magnetic Resonance
OSV ..... Orbital Specific Virtual
PAO ..... Projected Atomic Orbital
PBE ..... Perdew-Burke-Ernzerhof
PES ..... Potential Energy Surface
POSS ..... Polyhedral Oligomeric Silsesquioxane
PTO ..... Poisson Type Orbital
RDS ..... Rate-Determining Step
RPA ..... Random Phase Approximation
SD ..... Slater Determinant
SIE ..... Self-Interaction Error
STO ..... Slater Type Orbital
TON ..... Turnover Number
TS ..... Transition State
UHV ..... Ultra-High Vacuum
WF ..... Wannier Function
WFR ..... Water-Formation-Reaction
XPS ..... X-Ray Photoelectron Spectroscopy

1 Chemistry and Surface Science in a Brief Historical Context

For as long as humanity existed, mankind has marveled at nature and the universe and wondered at the existence of life. While there seems to be an infinite number of inexplicable phenomena in the universe, there ought to be as many attempts at explaining them. The roots of science as a means to establish new knowledge can be traced back to the ancient Egyptian and Mesopotamian era, dating as far back as 2500 BCE.[1] This included, amongst other things, early forms of mathematics, book keeping, geometry, calendars and astronomy.[1,2] Many of the philosophical and mathematical foundations of our modern understanding of science were pioneered by the ancient Greeks, such as Thales of Miletus (c. 640 – c. 546 BCE), credited as the founder of the ionian school of philosophy, Pythagoras of Samos (c. 570 – c. 495 BCE) or Leucippus (5^{th} century BCE) who introduced the concept of the atom as the indivisible constituents that make up the world and many others.

The modern definition of a scientific theory is usually understood in terms of physical laws, which are deduced from reproducible experimental observations. A scientific theory therefore aims for the mathematical explanation of all known observations and the prediction of new physical laws based on these facts, which in turn can then be falsified by experiment.[3]

Initially, there was no clear distinction between the field of natural sciences as we know them today, such as physics, chemistry, biology or mathematics and the first scholars we associate with the advent of modern scientific methods were often skilled in a wide variety of fields. Starting with Nicolaus Copernicus (1546 – 1601), who was the first to advocate – facing great oppression – a heliocentric view of the solar system and continuing with famous names such as Galileo Galilee (1564 – 1642), who established the concepts of velocity and acceleration and discovered the first moons of Jupiter as well as Saturn's rings, or Johannes Kepler (1571 – 1630) who dared for the first time to deviate from a perfect circle and predicted

the planetary motion to be elliptic, with the sun in one of their focal points. The work of these and many other natural philosophers and mathematicians of the time culminated in Sir Isaac Newton's (1642 – 1726/27*) famous work *Philosophiæ Naturalis Principia Mathematica* (first published July 1687) establishing the laws of classical mechanics.

The great struggles with which these early scientist had to wrestle (and still wrestle today) is beautifully exemplified in the words of Stevin, who introduced the decimal fraction in his work *La Disme* (1585) beginning with the words[5–7]

> *"To all astronomers, surveyors, measurers of tapestry, barrels and other things, to all mintmasters and merchants, good luck!"*

In parallel to the quest for the mathematical description of the universe, attempts were also made at elucidating the building blocks of matter. The changes in sociological structures as society shifted from a feudalistic system to one driven by industrialists and capitalism meant, new social classes emerged such as the working class and the artisans.[6] As a consequence, large amounts of effort were redistributed into optimizing production and illuminating properties of new materials and soon, the mysterious aura that enrobed medieval alchemists was replaced by scientific principles when Sir Francis Bacon (1561 – 1626) published *The Proficience and Advancement of Learning* in 1605. From this time onward, many new theories about the exact constituents of nature and their interactions were suggested, overhauled and rejected.

Robert Boyle (1627 – 1691) began research on how gases respond to changes in temperature and volume, which was carried on by others such as Joseph Louis Gay-Lussac, Sadi Carnot or James Watt and ultimately lead to the invention of thermodynamics. As a result the steam engine revolutionized industrial production. In parallel, chemistry as a science in its own right began to take shape as Antoine-Laurent de Lavoisier published what is today considered the first modern textbook on chemistry in 1789 and John Dalton proposed the atomic theory of matter in 1803. During the 19$^{\text{th}}$ century chemistry flourished and many famous scientists contributed, of which some notable examples are the establishment of the periodic system of the elements by Dimitri Mendeleev in 1869, the establishment of organic chemistry and the first synthesis of Urea by Friedrich Wöhler in 1828, the discovery

*During Newtons lifetime, both the Julian (old style) and Gregorian calendars (new style) were in use. This lead to subsequent confusion about his time of death, which is why there exist two dates depending which calendar is referred to.[4]

of radioactivity by Wilhelm Conrad Röntgen (1895) and Henri Becquerel (1896) and the subsequent work by Marie and Pierre Curie, as well as the discovery of the atomic nucleus in scattering experiments by Ernest Rutherford in 1906. Within the physics community, some of the major milestones included the elucidation of the phenomena of electricity and magnetism by eminent names such as Benjamin Franklin, Michael Faraday, Allesandro Volta, Charles-Augustin de Coulomb and many others which ultimately culminated in James Clerk Maxwell's work unifying both concepts into the theory of electro-magnetism, or the generalization of Newton's equations of motion by Joseph-Louis Lagrange and Sir William Rowan Hamilton.

With the turn of the 19^{th} century, new phenomena began to emerge, which stood in stark contrast with the established classical theories of how matter behaves. One of the riddles that had been debated for a long time, was whether light is to be described as a wave or as particles. Both Descartes and Newton argued in their corpuscular theory of light, that it is composed of individual particles, which explains the fact that light beams always seem to travel in straight lines. Christiaan Huygens (1629 – 1695) on the other hand put forward a theory of light based on continuous wave fronts, which was successfully able to explain the refraction of light at boundaries of different transparent materials. Furthermore, measurements showed that the speed of light seemed to be independent of the relative velocities between the light source and the observer. In addition to these apparently incompatible behaviors of light, other problems arose, such as the electro-magnetic spectrum of a black body or the photoelectric effect observed when metals were exposed to electromagnetic radiation.

The consequences that arose in the theories that attempted the explanation of these phenomena were in such opposition to our usual experiences, that many of the scientists that worked on them were themselves not convinced of their integrity. One of the two major milestones is of course Albert Einstein's (1879 – 1955) theory of relativity, which solved the puzzle of constant light speed and lead to famous predictions such as black holes and gravitational waves that distort the four-dimensional space-time, all of which has been supported by experimental observations.[8]

The second theory that shook the scientific community was concerned with the elucidation of the behavior of single molecules, atoms and particles and was termed quantum mechanics. Within the realm of quantum mechanics, the usual rules

how things behave seem to dissipate and our tangible reality gets replaced with concepts such as uncertainty, probability and non-local correlation. The underlying mathematical structure, which was necessary to explain observed reality has been tested to unprecedented accuracy[†] and in conjunction with Einstein's theory of relativity enabled us to completely work out theories of matter encompassing all scales from the Planck length[‡] to the entire visible universe.[8]

Having been equipped with both, the toolbox provided by chemists of the last 300 years, as well as the theory of quantum mechanics, modern chemistry and physics are able to image and manipulate single atoms, predict, characterize, synthesize and manipulate molecules and materials, provide the basis for medicine, catalysis, industrial agriculture and food production, creation of novel materials in all areas of daily life, means to tackle climate change and, for better of for worse, transform our planet.

One of the key areas in modern chemistry and physics is the interaction of gases and liquids with solid materials, as these are present everywhere in our world and often define the interfaces at which chemical and physical reactions take place. Examples for important liquid-solid and gaseous-solid interfaces are countless. For instance, it is hypothesized that the first examples of protocells and RNA where only possible due to the stabilizing interactions of these molecules with mineral surfaces.[11] These interfaces appear in our daily lives in obvious ways everywhere we look, such as the weathering of rocks or shoes engineered to be water-proof and in less obvious ways, such as the fact that the amounts of fertilizer that are required to feed the ever-growing population were not possible without the solid catalysts used in the Haber-Bosch process to convert hydrogen and nitrogen to ammonia.

Surface science is faced with a unique challenge, since the number of atoms or molecules that are typically present on a surface ($\approx 10^{15}\,\mathrm{cm}^{-2}$) is diminishing in comparison with typical number of atoms or molecules in the material that constitutes the surface ($\approx 10^{22}\,\mathrm{cm}^{-3}$, a factor of 10 million). The foundations of surface-science are often credited to Irving Langmuir (1881 – 1957), who conducted

[†]The uncertainty in the value of the so called muon g-factor has been measured in accordance with theory to less than one part in a billion.[9]

[‡]The Planck length defines the smallest measurable length within the theory of quantum mechanics. In order to measure distances shorter than the Planck length, one would need photons of even shorter wavelength, which would inevitably create a black hole.[10] It is equal to $l_p = 1.616 \times 10^{-35}\,\mathrm{m}$

studies on the macroscopic behavior of adsorption and desorption of gasses on metallic surfaces. He was able to show, that diatomic molecules such as hydrogen and oxygen adsorb dissociatively on tungsten and many of his models, even though often simplistic in their assumptions, are still used today to gain qualitative understanding about adsorption processes.[12]

Studies concerning the atomistic and molecular characteristics and behaviors of such interfaces were difficult, since due to the low concentration of adsorbed species as opposed to the bulk material, one not only requires tools that are sensitive to the surface of the material and not the bulk, but also methods that can detect the low concentration of adsorbates reliably. The development of these tools was greatly aided due to historical reasons: Firstly, in the 1950s and 60s, the "space race" for the moon and the large market for vacuum-tubes in electronics greatly increased research activities concerning clean metallic surfaces and ultra-high vacuum (UHV) systems, both fundamental requirements for surface science studies. Secondly, the advent of the semi-conductor in the 50s and the subsequent explosion in computational power not only made theoretical studies feasible, it also further increased the interest in manufacturing highly specific surfaces. A further boost was received in the 1970s, when due to the energy crisis, interest in the development of new solid state catalysts gained huge momentum.[12–14]

Today, surface science is equipped with an arsenal of over 65 different techniques with a sensitivity of $\leq 1\,\%$ of a monolayer to investigate the composition, electronic structure, oxidation states and dynamics of the system.[12] *Some* of the cornerstones of modern spectroscopic methods include low-energy electron diffraction, which is able to deduce the structure of periodic surface arrangements, scanning tunneling and atomic force microscopy, both able to resolve individual atoms on surfaces, X-ray photoelectron and Auger electron spectroscopy reveal information about the electronic and chemical states of the adsorbates, (gracing incidence) infrared spectroscopy gives insight into the vibrational modes and of course quantum mechanical studies are able to investigate models of experimental findings and thus give deep insight into atomistic data, such as the electronic structure, molecular geometries, kinetic and dynamic properties amongst many other.

One of the difficulties arising in the experimental and theoretical description is the complexity of these processes as well as the different timescales at which processes occur. The quantum mechanical apparatus is in principle capable of exactly calculating and predicting (within the framework of the chosen level of

theory) all properties of the system. However, while the microscopic picture at the atomic level describes the fundamental processes that are happening, such as vibrations and bond-formation and breaking, macroscopic effects are usually only observed after longer timescales, involving not only many repetitions of the atomic processes but also the interaction between all the constituents amongst themselves, as well as with the environment, which is often completely neglected in theoretical studies. In order to bridge these gaps, various methods have been suggested. For one, it is possible to treat only the electronic part of the system at the quantum mechanical level, while the macroscopic properties are inferred from statistical thermodynamical arguments. Another approach to explicitly follow the motion of the atoms is to calculate forces acting on particles in a quantum mechanical framework, while the nuclei themselves are propagated using Newton's classical equation of motion. While for heavy atoms this description is adequate, attention has to be given when for example hydrogen is involved, where zero-point energies and quantum-tunneling effects play a considerable role. The involved mathematical description limits the application of these systems and the timescales that can be simulated are in the pico-second range, which is why for highly complex systems or for longer simulation times, one often describes the interactions between individual atoms and molecules by empirically derived force-fields. Of course, various combinations of these approaches also exist. An alternative approach is brought forward by statistically sampling the configuration space of the system, for example by kinetic Monte Carlo methods, which allows for simulation times in the range of seconds or even minuets.[15,16]

In the first part of this thesis we will develop the quantum mechanical apparatus required for the description of our systems and offer context on how to extract thermodynamical information about reactions happening on surfaces. We will then move on to apply this methodology to various systems involving the interaction of hydrogen with solid surfaces and materials.

First, we are concerned with a partially oxidized ruthenium metal surface exposed to hydrogen gas. The potential energy surface for the formation of water is calculated using first-principle quantum mechanical methods and the behavior of the system is compared to a surface that has been covered under a two-atom thick sheet of silica (crystalline SiO_2). The physical constraint that is introduced for surface adsorbates via the silica sheet is a prime example for the field of *confined chemistry*, which has seen a surge in interest over the last decades. We

use our results in conjunction with experiment to set up a micro-kinetic model to fundamentally understand the processes happening on the surface.

In a next step, we investigate the behavior of the silica sheet on ruthenium when exposed to hydrogen plasma and the subsequent chemical alteration of the bilayer sheet. The functionalization of the bilayer is a direct route to modify the chemical and physical properties of the structure and thereby allows for potential design of novel ultra-thin materials.

The last topic will look at the typical trade-offs that are made when modelling a periodic surface with quantum mechanical tools. We will use the diffusion barrier of hydrogen adsorbed on an aluminum-oxide surface as a case study to systematically remove quantum mechanical approximations and increase the accuracy of our model below chemical accuracy in order to supply a benchmark for experiment.

2 Theory

2.1 A Brief Introduction to Quantum Mechanics

The fundamental cornerstone of this thesis is quantum mechanics, which, together with Einstein's theory of relativity, accounts for all physical principles we have found to govern our universe.[8] Both theories, quantum mechanics and relativity, are known for their audacious predictions, none of which could be falsified so far.[17,18] Even though Paul Dirac was able to find a formulation of quantum mechanics which is compatible with Einsteins special theory of relativity,[19] this thesis will focus on the "classical" Schrödinger equation, which is incompatible with the special theory of relativity and hence can only be utilized for the study of *light* atoms (i.e. atoms with a small number of constituting protons in the nucleus), as for those, the kinetic energy contribution to the atom is of low enough magnitude.[20] Nonetheless, Schrödingers original formulation was a tremendous advance in the mathematical description of the laws of quantum mechanics, which were uncovered by famous names such as Niels Bohr, Werner Heisenberg, Wolfgang Pauli and many others.[21]

One of the many striking results of quantum mechanics is that it is impossible to predict how any particle moves from one part in space to another, that is which exact trajectory it will take and even further that it is impossible to predict the position of any particle precisely.[22] This result is of course now known as the famous Heisenberg uncertainty principle, which states that when one restricts the probability of a particle's location (for example by containing it in a potential well), one will lose information about the particle's momentum, i.e. its directional motion. This means, one can only ever calculate a probability of finding a particle within a given volume of space at a certain time.[23] One of the postulates of quantum mechanics is, that this probability density p is given by the square of the absolute

value of a (in general complex valued) function Ψ

$$p = |\Psi|^2 = \Psi^* \Psi \qquad , \tag{2.1}$$

termed the wavefunction, which depends on all degrees of freedom of the system under consideration, for example the spatial and spin coordinates of electrons in an atom, as well as time. Of course, the total probability of finding a particle anywhere in space must be equal to unity, which requires the wavefunction to be normalized:[24]

$$\int_{\mathbb{R}^3} |\Psi|^2 \, \mathrm{d}V \stackrel{!}{=} 1 \qquad . \tag{2.2}$$

It is the Schrödinger equation that uniquely determines the spatiotemporal evolution of such a wavefunction:[20]

$$\mathrm{i}\hbar \frac{\mathrm{d}}{\mathrm{d}t} |\Psi(x,t)\rangle = \hat{H} |\Psi(x,t)\rangle = \left(\hat{T} + \hat{V}\right) |\Psi(x,t)\rangle \qquad , \tag{2.3}$$

where x depends on all degrees of freedom of the system, t denotes time and $\hat{H}$ is the so called *Hamiltonian operator* of the system, which in turn is comprised of the kinetic ($\hat{T}$) and potential energy ($\hat{V}$) operator, i.e. the total energy of the system.

For atoms and molecules, we are in general interested in stationary states, i.e. states whose total energy is constant in time. Consequently, the Hamiltonian operator $\hat{H}$ does not explicitly depend on time and thus any solution to the Schrödinger equation 2.3 can be written as the initial wavefunction $|\Psi_n(x,0)\rangle$ and a phase factor, which only depends on the total energy E of the system:

$$|\Psi_n(x,t)\rangle = \mathrm{e}^{-\mathrm{i}\frac{E_n}{\hbar}t} |\Psi_n(x,0)\rangle \tag{2.4}$$

Since there are multiple states of different Energy for a given system, the wavefunction describing the system and its corresponding eigenvalue E_n have been indexed with the number n.

As a result, for stationary systems it is sufficient to determine the time-independent part of the wavefunction, which is subsequently determined by the time-independent Schrödinger equation

$$\hat{H} |\Psi_n(x)\rangle = E_n |\Psi_n(x)\rangle \qquad , \tag{2.5}$$

with the time independent Hamilton operator, which for a system of N electrons

interacting in the Coulomb field of M atomic nuclei, is given by

$$\hat{H} = \hat{T} + \hat{V} = \left(\hat{T}_e + \hat{T}_n\right) + \left(\hat{V}_{en} + \hat{V}_{ee} + \hat{V}_{nn}\right) \quad , \tag{2.6}$$

with the kinetic energy of the electrons and nuclei

$$\hat{T}_e = -\sum_i^N \frac{\hbar^2}{2m_e} \vec{\nabla}^2_{\vec{r}_i} \tag{2.7}$$

$$\hat{T}_n = -\sum_i^M \frac{\hbar^2}{2M_i} \vec{\nabla}^2_{\vec{R}_i} \quad , \tag{2.8}$$

the attractive potential between nuclei and electrons

$$\hat{V}_{en} = -\sum_i^N \sum_j^M \frac{Z_i e^2}{4\pi\epsilon_0} \frac{1}{|\vec{r}_i - \vec{R}_j|} \quad , \tag{2.9}$$

and the repuslive potentials between electrons and nuclei, respectively:

$$\hat{V}_{ee} = \sum_i^N \sum_{j>i}^N \frac{e^2}{4\pi\epsilon_0} \frac{1}{|\vec{r}_i - \vec{r}_j|} \tag{2.10}$$

$$\hat{V}_{nn} = \sum_i^M \sum_{j>i}^M \frac{Z_i Z_j e^2}{4\pi\epsilon_0} \frac{1}{|\vec{R}_i - \vec{R}_j|} \quad . \tag{2.11}$$

Here, $\vec{\nabla}$ denotes the Nabla operator, ϵ_0 is the absolute dielectric permittivity in vacuum, e is the elementary charge, m_e is the rest mass of the electron, M_i is the rest mass of the i-th nucleus, Z_i is the nuclear charge of the i-th nucleus and $\vec{r}_i$ and $\vec{R}_i$ are the coordinate-vectors of the i-th electron or nucleus, respectively.

Since the constants that appear in eqs. (2.7) to (2.11) are somewhat cumbersome, it is customary to re-scale the unit system from SI units to so called atomic units (a.u.),[25] scaled such that

$$e = m_e = \hbar = \frac{1}{4\pi\epsilon_0} = 1 \text{ a.u.} \quad . \tag{2.12}$$

This simplifies the algebra and consequently, we will use atomic units throughout.

Once the (time independent) wavefunction Ψ has been found, a further postulate of quantum mechanics states that any physical observable property o of the system,

for example the total energy, is given by the so called expectation value

$$\langle o \rangle = \left\langle \Psi \middle| \hat{\mathrm{O}} \middle| \Psi \right\rangle = \int_{\mathbb{R}^3} \Psi^* \, \hat{\mathrm{O}} \, \Psi \, \mathrm{d}V \qquad , \tag{2.13}$$

where $\hat{\mathrm{O}}$ is the quantum mechanical operator representing the observable and * represents complex conjugation. If an observable of a quantum mechanical system can be predicted without uncertainty, the system is said to be in an eigenstate $\left|\Psi^{\hat{\mathrm{O}}}\right\rangle$ of the operator associated with this observable. Mathematically this means, that when the operator acts upon the wavefunction describing this eigenstate, it returns the same eigenstate multiplied with the value of the observable

$$\hat{\mathrm{O}} \left|\Psi_n^{\hat{\mathrm{O}}}\right\rangle = o_n \left|\Psi_n^{\hat{\mathrm{O}}}\right\rangle \qquad , \tag{2.14}$$

where any operator usually has an infinite spectrum of eigenstates and eigenvalues o_n, which are thus numbered by the index n. For any hermitian operator, in particular the Hamiltonian, these eigenvalues are always guaranteed to be real.

By solving the differential equation 2.3, one obtains the true wavefunction Ψ of the system, which in turn then encodes all possible observables of the system. The ansatz for the solution is usually chosen by expanding the true wavefunction in a (finite) set of basis functions, termed ab-initio *wavefunction-based* methods. A different approach is termed *density functional theory* and is based on the two Hohenberg-Kohn theorems (vide infra), which show that in principle it is unnecessary to know the explicit wavefunction Ψ, as all properties of the system are also determined by the one-electron density function of the system, which only implicitly depends on the coordinates of the constituting particles.

2.2 Properties of Wavefunctions and Required Fundamental Approximations

As explained in the previous section, all properties of a system are determined by its wavefunction, where the square of the absolute value of the wavefunction is equal to the probability density of finding a particle within a given differential volume. However, it was demonstrated in 1922 by Otto Stern and Walther Gerlach that when one sends a beam of positively charged silver atoms trough an inhomogeneous magnetic field aligned along an axis, the beam will exhibit a well defined separation into two parts, parallel to the field direction.[26]

It was deduced that the electron has an additional, quantized degree of freedom, coined the spin, which can only obtain one of two possible values, named α and β (or up and down). This degree of freedom has all properties of angular momentum, however it has no classical counterpart, since it is an intrinsic property of electrons that does not depend on any "rotation" in real space. Only Dirac was able to deduce it from fundamental principles using his relativistic counterpart of the Schrödinger equation.[19] Before this theory was put on a sound theoretical basis however, in his work on atomic spectra, Wolfgang Pauli found that this fourth quantum number describing the spin of the electron, would allow for the explanation of the fine structure observed for the hydrogen adsorption spectrum. This lead to his famous rule, later termed Pauli exclusion principle, which states that no two electrons in an atom can occupy the same orbital, where the orbital is described by four quantum numbers.[27] This formulation is somewhat inexact, since a fundamental requirement of quantum mechanics is the indistinguishability of quantum particles, that is to say it is impossible to assign two different probability densities to two different particles of the same type in the same system. A mathematical formulation of the Pauli principle is that whenever two indistinguishable particles in a quantum mechanical system interchange their coordinates, the wavefunction has to change sign[28]

$$\Psi(\vec{r}_1, \vec{r}_2) = -\Psi(\vec{r}_2, \vec{r}_1) \qquad . \tag{2.15}$$

This condition prevents a wavefunction comprised of a system of N particles to be simply written as products of N individual one-particle wavefunctions $\psi(\vec{r}_i)$:

$$\Psi^{\mathrm{HP}}(\vec{r}_1, \vec{r}_2, \ldots) = \psi_1(\vec{r}_1)\psi_2(\vec{r}_2)\ldots \qquad , \tag{2.16}$$

which is called a Hartree product. In order to fulfill this requirement, the wavefunction is usually written as a so called Slater determinant

$$\left|\Psi^{\mathrm{SD}}(\vec{r}_1,\vec{r}_2,\ldots,\vec{r}_N)\right\rangle = \frac{1}{\sqrt{N!}}\det\begin{vmatrix}\psi_1(\vec{r}_1) & \psi_1(\vec{r}_2) & \cdots & \psi_1(\vec{r}_N)\\ \psi_2(\vec{r}_1) & \psi_2(\vec{r}_2) & \cdots & \psi_2(\vec{r}_N)\\ \vdots & \vdots & \ddots & \vdots\\ \psi_N(\vec{r}_1) & \psi_N(\vec{r}_2) & \cdots & \psi_N(\vec{r}_N)\end{vmatrix} \quad , \tag{2.17}$$

which is an antisymmetrized linear combination of all possible permutations of Hartree products and automatically fulfills the Pauli principle. However, in general, the true wavefunction Ψ is a linear combination of an infinite number of such Slater determinants. Thus, when approximating the wavefunction with a finite number of Slater determinants, it is in general no longer an eigenfunction of the Hamiltonian operator.

As elaborated on above, for stationary systems, the wavefunction is completely determined by the time-independent Schrödinger equation (2.5), which constitutes a many-body-problem of interacting particles, for which even in the classical Newtonian case, there exist no analytical solutions in the general case. For that reason, it is required to introduce further approximations to the system, of which the most fundamental is the so called Born-Oppenheimer approximation.[29] It allows for a separation of the total wavefunction Ψ into a nuclear and an electronic wavefunction

$$|\Psi\rangle = \phi_{\mathrm{nuc}}\left(\{\vec{R}\}\right)\Phi_{\mathrm{elec}}\left(\{\vec{r}\},\{\vec{R}\}\right) \quad , \tag{2.18}$$

owing to the fact that nuclei and electrons are of different magnitude in their mass and motion of the electrons around the heavy nuclei can be interpreted as moving in a very slowly varying electrostatic potential that is constant in first order. In other words, electrons are allowed to adapt instantaneously to the configuration of the nuclei. As a result of this approximation, one introduces the so called potential energy (hyper)surface $E(\{\vec{R}_i\})$, which is the potential energy surface in the space of the nuclear coordinates of the molecule. The electronic wavefunction is then determined by the so called "clamped-nuclei" Schrödinger equation

$$\hat{H}_{\mathrm{elec}}\left|\Phi_{\mathrm{elec}}\right\rangle = E_{\mathrm{elec}}\left|\Phi_{\mathrm{elec}}\right\rangle \quad , \tag{2.19}$$

where the electronic Hamiltonian is given by

$$\hat{H}_{\text{elec}} = \hat{T}_e + \hat{V}_{en} + \hat{V}_{ee} + \hat{V}_{nn} \qquad , \tag{2.20}$$

where V_{nn} and V_{en} now only parametrically depend on the set of nuclear coordinates. The nuclear wavefunction and the total energy of the clamped system in turn is then determined by the nuclear Schrödinger equation

$$\hat{H}_{\text{nuc}} \left|\phi_{\text{nuc}}\right\rangle = \left(\hat{T}_n + E_{\text{elec}}\right) \left|\phi_{\text{nuc}}\right\rangle = E_{\text{tot}} \left|\phi_{\text{nuc}}\right\rangle \qquad , \tag{2.21}$$

where the electronic energy of the system acts as a potential energy that is added to the kinetic energy of the nuclei.

2.3 Hartree-Fock Theory

2.3.1 Formalism

The Hartree-Fock algorithm, as pioneered by Douglas R. Hartree[30] and amended by Vladimir A. Fock,[31] is probably the best known example for determining approximate wavefunctions for atoms and molecules and serves as a starting point for many other, more sophisticated algorithms that try to improve on the inherent approximations made. As introduced before, the Born-Oppenheimer approximation allows for the decoupling of the nuclear from the electronic degrees of freedom. This transforms the full problem of all interacting particles into a problem of moving electrons in a fixed electrostatic potential created by the frozen nuclei. Albeit reduced in complexity, the coupling of the electronic motion via the electron-electron repulsion potential $\hat{V}_{ee}$, still precludes an analytical solution of the partial differential equation posed by the electronic Schrödinger equation (2.19).

However, we may utilize the variational principle,[32] which states that any wavefunction Ψ^{test}, which is not the true ground state Ψ_0 of the system under study, will yield a larger Rayleigh quotient

$$E[\Psi^{\text{test}}] = \frac{\left\langle \Psi^{\text{test}} \middle| \hat{H} \middle| \Psi^{\text{test}} \right\rangle}{\left\langle \Psi^{\text{test}} \middle| \Psi^{\text{test}} \right\rangle} \geq E[\Psi_0] \tag{2.22}$$

than the ground state. Consequently, the Slater determinant with the lowest possible energy expectation value will be the best possible approximation to the true ground state wavefunction.

The Hartree-Fock algorithm now leverages this principle by writing the energy expectation value of a trial wavefunction as a functional of the orbitals that form the Slater determinant[24]

$$E_{\text{elec}}\left[\{\psi_i\}\right] = \langle \hat{H}_{\text{elec}} \rangle = \left\langle \Psi^{\text{SD}} \middle| \hat{T}_e + \hat{V}_{en} + \hat{V}_{ee} + \hat{V}_{nn} \middle| \Psi^{\text{SD}} \right\rangle \tag{2.23}$$

$$= \sum_i \left\langle \psi_i \middle| \hat{h} \middle| \psi_i \right\rangle + \frac{1}{2} \sum_{i,j} \langle \psi_i \psi_j \,|\, \psi_i \psi_j \rangle - \langle \psi_i \psi_j | \psi_j \psi_i \rangle \tag{2.24}$$

$$= \sum_i \left\langle \psi_i \middle| \hat{h} \middle| \psi_i \right\rangle + \frac{1}{2} \sum_{i,j} \langle \psi_i \psi_j \,\|\, \psi_i \psi_j \rangle \qquad , \tag{2.25}$$

where we have used the so called Slater-Condon rules[33,34] for the evaluation of one- and two-electron operator expectation values with Slater determinants and the

shorthand notation

$$\hat{h} = -\frac{1}{2}\vec{\nabla}^2_{\vec{r}_i} - \sum_M \frac{Z_M}{|\vec{r}_i - \vec{R}_M|} \tag{2.26}$$

$$\langle \psi_i \psi_j \parallel \psi_k \psi_l \rangle = \langle \psi_i \psi_j \,|\, \psi_k \psi_l \rangle - \langle \psi_i \psi_j \,|\, \psi_l \psi_k \rangle \tag{2.27}$$

$$\langle \psi_i \psi_j | \psi_k \psi_l \rangle = \iint \psi_i^\dagger(\vec{r}) \psi_j^\dagger(\vec{r}') \frac{1}{|\vec{r} - \vec{r}'|} \psi_k(\vec{r}) \psi_l(\vec{r}') \, \mathrm{d}\vec{r} \, \mathrm{d}\vec{r}' \quad . \tag{2.28}$$

The orbitals ψ_i depend on all electronic degrees of freedom, that is both the spatial $\vec{r}_i$ and spin coordinates σ_i.

It then finds the minimum of this functional by linearly varying the orbitals under the condition, that the resulting orbitals remain orthonormal to each other, i.e. that $\langle \psi_i | \psi_j \rangle = \delta_{ij}$ with the Kronecker delta δ_{ij}. This is achieved by using the method of Lagrange multipliers and the Lagrangian reads

$$\mathcal{L} = E_{\text{elec}}\left[\{\psi_i\}\right] - \sum_{i,j} \epsilon_{ji} \Big(\langle \psi_i \,|\, \psi_j \rangle - \delta_{ij} \Big) \quad , \tag{2.29}$$

where the ϵ_{ji} are the Lagrange multipliers. The stationary condition now requires that for any arbitrarily small variation of the orbitals, the variation in the Lagrangian must vanish. Applying this for the k-th orbital, we obtain

$$0 \stackrel{!}{=} \delta\mathcal{L}^{(k)} = \delta E^{(k)}_{\text{elec}}\left[\{\psi_i\}\right] - \sum_i \epsilon_{ik} \langle \delta\psi_k \,|\, \psi_i \rangle + \text{c.c.} \tag{2.30}$$

$$= \Big\langle \delta\psi_k \Big| \hat{h} \Big| \psi_k \Big\rangle + \sum_i \langle \delta\psi_k \psi_i \parallel \psi_k \psi_i \rangle - \sum_i \epsilon_{ik} \langle \delta\psi_k \,|\, \psi_i \rangle + \text{c.c.} \tag{2.31}$$

$$= \Big\langle \delta\psi_k \Big| \hat{F} \Big| \psi_k \Big\rangle - \sum_i \epsilon_{ik} \langle \delta\psi_k | \psi_i \rangle + \text{c.c.} \quad , \tag{2.32}$$

where we have introduced the so called Fock operator

$$\hat{F} = \hat{h} + \sum_i \hat{J}_i - \hat{K}_i \quad , \tag{2.33}$$

with the Coulomb operator $\hat{J}$ and exchange operator $\hat{K}$, which are defined in their action on an arbitrary orbital ψ as

$$\hat{J}_i \, \psi(\vec{r}) = \int \psi_i^\dagger(\vec{r}') \psi_i(\vec{r}') \frac{1}{|\vec{r} - \vec{r}'|} \, \mathrm{d}\vec{r}' \; \psi(\vec{r}) \tag{2.34}$$

$$\hat{K}_i \, \psi(\vec{r}) = \int \psi_i^\dagger(\vec{r}') \psi(\vec{r}') \frac{1}{|\vec{r} - \vec{r}'|} \, \mathrm{d}\vec{r}' \; \psi_i(\vec{r}) \quad . \tag{2.35}$$

Applying these variations yields, after some manipulations, a set of $k = 1, \ldots, N$ equations

$$\hat{F} \left|\psi_k\right\rangle = \sum_i \epsilon_{ki} \left|\psi_i\right\rangle \qquad , \tag{2.36}$$

which can be compactly written as

$$\mathbf{F}\underline{\psi} = \mathcal{E}\underline{\psi} \qquad . \tag{2.37}$$

Since $\mathcal{E}$ is hermitian, we can utilize the unitary matrix $\mathbf{U} = (\underline{q}_1, \ldots, \underline{q}_N)$, with the eigenvectors $\underline{q}_i$ of $\mathcal{E}$, to rewrite eq. (2.37) as

$$\mathbf{F}\underline{\widetilde{\psi}} = \widetilde{\epsilon}\underline{\widetilde{\psi}} \tag{2.38}$$

with

$$\mathcal{E} = \mathbf{U}\widetilde{\epsilon}\mathbf{U}^\dagger \tag{2.39}$$

and

$$\underline{\widetilde{\psi}} = \mathbf{U}^\dagger\underline{\psi} \qquad , \tag{2.40}$$

which diagonalizes $\mathcal{E}$ and eq. (2.38) becomes a set of N non-linear equations

$$\hat{F} \left|\widetilde{\psi}_i\right\rangle = \widetilde{\epsilon}_i \left|\widetilde{\psi}_i\right\rangle \qquad . \tag{2.41}$$

In principle, this poses an ordinary eigenvalue problem, which can be solved with standard tools of linear algebra. However, the fact that the Fock operator $\hat{F}$ itself explicitly depends on the solution of these equations, means they have to be solved iteratively: A Fock operator is constructed from a set of guessed one-electron orbitals, the resulting eigenvalue problem is then solved and the solutions are used to construct a new Fock operator. This procedure is repeated until a convergence threshold (for example the change in energy or density) has been reached and the resulting new orbitals only marginally differ from the previous iteration, i.e. until self-convergence is achieved.

Since the Fock operator is a sum of effective one-electron operators, where the true electron-electron interaction potential $\hat{V}_{ee}$ has been replaced with the average electrostatic potential generated by all electrons in the system except for the one the potential is acting on, this can be interpreted as iteratively letting a test charge relax in the field of all electrons until it is self-consistent. Hence, this type of optimization is often called the “self-consistent field method”.

The fact, that in general, the true wavefunction Ψ cannot be represented as a single Slater determinant and that the Hartree-Fock algorithm provides the Slater determinant with the lowest possible energy expectation value, results in the definition of the so called correlation energy according to Löwdin[35]

$$E_{\text{corr}} = E_0 - E_0^{\text{HF}} \quad , \tag{2.42}$$

with the Hartree-Fock Energy E_0^{HF} and the true ground state energy E_0. However, this definition is somewhat unfortunate, since strictly speaking, the Hartree-Fock method already includes Fermi correlation, which arises from the anti-symmetry of the wavefunction. Nonetheless, the Hartree-Fock algorithm does not account for the so called Coulomb correlation, which is an effect of the instantaneous interactions of electrons, that cannot be described in the mean field approach of the Hartree-Fock method.[36] As a result, one of the flaws of this algorithm is that it cannot describe dispersive long-range interactions.[37]

This type of correlation energy is often referred to as so called dynamic correlation, arising from the instantaneous interaction of the particles and the anti-symmetry of the wavefunction. In addition to these, there is also static correlation, which cannot be described by any method using a single Slater determinant, as it originates in the fact that there exist multiple determinants with comparable weight in the configuration interaction expansion (vide infra). In general, these types of systems can be treated by so called multi-reference methods, which will not be discussed in this thesis.

2.3.2 The LCAO Ansatz and the Roothaan-Hall Equations

In order to solve the Hartree-Fock equations 2.38, we require a starting guess for the one-electron orbitals in order to form the Fock operator and solve for the new orbitals. To this end, the one-electron orbitals ψ_i are expressed as a linear combination of basis functions:

$$\psi_i(\vec{r}) = \sum_n c_{n,i}\chi_n(\vec{r}) \quad . \tag{2.43}$$

In principle, the choice of Basis set $\{\chi_n\}$ is arbitrary and different types of basis functions are able to describe different types of physics. For example, a common choice are hydrogen-like, atom-centered basis functions, which lend

themselves naturally to the description of molecules in a vacuum, applying the linear combination of atomic orbitals (LCAO) theory. One of the advantages of this type of basis set is, that tightly bound core states are rarely strongly influenced and thus they largely retain their atom-like structure, even for strongly interacting atoms in molecules. An example of such a basis set is the so called (spherical) Slater type orbital (STO) basis set

$$\chi_{\zeta,l,m,A}(\vec{r}) = N_{\zeta,l}\, \mathrm{e}^{-\zeta|\vec{r}-\vec{R}_A|} \left|\vec{r}-\vec{R}_A\right|^l \bar{Y}_{l,m}(\vec{r}-\vec{R}_A) \qquad , \tag{2.44}$$

where ζ is a parametric exponent that may be chosen freely, $\vec{R}_A$ is the position of the A-th Atom, $N_{\zeta,l}$ is a normalizing factor and $\bar{Y}_{l,m}$ is a real combination of spherical harmonics. One immediate draw-back of STO basis sets are their mathematical structure, since the integrals that result in the solution of the Hartree-Fock equations require combinations of two or more basis functions on different atoms, which cannot be easily solved analytically for this type of functions.

Another basis set, which tries to sidestep the problems of integration encountered in the STO basis set is the Gaussian basis set, where the (physically correct) exponential decay in eq. (2.44) is replaced with Gaussian type functions

$$\chi_{\alpha,l,m,A}(\vec{r}) = N_{\alpha,l}\, \mathrm{e}^{-\alpha\left|\vec{r}-\vec{R}_A\right|^2} \left|\vec{r}-\vec{R}_A\right|^l \bar{Y}_{l,m}(\vec{r}-\vec{R}_A) \qquad , \tag{2.45}$$

which inherently possess the attribute, that products of two spatially separated Gaussian functions yield another (displaced) Gaussian. The computationally strongest advantage is however, that integrals of functions with higher angular momenta components can be expressed in terms of integrals of lower angular momenta.[38] However, this basis set inevitably introduces an error, since physically exact wavefunctions have a cusp at the position of the nucleus, resulting from the unbounded electron-nucleus Coulomb potential, centered at the nucleus. To mitigate this error, usually each basis function in a Gaussian type orbital (GTO) basis set, is fitted to a Slater type orbital by expanding it in a small set of Gaussian functions until a satisfactory overlap between the true Slater orbital and the GTO is achieved. This method is often referred to as the STO-nG basis set, where n is an integer indicating how many primitive Gaussians have been used to approximate a single Slater type orbital. A comparison between a Slater type function and various approximated STO-nG functions is shown in fig. 2.1.

If one includes more than one function per electron for the description of valence

states, the basis is termed a "split-valence" basis and is often referred to as double- (triple-, etc.) zeta quality, referring to the ζ-Exponent of eq. (2.44). Another common way of modifying the basis as described above is the addition of so called polarization functions, that is functions of higher angular momenta than required in the minimal description of the atom, for example p-like terms on hydrogen or d-like terms on first-row elements. In addition to that, in order to allow for even more flexibility in the spanned Hilbert space, one often includes so called diffuse orbitals, which have a very low Gaussian exponent and therefore a large spatial extent.

A type of basis set, which is especially useful for high-accuracy computations is the so called correlation-consistent (cc) basis set. These have been developed in order to obtain a smooth convergence of the correlation energy when increasing the basis set size and therefore allow for extrapolation to the basis set limit.

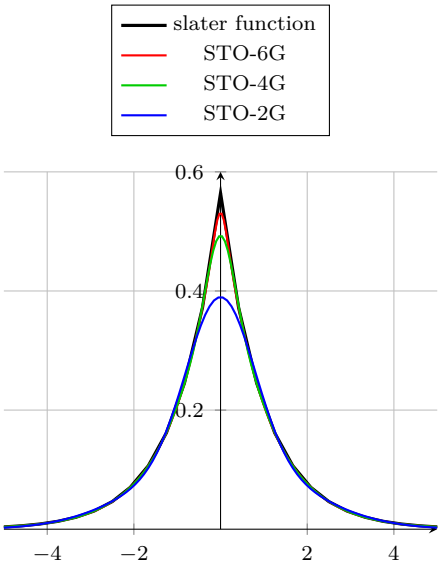

Figure 2.1: Comparison between a Slater type function and various approximations using Gaussian type orbitals. The Slater function has a cusp at the position of the nucleus, which cannot be reproduced exactly by the Gaussian functions, except in an infinite primitive function limit.

A multitude of other basis sets have been developed over the years, some highly adapted to special kinds of physics, while others try to be as generally applicable as possible. However, an increase in basis functions will not only have a negative impact on the computational cost of the algorithm, it may also introduce (near) linear-dependencies in the basis set, resulting in numerical instabilities. The choice of a particular basis is therefore often crucial and a trade-off between accuracy and numerical tractability has to be made.

A further choice of basis, which will be of importance for description of periodic systems, are so called (complex) plane waves, defined as

$$\chi_{\vec{k}}(\vec{r}) = \mathrm{e}^{\mathrm{i}\vec{k}\cdot\vec{r}} \quad , \tag{2.46}$$

where $\vec{k}$ is the so called Bloch vector. This set forms a complete basis for any function that is periodic and thus forms a natural basis for crystalline systems. The huge advantage of this type of basis is the fact, that the quality of the basis can be improved simply by increasing the range of allowed values for $\vec{k}$. Furthermore, plane waves always possess the attribute of orthogonality, that is, they do not suffer from possible (near) linear dependencies or over-completeness. On the other hand, plane waves are, by their very nature, fully delocalized in space. Thus, in order to describe localized parts of the wavefunction, such as core-orbitals, plane waves with very high oscillatory components have to be included in the expansion, or pseudo-potentials such as the augmented plane wave method have to be used.

Once a basis has been chosen, plugging eq. (2.43) into eq. (2.41)

$$\hat{F} \sum_{\nu} c_{\nu,i} \chi_{\nu}(\vec{r}) = \epsilon_i \sum_{\nu} c_{\nu,i} \chi_{\nu}(\vec{r}) \tag{2.47}$$

and projection of $\chi_{\mu}(\vec{r})$ onto the resulting expression:

$$\int \chi_{\mu}(\vec{r})^* \, \hat{F} \sum_{\nu} c_{\nu,i} \, \chi_{\nu}(\vec{r}) \, \mathrm{d}\vec{r} = \int \chi_{\mu}(\vec{r})^* \, \epsilon_i \sum_{\nu} c_{\nu,i} \, \chi_{\nu}(\vec{r}) \, \mathrm{d}\vec{r} \tag{2.48}$$

$$\sum_{\nu} \left\langle \chi_{\mu} \middle| \hat{F} \middle| \chi_{\nu} \right\rangle c_{\nu,i} = \epsilon_i \sum_{\nu} \langle \chi_{\mu} \,|\, \chi_{\nu} \rangle \, c_{\nu,i} \tag{2.49}$$

$$\sum_{\nu} F_{\mu\nu} c_{\nu,i} = \epsilon_i \sum_{\nu} S_{\mu\nu} c_{\nu,i} \qquad , \tag{2.50}$$

yields a system of linear equations, which can be compactly written in Matrix form as:

$$\mathbf{F}\mathbf{c}_i = \mathbf{S}\mathbf{c}_i \epsilon_i \qquad . \tag{2.51}$$

This set of equations is often referred to as Rothaan-Hall equations after Clemens Rothaan and George Hall, who derived them for the first time in 1951.[39,40]

This is again a generalized eigenvalue problem, which may be solved by standard tools of linear algebra. After orthogonalization (for example using symmetric or unitary orthogonalization) and subsequent diagonalization of the Fock matrix $\mathbf{F}$, a vector of new orbital coefficients is obtained and the procedure is repeated until self-consistency is achieved.

2.4 Post Hatree-Fock Methods

2.4.1 The Product State Expansion of the Wavefunction

In the previous sections we introduced the Hartree-Fock algorithm for determining an approximate solution for an arbitrary system of interacting electrons in a static external field. It leveraged the fact that an approximation for the wavefunction may be written as an anti-symmetrized linear combination of one-electron-function products. These are sometimes called product states, owing to the fact that all possible permutations of products appear in them. However, as was touched upon before, the true wavefunction of an arbitrary system can, in general, not be expressed as a single Slater determinant, which is why the Hartree-Fock algorithm is, by definition, incapable of capturing correlation effects.

However, the set of *all* possible Slater determinants, which may be constructed from a complete set of one-electron orbitals $\{\varphi_n\}$, for example approximately determined via the Hartree-Fock algorithm, forms a complete basis in which the true wavefunction may be expanded.

To see this, one considers an arbitrary function $f(x_1, x_2, \ldots, x_N)$, where in a first step all but the first variable is held constant. It is thus possible to expand this function in a complete basis of one-electron functions in the first coordinate:

$$f(x_1, \{x_2, \ldots, x_N\}) = \sum_{n_1} a_{n_1}(x_2, \ldots, x_N)\varphi_{n_1}(x_1) \tag{2.52}$$

with expansion coefficients $a_{n_1}(x_2, \ldots, x_N)$ given by

$$a_{n_1}(x_2, \ldots, x_N) = \langle \varphi_{n_1} \,|\, f \rangle \qquad . \tag{2.53}$$

These coefficients in turn, can be expressed in terms of a function in x_2

$$a_{n_1}(x_2, \{x_3, \ldots, x_N\}) = \sum_{n_2} a_{n_1,n_2}(x_3, \ldots, x_N)\varphi_{n_2}(x_2) \qquad . \tag{2.54}$$

Repeating this for all subsequently appearing coefficients, we obtain the true function as a linear combination of product states

$$f(x_1, x_2, \ldots, x_N) = \sum_{n_1,n_2,\ldots,n_N} a_{n_1,n_2,\ldots,n_N}\varphi_{n_1}(x_1)\varphi_{n_2}(x_2)\cdots\varphi_{n_N}(x_N) \qquad . \tag{2.55}$$

Since for a system of fermions, the wavefunction has to be anti-symmetric with respect to the permutation of any two coordinates, also the expansion coefficients will be anti-symmetric under these permutations $a_{n_{p(1),\ldots,p(N)}} = (-1)^P a_{n_1,\ldots,n_N}$. Fixing the order of the indices, e.g. $n_1 < n_2 < \ldots < n_N$, results in an expansion of the function in the basis of Slater determinants:

$$f(x_1, x_2, \ldots, x_N) = \sum_{n_1<\ldots<n_N} \sqrt{N!} a_{n_1,\ldots,n_1} \Psi^{\mathrm{SD}}_{a_1,\ldots,a_N}(x_1, x_2, \ldots, x_N) \quad . \tag{2.56}$$

2.4.2 Configuration Interaction

The Hartree-Fock algorithm finds the Slater determinant with the lowest possible energy expectation value. While it is already capable of retrieving over 98% of the total energy in comparison to the most accurate descriptions we have,[24] unfortunately it is exactly these last 2% of accuracy that are crucial for studying chemical reactions and the behavior of molecules and solids.

Since, in general, a chosen basis set for a Hartree-Fock calculation will include more basis functions than are required to build the N-electron Slater determinant, the Hartree-Fock algorithm will provide so called virtual orbitals, i.e. orbitals which are not explicitly used in the creation of the N-electron Slater-determinant because their orbital-eigenvalue is too large. Consequently we may expand the full wavefunction according to eq. (2.56) in the space of all possible N-electron determinants that may be constructed from all (occupied and virtual) orbitals of the preceding Hartree-Fock run

$$\Psi_0 = c_0\Phi_0 + \sum_{i,a} c_i^a \Phi_i^a + \sum_{\substack{i<j \\ a<b}} c_{ij}^{ab} \Phi_{ij}^{ab} + \sum_{\substack{i<j<k \\ a<b<c}} c_{ijk}^{abc} \Phi_{ijk}^{abk} + \ldots \quad , \tag{2.57}$$

where Φ_0 is the ground-state Hartree-Fock determinant, Φ_i^a is a determinant with the i-th occupied orbital replaced by the a-th unoccupied orbital and so forth. The indices on the sums have been restricted such that each configuration only appears once in the summation. This expansion is called the Configuration Interaction (CI) method. Subsequently, we will be using the indices $i, j, k, \ldots$ for occupied orbitals, the indices $a, b, c, \ldots$ for virtual orbitals and the indices $p, q, r, \ldots$ for arbitrary orbitals.

While, for a complete one electron basis, this delivers the true wavefunction of the fully correlated system, the number of determinants that have to be considered

in the expansion quickly grows to an insurmountable extent. Consequently, it is customary to restrict the number of determinants that are actually used. This leads to the so called truncated CI methods, for example CIS, CISD..., where S stands for singles, D four doubles and so forth. Here, only determinants with up to a single (double, triple) occupied → virtual substitution are included.

A result which is useful in the CI formalism is Brillouin's theorem, which states that singly excited determinants do not directly mix with the Hartree-Fock ground-state:

$$\left\langle \Phi_0 \middle| \hat{H} \middle| \Phi_i^a \right\rangle = 0 \qquad , \tag{2.58}$$

which results from the fact, that this expectation value is simply the off-diagonal element of the Fock Matrix, which is zero by construction, since the orbitals $\{\psi_i\}$ diagonalize the Fock matrix. Similarly, matrix elements that differ in more than two orbitals do also not mix, which is a result of the Slater-Condon rules, since matrix elements for two electron operators with determinants that differ in more than two orbitals are always zero.[33,34]

In order to determine the correlation energy $E_0 - E_0^{\mathrm{HF}}$ using the CI expansion eq. (2.57), it is convenient to rewrite the wavefunction in an intermediately normalized way, i.e. requiring $c_0 \coloneqq 1$, since then

$$\langle \Phi_0 \,|\, \Psi_0 \rangle = 1 \qquad . \tag{2.59}$$

The correlation energy can be obtained from the eigenvalue equation

$$\hat{H} \,|\Psi_0\rangle = E_0 \,|\Psi_0\rangle \qquad , \tag{2.60}$$

by subtracting $E_0^{\mathrm{HF}} \,|\Psi_0\rangle$ from both sides and projecting with $\langle\Phi_0|$ from the left:

$$\left\langle \Phi_0 \middle| \hat{H} - E_0^{\mathrm{HF}} \middle| \Psi_0 \right\rangle = E_{\mathrm{corr}} \,\langle \Phi_0 \,|\, \Psi_0 \rangle = E_{\mathrm{corr}} \qquad . \tag{2.61}$$

If we plug the expansion eq. (2.57) into eq. (2.61) and exploit Brillouin's theorem, as well as the fact that determinants that differ in more than two orbitals do not mix, we obtain the correlation energy purely in terms of doubly excited determinants:

$$E_{\mathrm{corr}} = \sum_{\substack{i<j \\ a<b}} c_{ij}^{ab} \left\langle \Phi_0 \middle| \hat{H} \middle| \Phi_{ij}^{ab} \right\rangle \qquad . \tag{2.62}$$

In cases where the Hartree-Fock wavefunction is a reasonable approximation to the true ground-state wavefunction, the doubly excited coefficients c_{ij}^{ab} will indeed be the contribution with the largest weight (aside from the reference determinant). However, this does not mean that singly or more than doubly excited determinants do not contribute to the expansion, since the coefficients c_{ij}^{ab} are coupled to all orders. This becomes evident when, if instead of projecting with the Hartree-Fock ground-state from the left, we project with a singly excited determinant

$$\left\langle \Phi_i^a \,\middle|\, \hat{H} - E_0 \,\middle|\, \Psi_0 \right\rangle = E_{\text{corr}} \left\langle \Phi_i^a \,|\, \Psi_0 \right\rangle \tag{2.63}$$

and plugging the CI expansion eq. (2.57) for $|\Psi_0\rangle$ to find

$$\sum_{jb} c_j^b \left\langle \Phi_i^a \,\middle|\, \hat{H} - E_0 \,\middle|\, \Phi_j^b \right\rangle + \sum_{\substack{j<k \\ b<c}} c_{jk}^{bc} \left\langle \Phi_i^a \,\middle|\, \hat{H} \,\middle|\, \Phi_{jk}^{bc} \right\rangle + \sum_{\substack{j<k \\ b<c}} c_{ijk}^{abc} \left\langle \Phi_i^a \,\middle|\, \hat{H} \,\middle|\, \Phi_{ijk}^{abc} \right\rangle = E_{\text{corr}}\, c_i^a \quad . \tag{2.64}$$

This can be repeated with higher excited determinants, to find a coupled set of equations that have to be solved simultaneously to obtain the CI coefficients and hence the correlation energy.

The expression for the correlation energy eq. (2.62) implies that it can be thought of as a sum of pair-energies e_{ij} for a given pair i and j, where the pair energy is given by

$$e_{ij} = \sum_{a<b} c_{ij}^{ab} \left\langle \Phi_0 \,\middle|\, \hat{H} \,\middle|\, \Phi_{ij}^{ab} \right\rangle \quad . \tag{2.65}$$

Since, in order to obtain the true pair energies e_{ij}, one would need to know all coefficients for higher excitations, i.e. solve the full CI problem, an alternative approach is to find approximations to e_{ij}. Historically, this leads to a multitude of approaches, which are often termed coupled-pair theories, one of the most successful descendants being the coupled cluster approximation.

One of the fundamental shortcomings of truncated CI is, that is not size consistent. That is, the energy of two subsystems A and B at large separations (such that they do not interact among each other) will not have the energy of the sum of the monomer calculations

$$E_{\text{A–B}}^{\text{CI}} \neq E_A^{\text{CI}} + E_B^{\text{CI}} \quad . \tag{2.66}$$

The reason for this can be seen if we consider the wavefunction of the super system

and subsystems in terms of the doubles CI method

$$\Psi^{\mathrm{CID}}_{\mathrm{A–B}} = \Phi^{\mathrm{HF}}_{\mathrm{A–B}} + \Phi^{\mathrm{D}}_{\mathrm{A–B}} \tag{2.67}$$

$$\Psi^{\mathrm{CID}}_{\mathrm{A}} = \Phi^{\mathrm{HF}}_{\mathrm{A}} + \Phi^{\mathrm{D}}_{\mathrm{A}} \tag{2.68}$$

$$\Psi^{\mathrm{CID}}_{\mathrm{B}} = \Phi^{\mathrm{HF}}_{\mathrm{B}} + \Phi^{\mathrm{D}}_{\mathrm{B}} \quad , \tag{2.69}$$

where Φ^{D} is the sum of all possible double excitations out of the reference Hartree-Fock determinant Φ^{HF}. The "true" wavefunction of the super systems, which is a product of the wavefunctions for the two subsystems

$$\tilde{\Psi}^{\mathrm{CID}}_{\mathrm{A–B}} = \Psi^{\mathrm{CID}}_{\mathrm{A}} \cdot \Psi^{\mathrm{CID}}_{\mathrm{B}} = \Phi^{\mathrm{HF}}_{\mathrm{A–B}} + \Phi^{\mathrm{D}}_{\mathrm{A–B}} + \Psi^{\mathrm{D}}_{\mathrm{A}} \cdot \Psi^{\mathrm{D}}_{\mathrm{B}} \quad , \tag{2.70}$$

carries an extra term for simultaneous double-excitations within both monomers, which is missing in the CID wavefunction of the super system. Furthermore, this shortcoming increases with the system size and hence becomes especially problematic for large systems such as crystals.[24]

2.4.3 Coupled Cluster Theory

2.4.3.1 Second Quantization

As argued in the last section, the expansion of the wavefunction in excited Slater determinants quickly leads to dimensions which cannot be handled routinely. An alternative approach to the CI method in generating a wavefunction expansion in excited determinants is provided by the so called Coupled-Cluster (CC) theory. This theory is most conveniently discussed in the context of second quantization, which introduces the concept of the Fock-space, as the space spanned by all possible determinants that can be formed from a given one-electron basis. The operators that act upon such determinants are formulated using so called creation and annihilation operators.

A creation operator $\hat{a}^{\dagger}_{p}$ is defined in its action on a reference determinant $|\phi_i \phi_j \dots \phi_s\rangle$, by adding a particle in state ϕ_p to the determinant

$$\hat{a}^{\dagger}_{p} |\phi_i \phi_j \dots \phi_s\rangle = |\phi_i \phi_j \dots \phi_p \dots \phi_s\rangle \quad . \tag{2.71}$$

Conversely, the annihilation operator $\hat{a}_p$ removes the particle in state ϕ_p from the

determiannt

$$\hat{a}_p \left|\phi_i\phi_j \ldots \phi_p \ldots \phi_s\right\rangle = \left|\phi_i\phi_j \ldots \phi_s\right\rangle \qquad . \tag{2.72}$$

A given determinant can therefore be constructed by action of a chain of creation operators onto the true vacuum state $|0\rangle$

$$\left|\Psi^{\mathrm{SD}}\right\rangle = a_p^\dagger a_q^\dagger \ldots a_s^\dagger \left|0\right\rangle = \left|\phi_p\phi_q \ldots \phi_s\right\rangle \qquad . \tag{2.73}$$

Since the wavefunction has to change sign when two columns of the Slater determinant are interchanged, pairwise permutation of two creation or annihilation operators

$$a_p^\dagger a_q^\dagger \left|0\right\rangle = \left|\phi_p\phi_q\right\rangle = -\left|\phi_q\phi_p\right\rangle = -a_q^\dagger a_p^\dagger \left|0\right\rangle \tag{2.74}$$

leads to the anti-commutation relations

$$\hat{a}_p^\dagger \hat{a}_q^\dagger + \hat{a}_q^\dagger \hat{a}_p^\dagger = 0 \qquad \hat{a}_p \hat{a}_q + \hat{a}_q \hat{a}_p = 0 \qquad \hat{a}_p^\dagger \hat{a}_q + \hat{a}_q \hat{a}_p^\dagger = \delta_{pq} \qquad . \tag{2.75}$$

Using these operators, we can define the so called (single orbital) cluster-operator

$$\hat{t}_i = \sum_a t_i^a a_a^\dagger a_i \qquad , \tag{2.76}$$

which when acting on a reference determinant, will create a linear combination of all possible determinants, where the particle in state ϕ_i has been replaced with a particle in state ϕ_a. This procedure can be extended to an arbitrary number of substitutions for the N orbital cluster operator

$$\hat{t}_{ij\ldots} = \sum_{a>b>\ldots>d} t_{ij\ldots}^{ab\ldots} \hat{a}_a^\dagger \hat{a}_b^\dagger \ldots \hat{a}_i \hat{a}_j \ldots \qquad . \tag{2.77}$$

Grouping all one orbital cluster operators into the total one orbital cluster operator

$$\hat{T}_1 = \sum_i \hat{t}_i = \sum_{ia} t_i^a \hat{a}_a^\dagger \hat{a}_i \qquad , \tag{2.78}$$

all two orbital cluster operators into the total two orbital cluster operator

$$\hat{T}_2 = \frac{1}{2} \sum_{ij} \hat{t}_{ij} = \frac{1}{4} \sum_{ij} \sum_{ab} t_{ij}^{ab} \hat{a}_a^\dagger \hat{a}_b^\dagger \hat{a}_j \hat{a}_i \tag{2.79}$$

and the N orbital cluster operators into the total N orbital cluster operator

$$\hat{T}_n = \left(\frac{1}{n!}\right)^2 \sum_{ij\ldots} \sum_{ab\ldots} t_{ij\ldots}^{ab\ldots} \hat{a}_a^\dagger \hat{a}_b^\dagger \ldots \hat{a}_i \hat{a}_j \ldots \quad , \tag{2.80}$$

we may write the total cluster operator as

$$\hat{T} = \sum_i \hat{T}_i \quad , \tag{2.81}$$

which when acting on a reference determinant will create the full CI expansion of the wavefunction.

2.4.3.2 The Coupled Cluster Ansatz

In contrast to the configuration interaction method, which successively adds (all) higher substituted determinants to the wavefunction expansion, coupled cluster (CC) parametrizes the wavefunction in terms of an exponential cluster-operator

$$|\Psi\rangle = \mathrm{e}^{\hat{T}} |\Phi_0\rangle \quad , \tag{2.82}$$

where $|\Phi_0\rangle$ is the reference (Hatree-Fock) determinant and the cluster operator $\hat{T}$ is defined in eq. (2.81). The advantage over the CI parametrization becomes apparent when one expands the cluster operator in terms of a Taylor series

$$\mathrm{e}^{\hat{T}} = 1 + \hat{T} + \frac{1}{2!}\hat{T}^2 + \ldots \tag{2.83}$$

$$= 1 + \hat{T}_1 + \hat{T}_2 + \frac{1}{2}\hat{T}_1^2 + \frac{1}{2}\hat{T}_1\hat{T}_2 + \frac{1}{2}\hat{T}_2\hat{T}_1 + \frac{1}{2}\hat{T}_2^2 + \ldots \quad , \tag{2.84}$$

which in contrast to the CI expansion not only carries the sum of the one-, two-, etc. electron excitation operators, but also products of operators, effectively generating higher substituted determinants when acting on a reference determinant. As a result of this expansion, the coupled cluster wavefunction retains the property of size-extensitivity at all levels of truncation.

However, one of the downsides of this approach is that the nonlinear parametrization of the wavefunction eq. (2.82) leads to complicated expression for the derivatives of the wavefunction with respect to the coupled cluster amplitudes t and consequently the minimization of the variational condition eq. (2.22) becomes a difficult task.

For this reason, in order to obtain an expression for the energy of the system, the usual eigenvalue equation

$$\hat{H}\mathrm{e}^{\hat{T}}\left|\Phi_0\right\rangle = E\,\mathrm{e}^{\hat{T}}\left|\Phi_0\right\rangle$$

is rewritten, by multiplying with $\mathrm{e}^{-\hat{T}}$ from the left

$$\mathrm{e}^{-\hat{T}}\hat{H}\mathrm{e}^{\hat{T}}\left|\Phi_0\right\rangle = E\left|\Phi_0\right\rangle$$

and subsequent projection against the reference determinant to obtain an expression for the energy

$$\left\langle \Phi_0 \middle| \hat{\bar{H}} \middle| \Phi_0 \right\rangle = E \qquad , \tag{2.85}$$

where

$$\hat{\bar{H}} = \mathrm{e}^{-\hat{T}}\hat{H}\mathrm{e}^{\hat{T}} \tag{2.86}$$

is the so called similarity transformed Hamiltonian. Analogously to the CI formalism, equations that determine the amplitudes are obtained by projection against excited determinants.

The advantage of this formalism is that the similarity-transformed Hamiltonian can be expressed in terms of a series of commutators of the exact Hamiltonian with the cluster operator, employing the so called Baker-Campbell-Hausdorff formula

$$\hat{\bar{H}} = \hat{H} + [\hat{H},\hat{T}] + \frac{1}{2!}\Big[[\hat{H},\hat{T}],\hat{T}\Big] + \frac{1}{3!}\Big[\Big[[\hat{H},\hat{T}],\hat{T}\Big],\hat{T}\Big] + \frac{1}{4!}\Big[\Big[\Big[[\hat{H},\hat{T}],\hat{T}\Big],\hat{T}\Big],\hat{T}\Big] \qquad , \tag{2.87}$$

which terminates after five terms in the expansion. The similarity-transformed Hamiltonian is no longer a hermitian operator and thus we get different left and right eigenvectors, describing the same state.

While this approach to determine the energy of the system under consideration no longer obeys the variational principle, the accuracy reached (at least starting with CCSD) is already sufficient to only marginally deviated from the variationally determined solution in many cases.[41]

2.4.4 Perturbation Theory

2.4.4.1 Formalism

An alternative approach to expanding the wavefunction into a sum of determinants is provided by means of Rayleigh-Schrödinger perturbation theory. Here, one solves an analogous, simplified problem and then tries to compute successive corrections to the model in order to retrieve the true behavior.

Assuming that we have found the eigenvalues $E_i^{(0)}$ and eigenfunctions $\Phi_i^{(0)}$ of some (unspecified) Hamiltonian $\hat{H}^{(0)}$, we may write a perturbation $\hat{V}^{(1)}$ (sometimes referred to as the fluctuation potential) to the system as

$$\left[\hat{H}^{(0)} + \lambda \hat{V}^{(1)}\right] \Psi_i(\lambda) = E_i(\lambda)\Psi_i(\lambda) \tag{2.88}$$

where $0 \leq \lambda \leq 1$ is a formal parameter.

Further expanding the (ground state) wavefunction Ψ_0 and eigenvalue E_0 into a power series in λ yields

$$\Psi_0(\lambda) = \sum_{n=0}^{\infty} \lambda^n \Psi_0^{(n)} \tag{2.89}$$

$$E_0(\lambda) = \sum_{n=0}^{\infty} \lambda^n E_0^{(n)} \quad , \tag{2.90}$$

where

$$\Psi_0^{(0)} = \Phi_0^{(0)} \quad . \tag{2.91}$$

For each power in λ, the Schrödinger equation 2.88 has to be fulfilled, i.e. each order in λ has to be fulfilled separately

$$\hat{H}^{(0)}\Psi_0^{(0)} = E^{(0)}\Psi_0^{(0)} \tag{2.92}$$

$$\hat{H}^{(0)}\Psi_0^{(1)} + \hat{V}^{(1)}\Psi_0^{(0)} = E^{(0)}\Psi_0^{(1)} + E_0^{(1)}\Psi_0^{(0)} \tag{2.93}$$

$$\hat{H}^{(0)}\Psi_0^{(2)} + \hat{V}^{(1)}\Psi_0^{(1)} = E^{(0)}\Psi_0^{(2)} + E_0^{(1)}\Psi_0^{(1)} + E_0^{(2)}\Psi_0^{(0)} \tag{2.94}$$

$$\vdots$$

Since the known eigenfunctions of $\hat{H}^{(0)}$ span a complete basis, we may expand

each contribution to the wavefunction in this basis

$$\Psi_0^{(n)} = \sum_j c_j^{(n)} \Phi_j^{(0)} \qquad . \tag{2.95}$$

Projecting onto the known basis functions $\Phi_i^{(0)}$ and requiring the so called intermediate norm

$$\left\langle \Phi_0^{(0)} \middle| \Psi_0^{(n)} \right\rangle \stackrel{!}{=} 1 \qquad , \tag{2.96}$$

we obtain an expression for $E_0^{(n)}$ and $\Psi_0^{(n)}$ for each order in n that only depends on lower orders. This is expressed in so called Wigner's $2n+1$ rule, which states that the correction to the energy of order $2n+1$ can be determined from wavefunctions of up to order n.[42]

The first order correction is thus just the expectation value of the undisturbed solutions with the perturbation operator

$$E_0^{(1)} = \left\langle \Phi_0^{(0)} \middle| \hat{V}^{(1)} \middle| \Phi_0^{(0)} \right\rangle \tag{2.97}$$

and the total energy is the expectation value of the perturbed Hamiltonian with the unperturbed eigenfunctions

$$E_0^{(0)} + E_0^{(1)} = \left\langle \Phi_0^{(0)} \middle| \hat{H}^{(0)} \middle| \Phi_0^{(0)} \right\rangle + \left\langle \Phi_0^{(0)} \middle| \hat{V}^{(1)} \middle| \Phi_0^{(0)} \right\rangle = \left\langle \Phi_0^{(0)} \middle| \hat{H} \middle| \Phi_0^{(0)} \right\rangle \qquad . \tag{2.98}$$

For the second order correction we obtain analogously

$$E_0^{(2)} = \sum_{k>0} \frac{\left| \left\langle \Phi_0^{(0)} \middle| \hat{V}^{(1)} \middle| \Phi_k^{(0)} \right\rangle \right|^2}{E_0^{(0)} - E_k^{(0)}} \qquad . \tag{2.99}$$

2.4.4.2 Møller-Plesset Perturbation Theory

In order to apply perturbation theory to the Hartree-Fock algorithm, we define the difference between the full electronic Hamiltonian $\hat{H}_{\text{elec}}$ and the Fock operator $\hat{F}$ eq. (2.33) as the fluctuation potential

$$\hat{V}^{(1)} = \hat{H}_{\text{elec}} - \hat{F} = \frac{1}{2} \sum_{\substack{k,l \\ k \neq l}} \frac{1}{|\vec{r}_k - \vec{r}_l|} - \sum_k \left(\hat{J}_k - \hat{K}_k \right) \qquad . \tag{2.100}$$

This variant of Rayleigh-Schrödinger perturbation theory is called Møller-Plesset perturbation theory of order N (MPN) and is one of the commonly applied

improvements over the Hartree-Fock procedure.

As shown above, the first order correction to the energy is simply the Hartree-Fock energy

$$E_0^{(0)} + E_0^{(1)} = \left\langle \Phi_0^{(0)} \middle| \hat{F} \middle| \Phi_0^{(0)} \right\rangle + \left\langle \Phi_0^{(0)} \middle| \hat{V}^{(1)} \middle| \Phi_0^{(0)} \right\rangle \tag{2.101}$$

$$= \left\langle \Phi_0^{(0)} \middle| \hat{F} \middle| \Phi_0^{(0)} \right\rangle + \left\langle \Phi_0^{(0)} \middle| \hat{H}_{\text{elec}} - \hat{F} \middle| \Phi_0^{(0)} \right\rangle \tag{2.102}$$

$$= \left\langle \Phi_0^{(0)} \middle| \hat{H}_{\text{elec}} \middle| \Phi_0^{(0)} \right\rangle = E_0^{\text{HF}} \quad . \tag{2.103}$$

For the second order correction, we obtain using Slater-Condon rules[33,34]

$$E_0^{(2)} = \sum_{i<j} \sum_{a<b} \frac{\left| \langle \phi_i \phi_j \parallel \phi_a \phi_b \rangle \right|^2}{\epsilon_i + \epsilon_j - \epsilon_a - \epsilon_b} \quad , \tag{2.104}$$

where indices i and j run over all occupied orbitals and a and b run over all unoccupied orbitals.

For a Hartree-Fock reference determinant, according to Brillouin's theorem, singly excited determinants do no directly mix with the reference and determinants that differ in more than two orbitals from the reference do not mix as a result of the Slater-Condon rules. Consequently, the first order correction to the wavefunction can be written as a linear combination of all doubly excited determinants $\left|\Phi_{ij}^{ab}\right\rangle$

$$\left|\Psi^{(1)}\right\rangle = \frac{1}{2} \sum_{ij} \sum_{ab} T_{ij}^{ab} \left|\Phi_{ij}^{ab}\right\rangle \quad , \tag{2.105}$$

where the expansion coefficients T_{ab}^{ij} are usually referred to as amplitudes.[43] For a closed-shell system, the second order correlation energy can then be expressed in terms of these amplitudes as

$$E_0^{(2)} = \sum_{ij} \sum_{ab} \left(2T_{ij}^{ab} - T_{ji}^{ab}\right) \langle ij \,|\, ab \rangle \quad . \tag{2.106}$$

In general, MP(2) perturbation theory is computationally less involved than CI and coupled cluster methods and is more comparable to hybrid DFT methods (vide infra), both in its complexity and quality of predictions.[44] However, a drawback is, that the perturbative expansion of the wavefunction is rather slowly converging, if at all. For some systems oscillatory or erratic behavior of the correlation energy for higher orders has been observed.[45] On the other side, one of the advantages

of this methodology is that it captures both short- and long-range contributions to the correlation energy, which is often a problem in commonly applied DFT methodologies.

2.4.5 Local and Density-Fitting Approximations

As was discussed, even for small systems on the order of a few atoms, the canonical form of the wavefunction expansion into Slater determinants as performed in the standard CI and CC approaches, quickly leads to dimensions which cannot be handled, even with massively parallel super-computers. This problem can be mitigated by truncating the expansion at an arbitrary level, however even for methods such as CISD or CCSD, there is still a steep computational scaling of the required time by a factor of $\sim N^6$ with the system size N.[46]

However, it was pointed out already more than 30 years ago, that the correlation effect is a local phenomenon[47] and that the steep scaling with the system size is an artifact of canonical orbitals obtained through the Hartree-Fock procedure, which are by default delocalized over the whole molecule.

Since the Hartree-Fock energy is invariant under unitary transformations of the Slater determinant, it is possible to find a representation of the wave function, in which the orbitals are localized to a certain region in space. Over the years, multiple procedures such as the Pipek-Mezey[48] or the Foster-Boys[49] localization algorithms have been suggested, which generally differ in how they "judge" localization, that is how they define the localization functional that is to be optimized.

Once a local basis has been found, it is possible to define a metric to calculate the "distance" between two localized basis functions and thus it is possible to restrict the list of electron pairs i and j to such which are spatially close together. Of course the threshold for when a pair of electrons is considered "far apart" is arbitrary, which often leads to a hierarchical scheme, where electron pairs that are considered "strong pairs" are treated at the maximum level of theory, while pairs that are "weak" or "distant" are treated at a less demanding level or neglected at all.[50]

In addition to the restriction of electron pairs, for each pair ij it is also possible to restrict the virtual space, that is the set of virtual orbitals to which a given pair of electrons are excited. Since the virtual space is generally harder to localize using algorithms as mentioned above, it is often represented by projecting out the occupied subspace from the atomic orbital (AO) basis set, since AOs are localized

by definition, resulting in the so called projected atomic orbitals (PAO).[51] Other approaches include the so called orbital-specific virtuals (OSV) basis, where the virtual space for a given occupied orbital i is defined as the MP2 virtual natural orbitals for a diagonal pair ii. The so called pair-domain, i.e. the virtual space for a given pair ij, is then the union of the the two sets for orbital i and j.[52]

For high accuracy calculations within the local approximation one often successively increases the allowed distances (or energy thresholds in case of OSVs) for orbitals that contribute to a domain. While PAOs are conceptually easier to use, they have the problem of "coarse-grained" domains, that is all basis functions on an atom are either included or not, which can lead to discontinuities on the potential energy surface when the domain changes, for example in a geometry relaxation. OSVs on the other hand adapt much better to these changes, but their drawback lies in the fact that they have a bias towards short-range correlation, resulting from their construction from the MP2 natural orbitals.

A further approximation that can drastically increase computational efficiency is the so-called density-fitting (also known as resolution of the identity) approach. Generally, the bottleneck in MP2 calculations is the evaluation of the four-index two-electron integrals $\langle ij \,|\, ab \rangle$, where orbitals i and a form a charge density product ϱ_{ia} for one coordinate and orbitals j and b for the other coordinate ϱ_{jb}. The idea behind density-fitting is to transform these integrals into three and two index quantities by expanding the charge density in a small auxiliary basis $\{\phi_p\}$

$$\varrho_{ia} = \sum_p d_{ia}^p \phi_p \qquad . \tag{2.107}$$

There are multiple approaches available on how to obtain the fitting coefficients d_{ik}^p and which choice to make for the auxilliary basis set $\{\phi_p\}$.[53–58] This approximation introduces only small errors but has profound consequences for the time required to complete the calculations.[59–61]

Over the years, all standard methods of computational chemistry such as CISD, CCSD(T), MPN, etc. haven been implemented using local correlation approaches. Together with the density-fitting approach this led to linear scaling algorithms that allowed system sizes to be treated which where in the domain of density functional theory up to that point.[62–66]

2.5 Density Functional Theory

While the Hartree-Fock algorithm provides a starting point for a large collection of so called post Hartree-Fock methods, which include the most accurate descriptions of the electronic structure we have, the inherent description of the wavefunction as an expansion in a basis of Slater determinants quickly precludes computational tractability, even for systems in the range of a few atoms. An alternative approach for how to determine all properties of a quantum mechanical system was put forward first by Llwellyn and Fermi[67,68] and then theoretically justified by Kohn and Hohenberg using a reductio ad absurdum.[69] In this approach, one is not interested in finding the wavefunction Ψ of the system, but one formulates all properties in terms of the electronic density $\varrho(\vec{r})$, which only explicitly depends on the three Cartesian coordinates x, y and z (and possibly the spin coordinate σ), instead of the $3N$ independent coordinates that appear in the Schrödinger equation 2.5 and thus in the wavefunction.

In order to prove, that for a given external potential $\hat{V}_{\text{ext}}$, there is only one unique electronic density associated with it, Hohenberg and Kohn showed that if the variational principle holds, the expectation value of the Hamiltonian $\hat{H} = \hat{T} + \hat{V}_{ee} + \hat{V}_{\text{ext}}$ with the true ground state wavefunction Ψ_0 must be lower than for any other trial wavefunction Ψ_0', which in turn is the ground-state of the Hamiltonian $\hat{H}' = \hat{T} + \hat{V}_{ee} + \hat{V}'_{\text{ext}}$:

$$\left\langle \Psi_0 \middle| \hat{H} \middle| \Psi_0 \right\rangle < \left\langle \Psi_0' \middle| \hat{H} \middle| \Psi_0' \right\rangle \quad . \tag{2.108}$$

Of course, the same must hold for $\hat{H}'$:

$$\left\langle \Psi_0' \middle| \hat{H}' \middle| \Psi_0' \right\rangle < \left\langle \Psi_0 \middle| \hat{H}' \middle| \Psi_0 \right\rangle \quad . \tag{2.109}$$

Since $\hat{H}$ and $\hat{H}'$ are the same except for the external potentials $\hat{V}_{\text{ext}}$ and $\hat{V}'_{\text{ext}}$, addition of the two inequalities yields

$$\left\langle \Psi_0 \middle| \hat{V}_{\text{ext}} \middle| \Psi_0 \right\rangle + \left\langle \Psi_0' \middle| \hat{V}'_{\text{ext}} \middle| \Psi_0' \right\rangle < \left\langle \Psi_0' \middle| \hat{V}_{\text{ext}} \middle| \Psi_0' \right\rangle + \left\langle \Psi_0 \middle| \hat{V}'_{\text{ext}} \middle| \Psi_0 \right\rangle \quad . \tag{2.110}$$

However, since $\hat{V}_{\text{ext}}$ is a multiplicative potential, the expectation value simply is

the potential multiplied by the electronic density integrated over the full domain:

$$\int \hat{V}_{\text{ext}} \varrho_0 \, \mathrm{d}\vec{r} + \int \hat{V}'_{\text{ext}} \varrho'_0 \, \mathrm{d}\vec{r} < \int \hat{V}_{\text{ext}} \varrho'_0 \, \mathrm{d}\vec{r} + \int \hat{V}'_{\text{ext}} \varrho_0 \, \mathrm{d}\vec{r} \qquad . \tag{2.111}$$

Thus, if the two electronic densities were equal $\varrho_0 = \varrho'_0$, it follows directly that they must belong to the same external potentials. In other words, the ground state energy for a given external potential is a unique functional of the electronic density.

Unfortunately, this relationship merely proofs the uniqueness of the electronic density, however it does not provide means of determining this density. In order to do so, one reformulates the variational principle in terms of a constrained search:[70]

$$E_0 = \min_{\Psi \to N} \left\langle \Psi \,\middle|\, \hat{H} \,\middle|\, \Psi \right\rangle = \min_{\Psi \to N} \left\langle \Psi \,\middle|\, \hat{T} + \hat{V}_{ee} + \hat{V}_{\text{ext}} \,\middle|\, \Psi \right\rangle \tag{2.112}$$

$$= \min_{\varrho \to N} \left\{ \min_{\Psi \to \varrho} \left\langle \Psi \,\middle|\, \hat{T} + \hat{V}_{ee} + \hat{V}_{\text{ext}} \,\middle|\, \Psi \right\rangle \right\} \tag{2.113}$$

$$= \min_{\varrho \to N} \left\{ \min_{\Psi \to \varrho} \left\langle \Psi \,\middle|\, \hat{T} + \hat{V}_{ee} \,\middle|\, \Psi \right\rangle + \int \hat{V}_{\text{ext}} \varrho \, \mathrm{d}\vec{r} \right\} \tag{2.114}$$

$$= \min_{\varrho \to N} \left\{ F[\varrho] + \int \hat{V}_{\text{ext}} \varrho \, \mathrm{d}\vec{r} \right\} \qquad , \tag{2.115}$$

with the so called Hohenberg-Kohn functional

$$F[\varrho] = \min_{\Psi \to \varrho} \left\langle \Psi \,\middle|\, \hat{T} + \hat{V}_{ee} \,\middle|\, \Psi \right\rangle \qquad . \tag{2.116}$$

The outer minimization of the energy functional over all wavefunctions that reproduce the specified number of electrons is constrained by the inner minimization over all such wavefunctions which yield a given, i.e. the lowest energy, electronic density. Since the external potential does not depend on the electronic density, its expectation value can be ignored in the inner minimization of the Hohenberg-Kohn functional. As a result of the outer constraint over the search of all wavefunctions that reproduce the correct number of electrons, linear variations of the resulting Euler-Lagrange equation have to be constant at the minimum:

$$\frac{\delta \left\{ F[\varrho] + \int \hat{V}_{\text{ext}} \varrho \, \mathrm{d}\vec{r} \right\}}{\delta \varrho} = \mu \qquad \Leftrightarrow \qquad \frac{\delta F[\varrho]}{\delta \varrho} + \hat{V}_{\text{ext}} = \mu \qquad . \tag{2.117}$$

The solution of this equation yields the ground state density ϱ_0 and consequently

the inner minimization of eq. (2.116)

$$\min_{\Psi\to\varrho}\left\langle\Psi\left|\hat{T}+\hat{V}_{ee}\right|\Psi\right\rangle \qquad \Rightarrow \Psi_0=\Psi[\varrho_0] \tag{2.118}$$

defines the ground state wavefunction as a functional of this ground state density.

In order to define the Hohenberg-Kohn functional $F[\varrho]$, the problem of N interacting electrons is mapped onto one with N non-interacting electrons moving in an effective potential $\hat{V}_s$, for which the Schrödinger equation reads

$$\hat{H}_s\Phi_0=\left(\hat{T}+\hat{V}_s\right)\Phi_0=E_{s,0}\Phi_0 \qquad , \tag{2.119}$$

where the effective potential is a sum of one-electron operators

$$\hat{V}_s=\sum_i v_s(\vec{r}_i) \qquad . \tag{2.120}$$

The Slater determinant that is constructed from the non-interacting one-electron functions is called the Kohn-Sham determinant, after Walter Kohn and Lu Jeu Sham, who introduced the concept in 1965.[71] Since, the effective potential is also multiplicative, the analogous constrained search yields

$$E_{s,0}=\min_{\varrho\to N}\left\{\min_{\Psi\to\varrho}\left\langle\Psi\left|\hat{T}\right|\Psi\right\rangle+\int\hat{V}_s\varrho\;\mathrm{d}\vec{r}\right\} \qquad , \tag{2.121}$$

which defines the *non-interacting* kinetic energy functional $T_s[\varrho]$ and thus the wavefunction Φ which satisfies this minimization is a functional of the electronic density:

$$T_s[\varrho]=\min_{\Psi\to\varrho}\left\langle\Psi\left|\hat{T}\right|\Psi\right\rangle \qquad \Rightarrow \qquad \Phi_0=\Phi[\varrho_0] \qquad . \tag{2.122}$$

The corresponding Euler-Lagrange equation then defines the effective potential in terms of the non-interacting kinetic energy

$$\left.\frac{\delta T_s[\varrho]}{\delta\varrho}\right|_{\varrho=\varrho_0}+V_s=\mu \qquad \Leftrightarrow \qquad \hat{V}_s=-\left.\frac{\delta T_s[\varrho]}{\delta\varrho}\right|_{\varrho=\varrho_0}+\mu \qquad . \tag{2.123}$$

Collecting these two systems, we can define the exchange E_x and correlation

energy E_c functionals as

$$E_x = \left\langle \Phi[\varrho] \middle| \hat{V}_{ee} \middle| \Phi[\varrho] \right\rangle - U[\varrho] \tag{2.124}$$

$$E_c = \left\langle \Psi[\varrho] \middle| \hat{T} + \hat{V}_{ee} \middle| \Psi[\varrho] \right\rangle - \left\langle \Phi[\varrho] \middle| \hat{T} + \hat{V}_{ee} \middle| \Phi[\varrho] \right\rangle \quad , \tag{2.125}$$

where

$$U[\varrho] = \frac{1}{2} \iint \frac{\varrho(\vec{r})\varrho(\vec{r}')}{|\vec{r} - \vec{r}'|} \, \mathrm{d}\vec{r} \, \mathrm{d}\vec{r}' \tag{2.126}$$

is the classical electrostatic interaction of the charge-density.

This enables us to rewrite the Hohenberg-Kohn functional purley in terms of the electronic density ϱ:

$$F[\varrho] = T_s[\varrho] + U[\varrho] + E_x[\varrho] + E_c[\varrho] \quad . \tag{2.127}$$

The crucial step now is, that we map the problem of the interacting electrons onto the problem of non-interacting electrons in such a way, that both electronic densities are the same. If this is possible, we can determine the effective potential of the non-interacting system by plugging the Hohenberg-Kohn functional eq. (2.127) into the Euler-Lagrange eq. (2.117) and solve for $\hat{V}_{\mathrm{ext}}$ to obtain

$$\hat{V}_{\mathrm{ext}}(\vec{r}) = -\frac{\delta T_s[\varrho]}{\delta \varrho} - \hat{V}_{\mathrm{H}} - \hat{V}_{\mathrm{x}} - \hat{V}_{\mathrm{c}} + \mu \tag{2.128}$$

with

$$\hat{V}_{\mathrm{H}} = \frac{\delta U[\varrho]}{\delta \varrho} \tag{2.129}$$

$$\hat{V}_{\mathrm{x}} = \frac{\delta E_x[\varrho]}{\delta \varrho} \tag{2.130}$$

$$\hat{V}_{\mathrm{c}} = \frac{\delta E_c[\varrho]}{\delta \varrho} \quad . \tag{2.131}$$

and plugging eq. (2.128) into eq. (2.123) to obtain

$$\hat{V}_s(\vec{r}) = \hat{V}_{\mathrm{ext}} + \hat{V}_{\mathrm{H}} + \hat{V}_x + \hat{V}_c \quad . \tag{2.132}$$

This is an effective one-electron operator and thus one can decouple the Kohn-

Sham equations

$$\left[\hat{T} + \hat{V}_s\right] \Phi_0 = E_{s,0} \Phi_0 \tag{2.133}$$

into N single particle equations

$$\left[\hat{T} + \hat{V}_s\right] \phi_i = \epsilon_i \phi_i \qquad , \tag{2.134}$$

and the ground state energy of the interacting system with the same density as the non-interacting system becomes

$$E_0 = F[\varrho_0] + \int \hat{V}_{\text{ext}}\, \varrho_0 \, \mathrm{d}\vec{r} \tag{2.135}$$

$$= \left\langle \Phi_0 \middle| \hat{T} \middle| \Phi_0 \right\rangle + U[\varrho_0] + E_x[\varrho_0] + E_c[\varrho_0] + \int \hat{V}_{\text{ext}} \varrho_0 \, \mathrm{d}\vec{r} \qquad . \tag{2.136}$$

Unfortunately, the exact functional dependence of the correlation energy is unknown. For this reason, approximate functionals have to be introduced. One of the consequences of this is that, even though in principle the exact functional of the exchange energy is known, in most modern implementations both the correlation as well as the exchange energy are approximated, so as to exploit mutual error compensation between these terms. Over the years, a vast number of approximative functionals have been proposed, with the first one used being the so called local (spin) density approximation L(S)DA, which employs the correlation energy of a system of homogeneously distributed charge density in a constant positive background potential. For this system the functional dependence of the exchange energy is given by

$$E_x^{\text{LDA}} = c \int \varrho^{4/3} \, \mathrm{d}\vec{r} \tag{2.137}$$

where c is a parameter that is not unambiguously defined, since the exchange in the free electron case varies with the wavenumber.[72] The correlation energy can be approximated to high degrees of accuracy in terms of the correlation energy density $\epsilon_c^{\text{LDA}}(\varrho)$:

$$E_c^{\text{LDA}} = \int \varrho \epsilon_c^{\text{LDA}}(\varrho) \, \mathrm{d}\vec{r} \qquad . \tag{2.138}$$

The success of this method is partially resulting from the fact, that the LDA approximation yields remarkably reasonable results considering its simplicity, especially for metallic systems.[73] For more complex systems, such as molecular crystals or surface chemistry, the accuracy often lacked, which lead to the development of

a cornucopia of functionals, which try to improve on the simple model in various ways.[74–77] One of the most commonly used approximations are the so called generalized gradient approximations (GGA), which not only depend on the density itself, but also on the gradient of the density.[78–81]

One of the key shortcomings of the Kohn-Sham formalism is the so called self interaction error (SIE): Within the Hartree-Fock formalism, the one-body terms of the electron interacting with itself in the coulomb operator is exactly canceled by the corresponding terms in the exchange potential; An electron does not interact with itself. However, since in the Hohenberg-Kohn functional, the energy is computed from the singe-particle density, each electron interacts with the full density, including itself.[82] One of the approaches that tries to improve upon this shortcoming are the so called hybrid-exchange functionals, which include parts of an exchange-potential which is calculated according to the Hartree-Fock exchange eq. (2.35), using the Kohn-Sham orbitals. This does not completely remedy the problem, as the exact amount of HF exchange that is to be mixed into the functional is not obvious and different amounts perform differently well.[82–84] On top of that other approaches are pursued, for example double-hybrid methods that add a perturbative (MP2) treatment of the correlation energy as well as parts of the HF exchange,[85,86] or so called range-separated functionals, which mix in different amounts of HF exchange and MP2 correlation depending on the spatial distance between two points.[87,88]

While these approaches include more and more sophisticated techniques on how to overcome the inherent deficiencies present, which is why this ordering is often referred to as "Jacobs ladder" in DFT, there is no actual true hierarchical way of how to systematically remove errors. As a result, a zoo of functional approximations exists, some of which try to be as generally applicable as possible, while others are specifically tailored for special purpose calculations. In practical calculations, one often has to balance between computational cost and available resources. One of the standard approaches that has evolved over the years is the combination of a GGA type functional with an additional empirical long-range dispersion correction, such as Grimme type or Tkatchenko-Scheffler corrections.[89,90] While this is generally a reasonable compromise for structure determination, certain known deficiencies of GGA functionals have to be taken into account. For example it is well known, that PBE in general over-binds and underestimates reaction barriers due to SIE.[91,92]

2.6 Treatment of Periodic Systems

2.6.1 Bravais Lattice and Bloch's Theorem

So far, all methods were formulated in terms of a set of discrete nuclear coordinates that define the molecular configuration and therefore the external potential. While this approach lends itself naturally to the description of molecular systems, problems arise when one tries to also describe condensed matter, such as crystalline solids, liquids or amorphous substances like glass. These systems are usually comprised of a number of atoms in the region of Avogadro's constant, rendering a discrete molecular description immediately impossible, even for the simplest of approximations. To cope with these problems, two different approaches are usually employed:

On the one hand, there is the so called cluster approach, where one tries to mimic the behavior of the full solid with a small cluster of atoms. Naturally, this approach has the same scaling problems as molecular calculations and further more, the ratio of surface to bulk volume will be strongly skewed, even for moderately sized clusters, introducing artificial effects into the system, that have to be either compensated by saturating surface atoms with for example hydrogen atoms, or embedding the whole cluster into a background charge that mimics the electrostatic effect of the omitted crystal.

This thesis will however focus on the concept of a Bravais lattice and the resulting description of the material as an infinitely repeating, perfectly periodic structure, by virtue of Bloch's theorem. As iterated above, macroscopic solids are comprised of a huge number of constituting particles, arranged into a crystalline structure, which itself is, disregarding irregularities, composed of a periodically repeating arrangement of atoms, termed the unit cell. Since, the number of unit cells is so large, it is justified to assume the periodicity to be infinite as long as surface phenomena or symmetry breaking structures, such as the amorphous structure of glass, do not play a key role.

Mathematically, the Bravais lattice is defined for a chosen unit cell with unit cell vectors $\{\vec{a}_i\}$, as the set of all coordinates $\{\vec{R}\}$ that satisfy the condition

$$\{\forall m_i \in \mathbb{Z} | \vec{R} = \sum_i m_i \vec{a}_i\} \qquad . \tag{2.139}$$

In other words, all translations $\hat{T}_{\vec{R}}$ that translate any coordinate by a linear

combination of the unit cell vectors leaves the whole system invariant. The atoms, that are placed in a unit cell are called the crystallographic basis. In the simplest case, the unit cell only contains a single atom, in which case the whole crystal will possess the symmetry of the point group describing the Bravais lattice. However, in principle the symmetry of the basis can be different from the symmetry of the Bravais lattice itself, leading to the concept of space groups.

Within the description of periodic structures, it is convenient to introduce the so called reciprocal lattice. For a given direct space unit cell with unit cell vectors $\{\vec{a}_1, \vec{a}_2, \vec{a}_3\}$, the reciprocal lattice is defined as

$$\vec{b}_1 = 2\pi \frac{\vec{a}_2 \times \vec{a}_3}{\langle \vec{a}_1 \,|\, \vec{a}_2 \times \vec{a}_3 \rangle} \tag{2.140}$$

$$\vec{b}_2 = 2\pi \frac{\vec{a}_3 \times \vec{a}_1}{\langle \vec{a}_2 \,|\, \vec{a}_3 \times \vec{a}_1 \rangle} \tag{2.141}$$

$$\vec{b}_3 = 2\pi \frac{\vec{a}_1 \times \vec{a}_2}{\langle \vec{a}_3 \,|\, \vec{a}_1 \times \vec{a}_2 \rangle} \tag{2.142}$$

The definition immediately results in the fact, that the scalar product between a Bravais lattice vector and a reciprocal lattice vector is equal to

$$\left\langle \vec{b}_i \,\middle|\, \vec{a}_i \right\rangle = 2\pi \; \delta_{ij} \qquad . \tag{2.143}$$

Since the system is invariant under any of the translations belonging to the Bravais lattice, the one-electron wavefunctions have to be eigenfunctions of all translational operators belonging to the lattice $\hat{T}_{\vec{R}}\psi(\vec{r}) = \psi(\vec{r} + \vec{R}) = t_{\vec{R}}\psi(\vec{R})$. Requiring normalization means, the wavefunction can differ at most by a phase factor upon translation

$$\hat{T}_{\vec{R}_i}\psi(\vec{r}) = \mathrm{e}^{2\pi \mathrm{i} \phi_i}\psi(\vec{r}) \qquad i \in \{x, y, z\} \qquad \phi_i \in \mathbb{R} \qquad . \tag{2.144}$$

For an arbitrary translation $n_1\vec{a}_1 + n_2\vec{a}_2 + n_3\vec{a}_3$, we thus may write $\vec{k} = \phi_1\vec{b}_1 + \phi_2\vec{b}_2 + \phi_3\vec{b}_3$ and defining the Bloch factor $u_{\vec{k}}(\vec{r})$ as

$$u_{\vec{k}}(\vec{r}) = \mathrm{e}^{-\mathrm{i}\vec{k}\cdot\vec{r}}\psi(\vec{r}) \qquad , \tag{2.145}$$

we can see that the eigenfunctions of the translational operators can be written as

$$\psi_{\vec{k}}(\vec{r}) = \mathrm{e}^{\mathrm{i}\vec{k}\cdot\vec{r}}u_{\vec{k}}(\vec{r}) \qquad , \tag{2.146}$$

where the Bloch factor $u_{\vec{k}}(\vec{r})$ possesses the full symmetry of the Bravais lattice, i.e. $\hat{T}_{\vec{R}}\, u_{\vec{k}}(\vec{r}) = u_{\vec{k}}(\vec{r})$. These wavefunctions are called Bloch functions, after Felix Bloch, who derived them in his work on periodic systems.[93]

Since the Hamiltonian operator reflects the symmetry of the Bravais lattice via the external potential of the nuclei, the Hamiltonian has to commute with all translational operators of the Bravais lattice and consequently, both have a common set of eigenfunctions.

Furthermore, the Bloch functions as defined above, are only unique up to a constant reciprocal lattice vector $\vec{K}$, i.e. $\psi_{\vec{k}+\vec{K}}(\vec{r}) = \psi_{\vec{k}}(\vec{r})$. Consequently the set of vectors $\vec{k}$ may be restricted to the set of unique vectors with the lowest $\vec{k}$. This set is geometrically equivalent to the Wigner-Seitz cell (the locus of points in space that are closer to a reference lattice point, than to any of the other lattice points.) in real space and is called the first Brillouin zone.

2.6.2 The Periodic LCAO Ansatz

While plane waves are a natural basis for the description of electron states in periodic potentials, their inherent delocalized nature creates problems for electronic states that are localized in their extent, such as tightly bound core-states. Generally this problem is solved by invoking the frozen core approximation and representing these core-states with an effective potential, centered on the respective atom. The Hamiltonian is then only constructed for the valence states, which interact with the effective core-potential. This approach, combined with density functional theory and various levels of exchange-correlation functionals to solve the resulting periodic Kohn-Sham equations, is the standard for routinely carried out calculations.

Clearly, when trying to reach high levels of accuracy, it is desirable to explicitly treat these core states with one-electron functions too. Of course, plane-waves are, albeit a very natural one, just one possible choice of basis functions. In order to introduce a LCAO ansatz akin to the Rothaan-Hall equations, any basis function that is chosen has to fulfill Bloch's theorem in eq. (2.146). To do so, one forms linear combinations $X_l^{\vec{k}}$ of all atomic basis functions χ_l in the lattice of a given type

$$X_l^{\vec{k}}(\vec{r}) = \sum_{\vec{R}} \mathrm{e}^{\mathrm{i}\vec{k}\cdot\vec{R}} \chi_l(\vec{r} - \vec{Q} - \vec{R}) \qquad , \tag{2.147}$$

where the sum runs over all vectors $\vec{R}$ of the Bravais lattice and $\vec{Q}$ is the position

of the atom in the reference cell. With this, we can form the ansatz

$$\psi_{\vec{k},i}(\vec{r}) = \sum_l c_l^{\vec{k},i} X_l^{\vec{k}}(\vec{r}) \qquad , \tag{2.148}$$

for the one electron orbitals, where the sum runs over all atoms and all basis functions on that atom. Plugging this equation into the eigenvalue equation and projecting from the left with $\langle\chi_m|$, we arrive at

$$\sum_l H_{ml}^{\vec{k}}\, c_l^{\vec{k},i} = \varepsilon_{\vec{k},i} \sum_l S_{ml}^{\vec{k}}\, c_l^{\vec{k},i} \qquad , \tag{2.149}$$

with

$$H_{ml}^{\vec{k}} = \sum_{\vec{R}} \left\langle \chi_m \middle| \hat{H} \middle| \chi_l \right\rangle \mathrm{e}^{\mathrm{i}\vec{k}\cdot\vec{R}} \qquad \text{and} \qquad S_{ml}^{\vec{k}} = \sum_{\vec{R}} \langle \chi_m \,|\, \chi_l \rangle \, \mathrm{e}^{\mathrm{i}\vec{k}\cdot\vec{R}} \qquad , \tag{2.150}$$

or in compact matrix notation

$$\mathbf{H}^{\vec{k}} \mathbf{c}^{\vec{k},i} = \varepsilon_{\vec{k},i}\, \mathbf{S}^{\vec{k}}\, \mathbf{c}^{\vec{k},i} \qquad . \tag{2.151}$$

This is again a self-consistent formalism, and depending on which effective one-electron Hamiltonian is chosen, i.e. DFT or HF, the resulting solution yields the ground state energy per unit cell of the crystal.

2.6.3 Fragment Embedding Techniques

Since it is known, that the periodic HF solution lacks in accuracy because it is affected by systematic errors stemming from the neglect of dynamical correlation,[94] it would be advantageous to apply the aforementioned methods such as perturbation theory and the cluster expansion, to correct for these deficiencies. From a principle point of view, this is possible, however the fact that the system is represented as an infinite Bravais lattice, introduces problems when computing the correlation energy.

However, often the "interesting" parts of quantum chemical models are confined to a small part of the system, being embedded in a chemical environment. An example are adsorbed species on a surface: while the surface is essential for providing the environment in which a reaction may occur, the reaction itself involves only a few of the atoms at the reaction site. It it thus a natural idea to

invoke the local approximation and define a cluster of functions that are localized on the interesting parts of the model and use these as a basis for an additional higher-level treatment. The immediate advantage of this approach is, that there is no actual "cutting" of bonds required, as it would be if one tries to represent the crystal as a finite cluster, since the fragment's orbitals are orthogonal to the occupied manifold of the environment by construction. Thus, the chosen cluster of orbitals can simply be embedded in the field of the periodic crystal, by including the coulomb and exchange potential from the full periodic Hamiltonian in the fragment's one-electron Hamiltonian

$$h_{pq}^{\text{frag}} := F_{pq}^{\text{cryst}} - \sum_{i \in \text{frag}}^{\text{occ}} \Big[2 \langle pi \,|\, qi \rangle - \langle pi \,|\, iq \rangle \Big] \tag{2.152}$$

$$= F_{pq}^{\text{cryst}} + \sum_{i \notin \text{frag}}^{\text{occ}} \Big[2 \langle pi \,|\, qi \rangle - \langle pi \,|\, iq \rangle \Big] \quad . \tag{2.153}$$

In this approach, the Hartree-Fock energy and the nuclear repulsion energy (since there are no actual nuclei associated with the fragment) are not uniquely defined.[95] In our methodology, we chose the nuclear repulsion energy such, that the total Hartree-Fock energy of the fragment coincides with the HF energy of the periodic crystal. Once the fragment has been defined it can in principle be subjected to any post-HF method of choice.

2.7 Thermodynamic Properties from First Principles

So far, it was discussed how to extract the wavefunction from the Schrödinger equation. In this section, we make the connection between quantum mechanics and thermodynamics, which was historically developed in order to understand and exploit the processes that were involved in optimizing the steam engine.[96]

Many influential scientists of the 17$^{\text{th}}$ and 18$^{\text{th}}$ century were involved in deriving the laws, that – until the advent of the electric motor in the early 19$^{\text{th}}$ century – governed the society of the industrial age. One of the concepts that emerged from this process, is the idea of entropy. It was observed, that the amount of work that was extractable when a gas was heated or cooled, was less than the heat that was provided to the system. This idea was first put on a mathematical basis by Clausius,[97] as the infinitesimal amount of heat $\mathrm{d}Q_{\text{rev}}$, that is reversibly transferred to the system at Temperature T

$$\mathrm{d}S = \frac{\mathrm{d}Q_{\text{rev}}}{T} \quad . \tag{2.154}$$

From this Josiah Gibbs introduced the free energy G as a function of state,[98] which is minimized in any system that is in thermodynamic equilibrium as

$$G = H - TS = U + pV - TS \quad . \tag{2.155}$$

Here H is the enthalpy of the system, i.e. the sum of internal energy U and volumetric work pV. The difference in free energy when changing reversibly from one state to another is equal to the maximum amount of work that can be extracted from the system.

A more fundamental explanation was provided by Ludwig Boltzmann,[99] who famously derived the Entropy as a measure of the amount of possible micro-states Ω of a given system, that reproduce the observed macroscopic state

$$S = \mathrm{k_B} \log \Omega \quad , \tag{2.156}$$

which is often more conviently expressed in terms of the probability p_i of the systems being in the i-th state

$$S = -\mathrm{k_B} \sum_i p_i \log p_i \quad . \tag{2.157}$$

This also makes the connection to quantum mechanics, which provides the means to access the probabilities p_i of the system being in the i-th micro-state, using the Boltzmann probability distribution

$$p_i = \frac{1}{q} \mathrm{e}^{-\frac{\varepsilon_i}{\mathrm{k_B} T}} = \frac{\mathrm{e}^{-\frac{\varepsilon_i}{\mathrm{k_B} T}}}{\sum_j \mathrm{e}^{-\frac{\varepsilon_j}{\mathrm{k_B} T}}} \quad , \tag{2.158}$$

with the energy ε_i of the i-th state of the system and the canonical partition function

$$q = \sum_j \mathrm{e}^{-\frac{\varepsilon_j}{\mathrm{k_B} T}} \quad , \tag{2.159}$$

which results from the fact that the total probability $\sum_i p_i$ must add up to unity.[100]

2.7.1 Thermodynamic State and Partition Functions

We only give a short outline of the thermodynamic formulation required for the description of our system. Further information can be found in the relevant literature.[100]

Our goal is to compute the standard Gibbs free energy G^0 (we drop the superscript 0 for simplicity) for all points on the potential energy surface (PES) that are relevant for the reaction kinetics. We start from the standard definition of the Gibbs free energy

$$G(T,p) = H - TS \tag{2.160a}$$

$$= U + pV - TS \quad , \tag{2.160b}$$

with the enthalpy H, internal energy U, entropy S, Volume V (all per particle), pressure p and temperature T, which is minimized in any system under isothermal ($\mathrm{d}T = 0$) and isobaric conditions ($\mathrm{d}p = 0$). For any reaction only including condensed matter, the contribution pV will be negligible, since $V_{gas} \gg V_{condensed} \approx 0$, while for steps including particles in the gas phase we invoke the ideal gas law and set $pV = \mathrm{k_B} T$, where $\mathrm{k_B}$ is Boltzmann's constant. Internal energy U and entropy S are readily available from the total partition function q_{tot} of the system and its internal energy at zero temperature $U_{T=0\,\mathrm{K}} = E_{electronic} + \frac{1}{2}\sum_i \epsilon_i$, where ϵ_i

is the energy of the i-th vibrational mode:

$$U = \mathrm{k_B} T^2 \frac{\partial}{\partial T} \ln q_{tot} + U_{T=0\,\mathrm{K}} \tag{2.161}$$

$$S = \mathrm{k_B} \ln q_{tot} + \mathrm{k_B} T \frac{\partial}{\partial T} \ln q_{tot} \tag{2.162}$$

Plugging eqs. (2.161) and (2.162) into eq. (2.160b), we arrive at

$$G = \begin{cases} U_{T=0\,\mathrm{K}} - \mathrm{k_B} T \ln q_{tot} + \mathrm{k_B} T & \text{(gas phase)} \quad (2.163a) \\ U_{T=0\,\mathrm{K}} - \mathrm{k_B} T \ln q_{tot} & \text{(condensed matter)} \quad (2.163b) \end{cases}$$

The real total partition function q_{tot}, which is required to calculate the enthalpy and entropy according to eqs. (2.161) and (2.162) is approximated as a product of the individual contributions from vibration, translation and rotation of the system under study:

$$q_{tot} = \prod_i q_i = \begin{cases} q_{trans}^{\mathrm{3D}} \cdot q_{rot} \cdot q_{vib} & \text{(gas phase)} \quad (2.164a) \\ q_{vib} & \text{(condensed matter)} \quad ,(2.164b) \end{cases}$$

where i runs over all degrees of freedom. Again, for any system only including condensed matter, there are no more free translations or rotations possible, while for the gas phase we approximate the rotational and translational contribution by using the standard partition functions of a symmetric, rigid free gas particle of mass m:

$$q_{trans}^{\mathrm{3D}} = \frac{V}{\Lambda^3} = V \cdot \frac{(2\pi\ m\ \mathrm{k_B} T)^{3/2}}{h^3} = \frac{(\mathrm{k_B} T)^{5/2}}{p} \times \frac{(2\pi\ m)^{3/2}}{h^3} \tag{2.165}$$

$$q_{rot} = \begin{cases} q_{rot}^{\mathrm{linear}} = \dfrac{8\pi^2\ I\ \mathrm{k_B} T}{\sigma\ h^2} & (2.166a) \\ q_{rot}^{\mathrm{general}} = \left(\dfrac{8\pi^2\ \mathrm{k_B} T}{h^2}\right)^{3/2} \cdot \dfrac{\sqrt{\pi\ I_A\ I_B\ I_C}}{\sigma} \quad , & (2.166b) \end{cases}$$

where h is Planck's constant, I is the moment of inertia of a linear molecule, I_A, I_B and I_C are the diagonal components of the inertia tensor for any molecule and

σ is a symmetry factor ($\sigma_{H_2O} = \sigma_{H_2} = 2$). The vibrational contribution is given by

$$q_{vib} = \prod_i \left[1 - \exp\left(-\frac{\epsilon_i}{k_B T}\right)\right]^{-1} \quad , \tag{2.167}$$

where ϵ_i is the energy of the i-th vibrational eigenmode. Note, that we do not include the electronic degrees of freedom in the partition function, since we assume that only the electronic ground state is populated and its contribution is included in the term $U_{T=0\,K}$ within the calculation of the free energy.

2.7.2 Transition State Theory and Rate Equations

We follow Chorkendorff and Niemantsverdriet[101] in the derivation of the transition state theory equations. Within the concept of the potential energy surface (PES), stable molecular geometries are characterized as a minimum on the PES. In order for a chemical reaction to occur, the atomic configuration that is representing the initial minimum has to change into a different geometry, which is also (albeit possibly higher or lower in potential energy) a minimum on the PES. Obviously, in order to cross from one minimum to another, a maximum of the potential energy surface has to be traversed. For a uni-molecular reaction of a reactant R being converted to product P

$$R \underset{k_-}{\overset{k_+}{\rightleftharpoons}} R^\ddagger \underset{k_-^\ddagger}{\overset{k^\ddagger}{\rightleftharpoons}} P \quad , \tag{2.168}$$

we can thus partition the reaction into a step where the reactant tries to reach the maximum on the PES ($R^\ddagger$) and a part where the transition state is converted into the product. Within transition state theory, it is assumed that any transition state particle $R^\ddagger$ that is successfully converted to product P, will not be able to return to its initial reactant minimum, i.e. $k_-^\ddagger = 0$. The equilibrium between the reactant species and the amount of molecules in the transition state is then described by the equilibrium constant $K^\ddagger$:

$$R \underset{k_-}{\overset{k_+}{\rightleftharpoons}} R^\ddagger \qquad \text{with} \quad K^\ddagger := \frac{k_+}{k_-} = \frac{q^\ddagger}{q} \quad , \tag{2.169}$$

where $q^\ddagger$ and q are the total partition functions of the transition state and reactant species, respectively. The assumption that any of the transition state species $R^\ddagger$ that crosses the highest point on the minimum energy pathway (MEP) along the reaction coordinate is irreversibly converted to products, leads to the general

transition state equation:

$$\mathrm{R} \underset{\mathrm{k}_-}{\overset{\mathrm{k}_+}{\rightleftharpoons}} \mathrm{R}^\ddagger \xrightarrow{\mathrm{k}^\ddagger} \mathrm{P} \qquad . \tag{2.170}$$

Here it is already implicit that the minimum energy pathway (MEP) from R to P is an elemental reaction step, i.e. there is one and only one maximum, namely the transition state $\mathrm{R}^\ddagger$, between these two minima on the PES. Hence, if we take the frequency ν of the vibration along this reaction coordinate as the frequency this crossing is attempted, we find

$$\frac{\mathrm{d[P]}}{\mathrm{d}t} = \nu[\mathrm{R}^\ddagger] = \nu K^\ddagger[\mathrm{R}] = \nu \frac{q'^\ddagger}{q}[\mathrm{R}] \qquad , \tag{2.171}$$

the dash on $q'^\ddagger$ indicating, that we have *included* the vibration along the reaction coordinate explicitly. Now writing this vibrational contribution q_ν separately, we find:

$$\frac{\mathrm{d[P]}}{\mathrm{d}t} = \nu q_\nu \frac{q^\ddagger}{q}[\mathrm{R}] = \nu \frac{\mathrm{e}^{-\frac{1}{2}\frac{h\nu}{\mathrm{k_B}T}}}{1-\mathrm{e}^{-\frac{h\nu}{\mathrm{k_B}T}}} \frac{q^\ddagger}{q}[\mathrm{R}] \qquad . \tag{2.172}$$

Since we are interested in Temperatures where $\mathrm{k_B}T \gg h\nu$, it is justified to use the classical expression for $q_\nu = \frac{\mathrm{k_B}T}{h\nu}$ and arrive at the transition state theory expression for the reaction rate:

$$\frac{\mathrm{d[P]}}{\mathrm{d}t} = \frac{\mathrm{k_B}T}{h}\frac{q^\ddagger}{q}[\mathrm{R}] = k_{\mathrm{TST}} \cdot [\mathrm{R}] \tag{2.173}$$

$$k_{\mathrm{TST}} \coloneqq \frac{\mathrm{k_B}T}{h}\frac{q^\ddagger}{q} = \frac{\mathrm{k_B}T}{h}\mathrm{K}^\ddagger \qquad . \tag{2.174}$$

Since usually we are interested in the thermodynamic form of this equation, we insert the relationship between the Gibb's free energy and the equilibrium constant $\Delta G^\ddagger = G(q^\ddagger, E^\ddagger_{elec}) - G(q, E_{elec}) = -\mathrm{k_B}T \ln K^\ddagger$ and find

$$k_{\mathrm{TST}} = \frac{\mathrm{k_B}T}{h} \cdot \mathrm{e}^{-\frac{\Delta G^\ddagger}{\mathrm{k_B}T}} \tag{2.175}$$

$$\overset{(2.160a)}{=} \frac{\mathrm{k_B}T}{h} \cdot \mathrm{e}^{\frac{\Delta S^\ddagger\left(\Delta q^\ddagger\right)}{\mathrm{k_B}}} \cdot \mathrm{e}^{-\frac{\Delta H^\ddagger\left(\Delta q^\ddagger, \Delta E^\ddagger_{elec}\right)}{\mathrm{k_B}T}} \qquad , \tag{2.176}$$

where $\Delta q^\ddagger$ and $\Delta E^\ddagger_{elec}$ imply, that the change in entropy is fully determined by vibrations, rotations and translations, while the change in enthalpy also depends on the change in electronic energy. ΔG also accounts for the missing electronic

term in the total partition function, since we do not assume any entropy in the electronic coordinates.

In order to describe surface phenomena, it is convenient to switch from concentrations to coverages. The coverage θ_{A_*} of any species A bound to a surface (indicated by the $*$) is given by

$$\theta_{A_*} = \frac{N_{A_*}}{M} \quad , \tag{2.177}$$

where N_{A_*} is the total number of species of type A on the surface and M is the total number of possible sites on the surface. Hence θ_{A_*} gives the fraction of surface sites occupied by A. Following from that, the rate is then given by

$$\frac{\mathrm{d}\theta_{A_*}}{\mathrm{d}t} = \frac{1}{M}\frac{\mathrm{d}N_{A_*}}{\mathrm{d}t} \equiv \frac{1}{M}\frac{\mathrm{d[P]}}{\mathrm{d}t} \quad . \tag{2.178}$$

2.7.3 Adsorption in the Context of Transition State Theory

The adsorption of molecules can be described in two main ways: Firstly, the incoming molecule is considered to only physisorb weakly to the surface, where it still has full vibrational and rotational freedom as in the gas phase, as well as a 2 dimensional freedom of translation, before it adsorbs to its final position on the surface. Here the transition state is the mobile, physisorbed species. In contrast to that, there is direct adsorption, in which the incoming molecule only finds one possible transition state close to its binding site, from which it only can desorb onto this site. The transition state species therefore only has vibrational freedom, but no rotations or translations, since it is now already considered to be *frozen* on the surface.

2.7.3.1 Precursor Mediated Adsorption

As mentioned before, the adsorption of a molecule A onto the surface can be described through a physisorbed species, i.e. a particle that is only bound very weakly to the surface and has full rotational, vibrational and two dimensional translational freedom over the surface, when still in this state:

$$^{3\mathrm{D}}\mathrm{A} + * \underset{\mathrm{k_-}}{\overset{\mathrm{k_+}}{\rightleftharpoons}} {}^{2\mathrm{D}}\mathrm{A}^{\ddagger} \xrightarrow{\mathrm{k}^{\ddagger}} \mathrm{A}_* \quad ,$$

where $*$ represents a binding site on the surface. Starting from eqs. (2.171) and (2.178), we find:

$$\frac{\mathrm{d}\theta_{A_*}}{\mathrm{d}t} = \frac{1}{M}\nu K^{\ddagger} N_A = \frac{1}{M}\ \nu\ K^{\ddagger}\frac{V p_{\mathrm{A}}}{\mathrm{k_B} T} \tag{2.179}$$

$$= \frac{1}{M}\ \nu\ \frac{V p_{\mathrm{A}}}{\mathrm{k_B} T}\ \frac{q'^{\ddagger}}{q} \qquad . \tag{2.180}$$

Now writing the vibration along the reaction coordinate q_ν and the other contributions seperatly we find

$$\frac{\mathrm{d}\theta_{A_*}}{\mathrm{d}t} = \frac{1}{M}\ \nu\ \frac{V p_{\mathrm{A}}}{\mathrm{k_B} T}\ q_\nu\ \frac{q^{\mathrm{2D}}_{trans}\cdot q^{\ddagger}_{rot}\cdot q^{\ddagger}_{vib}}{q^{\mathrm{3D}}_{trans}\cdot q_{rot}\cdot q_{vib}} \tag{2.181}$$

and using eqs. 2.164a, 2.164b and setting $q_\nu = \frac{\mathrm{k_B} T}{h\nu}$ yields

$$\frac{\mathrm{d}\theta_{A_*}}{\mathrm{d}t} = \frac{p_{\mathrm{A}}}{N_0\sqrt{2\pi\ m\ \mathrm{k_B} T}}\cdot\frac{q^{\ddagger}_{rot}\cdot q^{\ddagger}_{vib}}{q_{rot}\cdot q_{vib}} \qquad , \tag{2.182}$$

where $N_0 = \frac{M}{A}$ = available sites per area. Since we assume that rotations as well as vibrations do not change in this transition state, the second fraction in eq. (2.182) will always be equal to one. In realistic systems, there will always be a loss of rotational and vibrational freedom, therefore in reality it will always be somewhat smaller than 1. Using eq. (2.176) and the fact, that $\Delta q^{\ddagger} = 0$, we find:

$$\frac{\mathrm{d}\theta_{A_*}}{\mathrm{d}t} = \frac{p_{\mathrm{A}}}{N_0\sqrt{2\pi\ m\ \mathrm{k_B} T}}\cdot \mathrm{e}^{-\frac{\Delta H^{\ddagger}}{\mathrm{k_B} T}} \qquad , \tag{2.183}$$

where

$$\Delta H^{\ddagger} = H^{\ddagger} - H = \Delta U^{\ddagger}_{T=0\,\mathrm{K}} - \mathrm{k_B} T \qquad , \tag{2.184}$$

where we have used the fact that vibrations and rotations are the same for transition state and gas phase and all contributions from these then cancel exactly. It becomes obvious that the difference in electronic energy is the only decisive factor in this model. This result could, as a matter of principal, also be derived via collision theory, since we don't assume any changes in rotations or vibrations and essentially consider the molecule a hard sphere.

2.7.3.2 Intermediate Regime Adsorption

If the transition state of adsorption is located within a potential well that prevents translation, but permits rotation, we find

$$\frac{\mathrm{d}\theta_{A_*}}{\mathrm{d}t} = \frac{p_\mathrm{A}}{N_0\sqrt{2\pi\ m\ \mathrm{k_B}T}} \cdot \frac{q^\ddagger_{vib} \cdot q^\ddagger_{rot}}{q^\mathrm{2D}_{trans} \cdot q_{rot} \cdot q_{vib}} \cdot (1 - \theta_{A*}) \tag{2.185}$$

$$= \frac{p_{\mathrm{H_2}}}{N_0\sqrt{2\pi\ m\ \mathrm{k_B}T}} \cdot \mathrm{e}^{\Delta G^\dagger} \cdot (1 - \theta_{A*}) \qquad , \tag{2.186}$$

where

$$\Delta G^\ddagger = G(q^\ddagger_{vib}, q^\ddagger_{rot}, E^\ddagger_{elec}) - G(q^\mathrm{2D}_{trans}, q_{rot}, q_{vib}, E_{elec}) \qquad . \tag{2.187}$$

Obviously, this description is equivalent to an intermediate loss in entropy, compared to the precursor mediated and direct adsorption models and will result in rate constantss that will be in between the predictions of the other two models.

2.7.3.3 Direct Adsorption

For the case of direct adsorption, i.e. a transition state that has no more freedom of translation or rotation and is only able to vibrate, one has to account for the configurational entropy on the surface. The canonical partition function $Q^\ddagger$ of $N^\ddagger$ such transition state structures distributed over M' free sites is given by

$$Q^\ddagger = \frac{M'!}{N^\ddagger!\,(M'! - N^\ddagger!)} \left(q^\ddagger\right)^{N^\ddagger} \qquad , \tag{2.188}$$

from which, after some manipulations, it follows that the equilibrium constant is found as

$$K^\ddagger = M\,(\theta_* - \theta_{A^\ddagger})\,\frac{q^\ddagger}{q} \qquad . \tag{2.189}$$

From that, we find analogously to the direct adsorption case:

$$\begin{aligned}
\frac{\mathrm{d}\theta_{A_*}}{\mathrm{d}t} = \frac{1}{M}\nu K^{\ddagger} N_{\mathrm{A}} &= \frac{1}{M}\ \nu\ K^{\ddagger}\frac{V p_{\mathrm{A}}}{\mathrm{k_B}T} \\
&= (\theta_* - \theta_{A^{\ddagger}})\ \frac{V p_{\mathrm{A}}}{\mathrm{k_B}T}\ \nu\ \frac{q'^{\ddagger}}{q} \\
&= (\theta_* - \theta_{A^{\ddagger}})\ \frac{V p_{\mathrm{A}}}{h}\ \frac{q^{\ddagger}_{vib}}{q^{\mathrm{3D}}_{trans}\cdot q_{rot}\cdot q_{vib}} \qquad (2.190) \\
&= \frac{M\,(\theta_* - \theta_{A^{\ddagger}})}{N_0}\ \frac{p_{\mathrm{A}}}{\sqrt{2\pi\ m\ \mathrm{k_B}T}}\ \frac{q^{\ddagger}_{vib}}{q^{\mathrm{2D}}_{trans}\cdot q_{rot}\cdot q_{vib}} \\
&= \frac{p_{\mathrm{A}}}{N_0\sqrt{2\pi\ m\ \mathrm{k_B}T}}\cdot \mathrm{e}^{\Delta G^{\dagger}}\cdot(1-\theta_{A_*}) \qquad , \qquad (2.191)
\end{aligned}$$

where

$$\Delta G^{\ddagger} = G(q^{\ddagger}_{vib}, E^{\ddagger}_{elec}) - G(q^{\mathrm{2D}}_{trans}, q_{rot}, q_{vib}, E_{elec}) \qquad . \qquad (2.192)$$

Here we have absorbed M in the last step of eq. (2.191) into the translational partition function via $q_{trans,unitcell} = \frac{q_{trans}}{M}$ and we utilized that $(\theta_* - \theta_{A^{\ddagger}}) \approx \theta_* = 1 - \theta_{A_*}$, where $\theta_* = \frac{M'}{M}$ and M' is the Number of free sites. It becomes obvious that $\Delta G^{\ddagger}$ will have a strongly negative contribution from the gas phase, as there is a strong loss of entropy going from the gas phase to the frozen transition state. Consequently, the rate constantss will decrease in comparison to the precursor mediated adsorption model.

2.7.4 Reactions on Surfaces in the Context of Transition State Theory

Reactions on surfaces are in principle analogous to reactions in the gas phase, with the difference that there are no free translations or rotations of adsorbed species. We consider a bi-molecular reaction of the kind

$$\mathrm{A}_* + \mathrm{B}_* \rightleftharpoons (\mathrm{A\text{-}B})^{\ddagger}_{**} \longrightarrow \mathrm{AB}_* + * \qquad . \qquad (2.193)$$

Consequently, the partition function of both reactant and transition state species are solely comprised of vibrations. The rate then becomes

$$\frac{\mathrm{d}\theta_{\mathrm{AB}_*}}{\mathrm{d}\,t} = \nu\theta_{\mathrm{AB}^{\ddagger}_{**}} = \nu K^{\ddagger}\cdot\theta_{\mathrm{A}_*}\cdot\theta_{\mathrm{B}_*} \tag{2.194}$$

$$= \frac{\mathrm{k_B}T}{h}\frac{q^{\ddagger}_{vib}}{q_{vib}}\cdot\theta_{\mathrm{A}_*}\cdot\theta_{\mathrm{B}_*} \tag{2.195}$$

$$= \frac{\mathrm{k_B}T}{h}\cdot\mathrm{e}^{\Delta G^{\dagger}}\cdot\theta_{\mathrm{A}_*}\cdot\theta_{\mathrm{B}_*} \quad , \tag{2.196}$$

where

$$\Delta G^{\ddagger} = G(q^{\ddagger}_{vib}, E^{\ddagger}_{elec}) - G(q_{vib}, E_{elec}) \quad . \tag{2.197}$$

Note that $q_{vib} = q_{A_*,vib}\cdot q_{B_*,vib}$ represents the partition function of the two separated species. In periodic surface slab calculations, the separated partition functions will be replaced by the combined partition function, where A_* and B_* are in their pre-reaction adsorption spots.

The reverse reaction

$$\mathrm{AB}_* + * \rightleftharpoons (\mathrm{A\text{-}B})^{\ddagger}_{**} \longrightarrow \mathrm{A}_* + \mathrm{B}_* \quad . \tag{2.198}$$

is found straightforwardly from the same ideas.

2.7.5 Desorption in the Context of Transition State Theory

The desorption of molecules or atoms from surfaces is in principle the reverse of adsorption:

$$\mathrm{A}_* \rightleftharpoons \mathrm{A}^{\ddagger}_* \longrightarrow \mathrm{A} + * \quad . \tag{2.199}$$

Consequently, the transition state of desorption $\mathrm{A}^{\ddagger}_*$ may be able to translate and/or rotate over the surface, while it may also be confined to a certain desorption spot. We find the rate as

$$-\frac{\mathrm{d}\theta_{A_*}}{\mathrm{d}\,t} = \nu\theta_{A^{\ddagger}_*} = \nu K^{\ddagger}\theta_{A_*} \tag{2.200}$$

$$= \frac{\mathrm{k_B}T}{h}\frac{q^{\ddagger}}{q}\cdot\theta_{A_*} \quad , \tag{2.201}$$

where q and $q^{\ddagger}$ correspond to the partition function of the ground state and the transition state without the vibration along the reaction coordinate. Again the rate depends on the amount of translational and rotational entropy, that is gained or lost during the process of desorption. In our case, we assume that the transition state of desorption $A_*^{\ddagger}$, as well as the reactants, only possesses vibrational freedom. The rate can then be rewritten as

$$-\frac{\mathrm{d}\theta_{A_*}}{\mathrm{d}\ t} = \frac{\mathrm{k_B}T}{h}\frac{q_{vib}^{\ddagger}}{q_{vib}} \cdot \theta_{A_*} \tag{2.202}$$

$$= \frac{\mathrm{k_B}T}{h} \cdot \mathrm{e}^{\Delta G^{\dagger}} \cdot \theta_{A_*} \quad , \tag{2.203}$$

where

$$\Delta G^{\ddagger} = G(q_{vib}^{\ddagger}, E_{elec}^{\ddagger}) - G(q_{vib}, E_{elec}) \quad . \tag{2.204}$$

2.8 X-Ray Photoelectron Spectroscopy and First Principles

X-Ray photoelectron spectroscopy (XPS) is a routinely used tool to probe information about different atomic species in a sample. It exploits the fact that tightly bound core-level states do not participate actively in chemical bonding, but are very well influenced by the effective potential generated by the surrounding valence electron density, which in turn is strongly affected by local changes in geometry and composition. By exciting these core-level state electrons to the vacuum level and measuring their kinetic energy versus the energy of the incoming photons, one can then extract this information about local chemical environments of the atoms.

If the incoming photon of energy $h\nu$ strikes the sample which is previously in its ground state with energy E_0 and which emits an electron with kinetic energy KE_{e^-} that gets detected at a detector with an electric potential ϕ_D, so that the sample is then in the ground state of the first ionized Hamiltonian with final energy E_f^+, conservation of energy yields

$$E_0 + h\nu = E_f^+ + KE_{e^-} + e\,\phi_D \qquad . \tag{2.205}$$

This leads to accumulation of positive charge on the sample surface, which generates an additional attractive potential for the emitted electrons, which has to be taken into account when studying insulators or gas-phase species, while for metallic systems the sample is usually connected to a ground potential together with the detector, which compensates for any charge loss in the sample. The physical quantity of interest is the ionization binding energy of the electron BE, defined as the difference between the ionized and the ground state energy of the system

$$BE = E_f^+ - E_0 \qquad , \tag{2.206}$$

which can be obtained from eq. (2.205) as:

$$BE = h\nu - KE_{e^-} - e\phi_D \qquad . \tag{2.207}$$

Since the assignment of these measured binding energies to prevalent atomic species is not easy, it is desirable to have access to theoretically computed values to compare against. However, this prooves difficult due to the number of electronic

states that have to be considered when core-levels are explicitly included in the calculation of the wavefunction. The fact that core-levels are largely oblivious to changes in the valence density is usually exploited by describing them with a fictitious effective potential, which has the same electrostatic effect but circumvents the description of highly oscillating components of the wavefunction. Consequently, the computational description of core-level excited species for larger systems is difficult, since this requires either a core-ionized pseudo-potential or an all-electron calculation. Furthermore, in order to describe periodic systems, one has to either use an idealized infinitely repeating slab-approach – which cannot easily describe charged systems – or use a vacuum cluster, which has the same problems as molecular calculations.

These problems are partially circumvented by the fact that we are interested in relative changes of the binding energies $\Delta BE = BE_0 - BE$, where BE and BE_0 refer to the binding energy of two comparable species, which converge much faster than absolute energies due to error compensation. Furthermore, one can get an estimate of the binding energies by not using total energies as in eq. (2.205), but interpreting the eigenvalues of the Kohn-Sham orbitals as physical quantities in the context of Koopmans' theorem[102] (initial state approximation). However this still incorporates the problem of explicitly computing core-state eigenvalues. This is possible, using the so-called projector augmented wave-method, which implicitly constructs core-state pseudo-orbitals based on the valence-densities. Furthermore this method does not include any kind of relaxation contributions of the valence-density to the change in the core-state density, since it computes the core-states from the fixed valence-density. Nevertheless, for relative binding energy shifts, the resulting trends are generally of reasonable quality.[103]

3 Results and Discussion

3.1 Chemistry Under Confinement: The Water Formation Reaction on a Ru(0001) Surface Covered by a Silica Bilayer

3.1.1 Introduction

The interaction of solid materials with liquid and gaseous substances is of immeasurable importance in our world. As was mentioned in the introduction, it is assumed that the stabilizing interactions of small organic molecules with the surfaces of minerals and clays facilitated the emergence of the first amino acids and sugars, thus playing a vital role in the precursors to life.[11] In general, all living beings are compartmentalized into cells, which are themselves further sub-compartmentalized into cellular organelles and all forms of life as we know it depend on the existence of water, which emphasizes the crucial role of the interaction between the two. In addition, our daily life is full of examples that have direct impact, such as the "non-stick" coating of pots and pans, the subsequently occurring Maillard reaction giving fried foods their unique taste or the tarnishing of precious jewellery and metal workings. Of course, in many industrial processes, these interfaces also play a crucial role, requiring thorough investigation and characterization of the surface properties to obtain the best efficiency possible. As was touched upon before, the study of these systems faces unique challenges such as the small number of adsorbates on a surface or the complexity of realistic surfaces. In addition, most real / realistic systems are comprised of a large number of different constituents, some of which are crucial to the studied process and some of which are innocent bystanders. A common way of simplifying the real-world process and introducing a controllable amount of complexity is the use of model systems. For example, surface-science as such became only feasible with the advent of ultra-high vacuum (UHV) chambers

(as otherwise the surface would be covered with atmospheric components) and the ability to grow single-crystals with well defined surface orientations, which reduces the complexity of the system considerably.

The reason, why the interface between solid materials and liquids / gases is of crucial importance to many areas in chemistry is manifold. Firstly, solid materials are generally arranged into some sort of crystal, which can be envisioned as a giant macro-molecule interacting with the particles in the liquid or gas phase, thus the surface is the region in which the different types of chemical and physical materials interact. Secondly, the crystalline lattice of solid materials alters their electronic and physical properties expressing itself in the band-structure and properties such as electric conductivity and the phonon spectrum. The surface plays a special role, as atoms or molecules located in the topmost layers will have different and in general lower coordination numbers than atoms or molecules in the bulk. As a result, many crystal surfaces, as they would be obtained by simple cleavage of the bulk material along a crystal plane, are thermodynamically not stable and thus they often undergo reconstructive processes. For example, gold, platinum and iridium all reconstruct from the face-centered cubic bulk structure to form a hexagonal overlayer. A different example concerns the structure of frozen water, i.e. ice, where it was shown that the H_2O molecules in the topmost layer vibrate with a frequency four times as large, compared to bulk molecules. It could also be shown, that molecules in the top layer do not obey the crystalline structure below and in many ways they are responsible for the peculiar properties of ice, such as its slipperiness.[12]

Probably the most crucial reason for the reactivity of surfaces is the fact that they are *not* perfect surfaces of cleavage planes orthogonal to a crystal axis, but they are very much composed of plateaus of flat areas connected by grain-boundaries and steps and kinks between multiple crystal planes. It is exactly these "defect" sites of the perfect surface, where reactivity is strongly increased due to the altered coordination of surface atoms. This is nicely exemplified by the fact, that the probability of exchanging H_2/D_2 at these sites occurs on a stepped platinum surface near unity, while the reaction using a perfect (111) platinum surface was below the detection threshold.[104]

The property that a material, such as a crystal surface, can affect the progress of a chemical reaction is nowadays connected to the concept of catalysis. Initially, the term was coined in 1835 by the Swedish chemist Jöns Jacob Berzelius in an

annual report about the progress of chemistry,[105] however his understanding in terms of a "catalytic force" has been overhauled and today's definition is more closely formulated in the words of the German chemist Wilhelm Ostwald: "A catalyst is a substance that accelerates the rate of a chemical reaction without being part of its final products."[106]

In general, catalysis is grouped into homogeneous and heterogeneous catalysis, depending on whether the catalyzing agent is present in the same phase or in a different phase, respectively. The prime example for catalysis in nature are of course enzymes, which are biologically active substances that show an immense catalytic turnover number (TON).*

Due to the unique properties of surfaces outlined above, heterogeneous catalysis plays a vital role for many processes that render our modern world possible. Due to its importance in the production of fertilizer and the fact that during the research many fundamental aspects of catalysis were established, the Haber-Bosch process of converting hydrogen and nitrogen into ammonia is probably the best known example of heterogeneous catalysis. The catalyst that was developed for the first industrial-scale realization of the process was essentially iron with small amounts of potassium, aluminum and calcium added as promoters. These were and are still in use, but in recent years other catalysts based on ruthenium were proposed.[109,110]

The Haber-Bosch process is an excellent example for surface science as, due to its apparent simplicity of only involving two elemental gases $N_2 + 3\,H_2 \rightleftharpoons 2\,NH_3$, it lends itself well to model system studies. Model systems, in this case, are understood as well defined crystal surfaces that can be studied in UHV conditions and employing corresponding computational models to extrapolate the results to the real system. However, this also accentuates one of the problems in surface science, namely the so called "pressure-gap", referring to the fact that most studies are carried out under UHV conditions and low temperatures while realistic systems often operate under high pressures and temperatures, as well as the "material-gap", referring to the fact that realistic systems are rarely composed of well defined single crystal surfaces.

Other highly important examples of heterogeneous catalysis include the Fischer-Tropsch process, converting carbon monoxide and hydrogen at elevated tempera-

*In enzymology, the TON is defined as the maximum number of chemical conversions of reactants per second that a single active site will convert at a given concentration of enzyme.[107] In chemical catalysis, the TON is defined as the number of moles of substrate that one mole of catalyst can convert before becoming inactivated.[108]

tures and pressures and with the aid of metal catalysts such as iron and cobalt into liquid hydrocarbons, the Ostwald process for synthesizing nitric acid from oxygen and ammonia using platinum or copper catalysts, the Ziegler-Natta catalyst based on titanium compounds for the polymerization of alkenes or the desulfurization of petroleum using molybdenum and cobalt. The number and scale of these processes and the subsequent amount of research that has gone and still goes into them, underlines the importance of surface-science for our modern society.

As is evident, the understanding and tuning of these processes and the development of new catalysts is of monumental importance. One of the topics that has gained strong momentum in catalysis within recent years, is the idea of *chemistry under confinement*, that is the influence of spatially confining a reaction within another material.[111–117] Surfaces as such already provide a type of confinement by adsorbing species and thereby limiting their mobility and changing their properties. However, this concept is not limited to surfaces, as confinement can be achieved in a variety of ways. Not only are there a plethora of biologically important reactions strongly influenced by the available space,[118] such as reactions in small biological cells or at the interface between liquid and solid surfaces, for example in blood vessels or lung capillaries,[119–122] but also catalysis as such benefited a great deal from this concept.[123–126] The reason, why spatially confining a reaction is so attractive is, that one can directly attempt to design the interstitial space within the porous structure such, that only the desired reactants or products interact in a favorable way.

In order to spatially confine a reaction, it is necessary to provide a framework, which limits the available space, but yet allows for reactants and products to enter and leave the provided space. As a result, these systems are often termed host-guest chemistry, where the host is the framework that provides the sterical boundary conditions and the guest are all types of particles which are enclosed by the host. Of course, due to the fact that the host framework limits the available space, strong interactions between the guest molecules and the surrounding walls are inevitable. In general, the types of confined reactors are categorized into 1-D, 2-D, and 3-D compounds, which can be further sub-categorized (following IUPAC[127]) according to the pore diameters d into micro- ($\mathrm{d} < 2\,\mathrm{nm}$), meso- ($2\,\mathrm{nm} < d < 50\,\mathrm{nm}$), and macroporous materials ($d > 50\,\mathrm{nm}$).

A prime example is the interaction of molecules with metal-organic-frameworks (MOF). MOFs consist of metal ions or clusters, which are linked together by

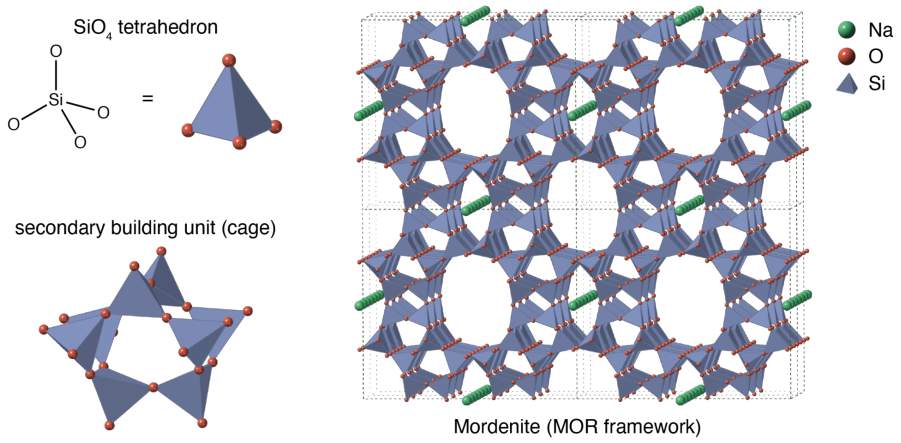

Figure 3.1: Microscopic structure of a zeolite (mordenite) framework, assembled from SiO_4 tetrahedra. Sodium is present as an extra-framework cation (in green).[128]

organic molecules to form 1-, 2- and 3-dimensional structures. Depending on the constituents, these compounds have pores of different sizes, defining a tunable space into which guest molecules may diffuse. A prominent example are the aluminosilicate minerals of the zeolite class, which consists of a network of SiO_4 tetrahedra with different counter ions positioned in the network. Examples of this class of structures are, amongst many other, analcime ($NaAlSi_2O_6 \cdot H_2O$), chabazite ($(Ca, K_2, Na_2)_2[Al_2Si_4O_{12}]_2 \cdot 12\,H_2O$) or stilbite ($NaCa_4(Si_{27}Al_9)O_{72} \cdot 28\,H_2O$). These materials feature pore sizes generally smaller than 1 nm and the basic building blocks of a typical zeolite material are shown in fig. 3.1.

This class of compounds is also often called “molecular sieves”, due to their wide variety of pore sizes and the ability of these structures to be used in gas purification processes, for example for the removal of H_2O or CO_2 from natural gas sources. Other applications include the use as solid state acids (due to the tunable presence of acidic protons in the structure), such as in fluid catalytic cracking and hydrocracking. However, due to their chemical and physical properties, these substances find wide use in areas from water purification and softening for domestic and commercial use, to solar cell technologies or soil treatment for agriculture.[115,129]

In more recent years, 2-D confined systems have seen a surge in interest, motivated by the success of monolayer graphene and the subsequent progress in growing other ultra-thin films of other materials such as hexagonal boron nitride (h-BN), transition metal dichalcogenides and crystalline and vitreous (amorphous) SiO_2

over metal supports.[114,115] These materials are of interest, because they define a tunable space between the atoms of the layer and the metal substrate into which molecules can be intercalated. The ultra-thin films of silica have attracted special attention, due to the fact that they can be both grown as a mono-atomic layer, chemically attached to the metal surface via bridging Si – O – Ru bonds, as well as a bilayer that is chemically detached from the surface and only bound via dispersive van-der-Waals forces. In addition, these layers can be synthesized (coexisting on the same surface) both as a crystalline network, consisting of purely of six-membered rings formed by the SiO_4 tetrahedra (except for grain boundaries and defects) and an amorphous network consisting of a distribution of randomly-sized rings with no apparent periodic structure.[130–132] These model-systems can thus be used as an example to study the transition from vitreous to crystalline phases, a topic that is still heavily debated.[133]

The mechanisms, by which spatial confinement and the host-guest interactions alters certain chemical reaction pathways, have been under intense research. Grommet et al.[11] pointed out, that even though there are a large variety of different systems for confining chemical reactions, the effects of the confinement are often very similar. Within their review, they recognized five different effects, that are responsible for most properties of the confined system:

- Acceleration of chemical reactions:

  Due to the sterical and electronical constraints provided by the host, it is possible to pre-organize molecules and increase their local concentration within the confined space, thus translating into an acceleration of the reaction. In addition, the host can stabilize transition states of the reaction, thus increasing the speed.

- Enhancement of alteration of selectivity:

  The walls of the host will inevitably introduce a limit for the maximum size of reactants, transition states and products thus possibly rendering certain reaction pathways impossible or unlikely, introducing a bias towards certain molecules. Additionally, the geometry of the host may favor certain molecules over others, resulting in a “selection” of pre-organized molecules, transition states or products.

- Stabilization of reactive species or unstable assemblies:

  It was shown that confinement can drastically increase the stability of certain intermediates, for example in the electro-chemical cycle of batteries, thus increasing their lifetime. Additionally, un- or meta-stable molecules can be stabilized by favorable interactions with the cavities. For example, it is possible to synthesize single DNA base-pairs within a coordination cage, which are unstable in solution.

- Modulation of light absorption and emission:

  The effect of confinement was observed to have two different results on photo-active molecules. Firstly, they can act as a "protective-coating", that is they can prevent molecules from undergoing reactions by hermetically sealing them from their environment. Additionally, by pre-organizing molecules in close vicinity to each other as well as in periodic arrangements, the host may induce changes in the electronic and physical properties of guest molecules by changing weak interactions, for example π-π stacking and van-der-Waals forces.

- Modulation of electrochemical properties:

  Confining molecules can also have an effect on their electrochemical properties without changing their chemical structure. For example, the electric fields of polar molecules can interact when brought close together, inducing changes in the redox potential or there may occur charge-transfer between the host and the guest molecules. Additionally, the long-range structure of the host can induce periodicity in the guest molecules, potentially leading to electric conductivity.

While it is well known that ruthenium catalyzes the water-formation-reaction (WFR) from dissociativley adsorbed hydrogen and oxygen,[134] it was recently discovered using low energy electron microscopy, that the reaction proceeds in a wave-like fashion across a Ru(0001) surface and that confining the adsorbed species by depositing a silica-bilayer over the surface has a strong impact on the front velocity as well as the observed apparent reaction barrier.[130] Figure 3.2 shows a series of low energy electron microscopy (LEEM) snapshots taken during the experiment, where a moving reaction front can clearly be identified.

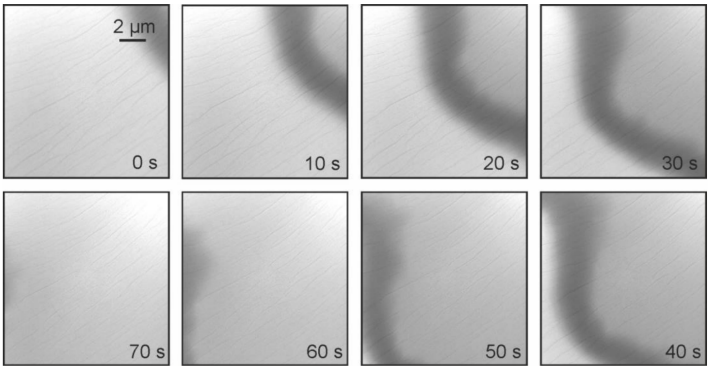

Figure 3.2: LEEM snapshots for the water-formation-reaction on a Ru(0001) surface. The bright area of the surface corresponds to the oxygen rich parts. Reproduced with permission from the authors.[135]

Previous studies identified the formation of hydroxyl (OH) groups from atomically adsorbed oxygen and hydrogen as the rate-determining step (RDS) for the WFR on ruthenium, while all subsequent steps are considerably faster. In particular the desorption of water on a bare surface is very fast at the experimentally considered temperatures (400 K – 675 K).[134–136] Using X-ray photoelectron spectroscopy (XPS) and LEEM techniques, the authors demonstrated that the reaction front propagates from an area of low oxygen concentration (0.25 ML) towards areas of high oxygen concentration. Together with the fact, that there are only four possible adsorption spots per unit cell on the ruthenium surface and that it is covered with a 0.75 mono-layer (ML) of oxygen prior to the introduction of H_2, the authors concluded that the reaction must have its origin in a defect of the oxygen ML, since otherwise there are not enough adsorption sites available for the dissociative adsorption of hydrogen.

While, for the confined system, the same reaction was observed at lower front velocities, the same XPS pattern was observed before and after the reaction, concluding that the silica bilayer is not deteriorated during the reaction and the effect must be sought elsewhere. Figure 3.3 summarizes the changes of the XPS spectra before and after the reaction. It is evident that the oxygen concentration diminishes (the shoulder in the pre-reacted XPS spectrum) and that there is a consequential shift of the peak due to the removal of the surface dipole induced by adsorbed oxygen atoms.

While the chemical denaturation of the silica film could be excluded, it could not be shown, whether the observed effect of the confinement is due to the transition

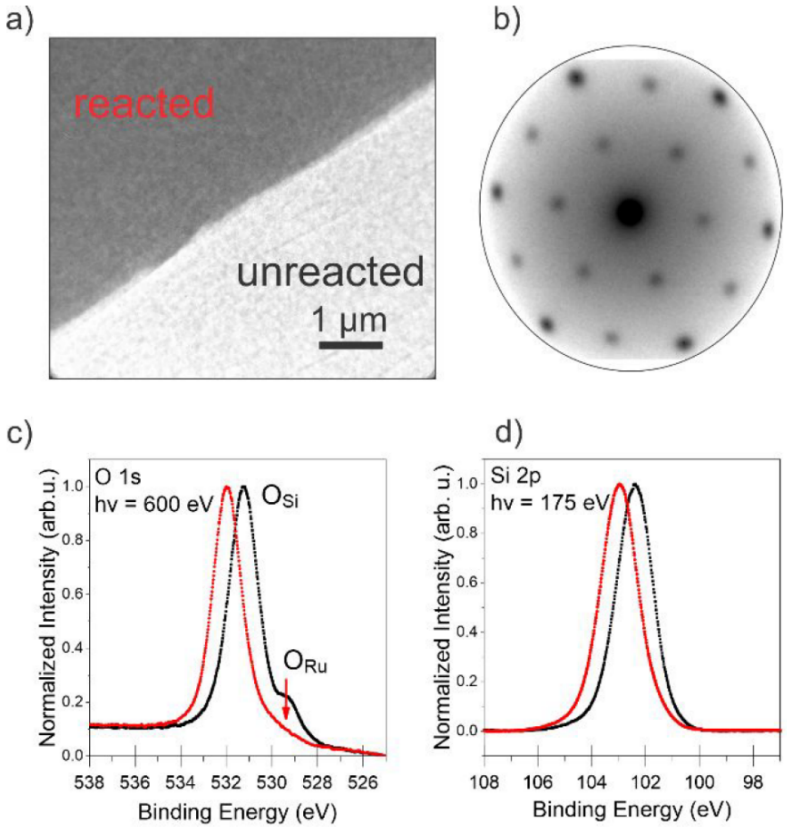

Figure 3.3: (a) LEEM snapshot showing the reaction front under reaction conditions; the O-rich and O-poor areas are labeled as unreacted (black) and reacted (red), respectively. (b) LEED pattern showing the characteristic (2×2) spots of the SiO_2 BL on Ru(0001) measured on the reacted sample. The patterns of the reacted and unreacted surface do not differ regarding number, position and broadening of the spots. (c, d) Local O 1s and Si 2p photoemission spectra collected on both sides of the reaction front. Reproduced with permission from the authors.[135]

state effect, that is if the reaction mechanism itself changes, or whether it is due to the effect of the confinement on the diffusion of both surface species and adsorption / desorption of hydrogen and water, respectively.

Since this system can be prepared under controlled conditions in a variety of ways, it lends itself as a prime candidate for a model system to study the processes involved from both an experimental and a theoretical point of view. In this section, we thus aim for the comprehensive study of the mechanism behind the water-formation-reaction on a ruthenium (0001) surface, both on a bare surface and under silica bilayer confinement. To do so, we leverage the power of quantum mechanical modeling using periodic DFT methods to obtain a comprehensive picture at the microscopic level of the processes at hand, which together with experimental data and mathematical modeling, results in a full picture of the system under consideration.

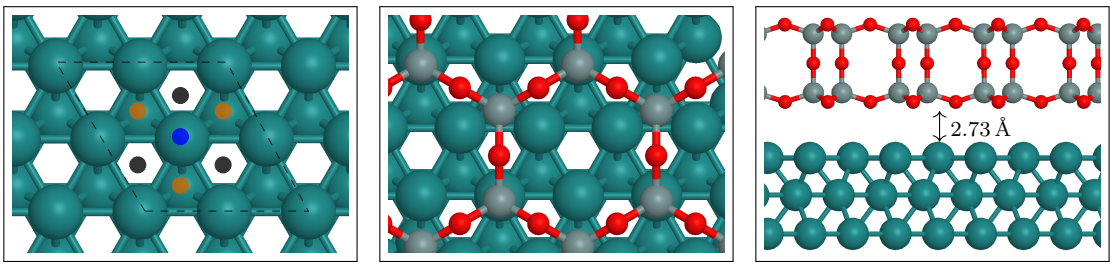

Figure 3.4: Left: On-top view of the ruthenium (0001) surface. Colored dots indicate binding sites: "on-top" (blue), "hcp" (orange) and "fcc" (black). The (2×2) unit cell is indicated with dashed lines.
Middle and right: Top and side view of a Ru surface with a SiO_2 bilayer.
Ruthenium, silicon and oxygen atoms are shown in green, gray and red, respectively.

3.1.2 Atomistic Model for Surface and Bilayer Geometries

Our goal is to investigate the atomistic process involved in the WFR occurring on a partially oxidized ruthenium (0001) surface, both on a bare surface and when confined under a two-dimensional silica-bilayer sheet.

In order to characterize the surface from a theoretical point of view, we set up a corresponding surface model, obtained from an optimized primitive hexagonal close-packed ruthenium bulk cell with two ruthenium atoms per cell,[137] from which a repeated 3-layer slab with a (0001) surface direction and a vacuum layer of 30 Å was constructed. The optimized and experimental bulk lattice constants are given in table 3.1.

If not stated otherwise, the (2×2) surface super-cell was used in our calculations. The top ruthenium layer was allowed to relax while the bottom two were fixed at their bulk positions. To model the confined case, a crystalline SiO_2-bilayer was added to the surface. A representation of the surface slab with and without a bilayer on top is shown in fig. 3.4.

	a / a_0	c / a
Theoretical	5.1337	1.56
Experimental	5.1132	1.58

Table 3.1: Experimental[138] and calculated ruthenium bulk unit cell parameters for a primitive hexagonal, closed packed structure with 2 atoms per cell.

Since it is difficult to predict the position of the SiO_2 rings with respect to the surface and oxygen atoms in real experiments, as irregularities in the bilayer

and/or surface may lead to a shift of these rings relative their optimal position on an ideal surface. In order to cope with this problem, we modeled two distinct (extreme) cases: a constrained and an optimized bilayer. In the constrained bilayer case, the x- and y-coordinates of the bilayer were chosen to coincide with those of its optimal position on a (2×2)-3O (0.75 ML) surface, corresponding to the in situ preparation conditions of the bilayer.[139] With the position of the bilayer fixed, the coverage was reduced to a (2×2)-2O to model the reaction (this coverage is expected in the active reaction region of the reaction front), and to a (2×2)-1O surface, in order to model the hydrogen adsorption. Within the experimental setup, removal of the last oxygen atom per unit cell requires temperatures well above those considered ($> 970\,\mathrm{K}$).[134]

In the optimized bilayer case, after the same manipulations were applied, the bilayer was allowed to find its optimal position on the surface (with the initial position also being taken from the (2×2)-3O surface) and was additionally allowed to fully relax at each step along the adsorption and reaction paths.

3.1.3 Employed Computational Methods

In order to access the potential energy surface (PES) of the system under study at a reliable level of theory, we employed density functional theory, as originally developed by Kohn and Sham[71] and implemented in the Vienna Ab Initio Simulation Package (VASP)[140] and the Quantum Espresso (QE) suit of codes.[141] In addition, the frozen-core approximation was invoked by using scalar-relativistic, ultra-soft pseudopotentials (QE) or the projector-augmented wave method (VASP). The exchange and correlation potential was described using the generalized gradient approximation proposed by Perdew, Burke and Enzerhof[78] with an additional atom-pair based dispersion-correction D2 proposed by Grimme et al.[89] Integration of the first Brillouin zone was done using a weighted uniform $\vec{k}$-point grid ($6 \times 6 \times 1$ for a (2×2) cell) as proposed by Monkhorst and Pack.[142] Plane waves up to $E_{PW} = 400\,\text{eV}$ were included in the expansion of the wavefunction. A Gaussian-type spreading for the Brillouin zone integration of metals with a width of 0.15 eV was utilized. Minima on the PES were optimized until all components of all forces were less than $5 \times 10^{-3}\,\frac{\text{eV}}{\text{Å}}$ and the change in electronic energy between two optimization steps was less than $1 \times 10^{-4}\,\text{eV}$.

Transition states were searched using the nudged elastic band (NEB) method[143] between two points of interest on the PES until the error on the projected forces was less than $0.05\,\frac{\text{eV}}{\text{Å}}$ and further refined with the improved dimer-method.[144]

Vibrational modes were then accessed using a central finite-differences scheme within the harmonic approximation. In calculations involving weakly interacting species, some of the harmonic vibrational frequencies turned out to be very close to zero, unphysically blowing up the entropic contribution, or even imaginary, leading to inconsistencies in the entropy along the reaction path. In our calculations this problem occurred for the vibrations originating from the rotations of the hydrogen molecule in the adsorption transition states, corresponding to its penetration through the bilayer (vide infra). In these calculations we did not include these vibrations in the partition function (2.167), but added the rotational partition function instead. Besides, to obtain balanced entropic contributions in the constrained and optimized calculations, in the latter case the vibrations of the bilayer in the x- and y-directions were not included in the vibrational partition function (2.167) at any reaction step. Firstly, these vibrations are essentially anharmonic and of very low frequency, so within the harmonic approximation their contribution to the entropy would be substantial, but very inaccurate. Meanwhile,

in the constrained case, these vibrations are entirely absent, as in this case the bilayer is not allowed to move in the x- or y-direction.

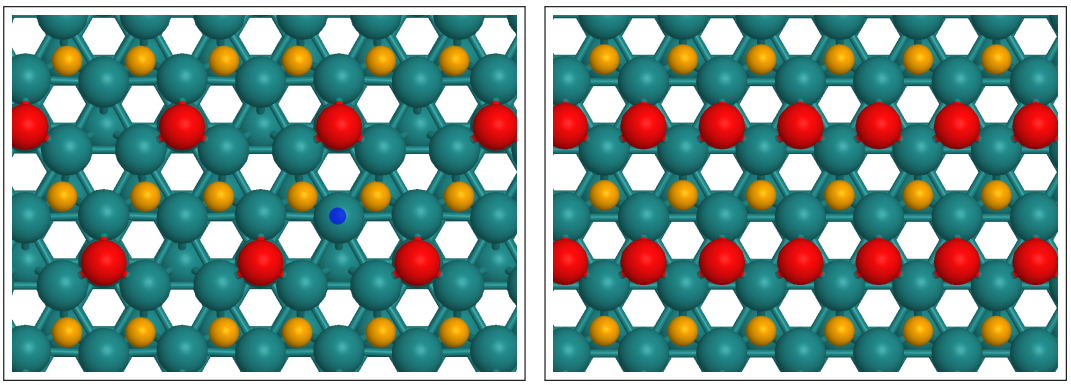

Figure 3.5: (2×2)-1O (left) and (2×2)-2O (right) surfaces with two hydrogen atoms (orange) adsorbed per unit cell. Hydrogen is forced to occupy hcp hollow sites in order to maximize its distance to adjacent oxygen (red) atoms. For the (2×2)-1O surface, there is one additional on-top binding site available surrounded by 3 oxygen atoms (indicated by a blue dot).

3.1.4 Investigation of the Potential Energy Surface

3.1.4.1 Adsorption of H_2 on a Partially Oxidized Ru(0001) Surface

Since, experimentally, the ruthenium surface is already partially covered with atomically bound oxygen resulting from the preparation of the bilayer, the first step in the process is inevitably the adsorption of hydrogen onto the surface. Due to the repulsive interactions between the adsorbates, both species are known to form ordered adlayers on the surface at low enough temperatures.[145] As reported in the literature, oxygen prefers hcp-hollow binding-positions, while hydrogen will bind to fcc-hollow sites.[146,147] However, when oxygen atoms are present, the actual position of hydrogen atoms is determined by a balance between the attraction to the surface and strong repulsion at a short distance between oxygen and hydrogen. As a consequence, on-top binding sites also become available for hydrogen when it is symmetrically surrounded by repelling oxygen atoms and therefore maximizes the distance to these atoms. Furthermore, since oxygen binds to hcp-hollow sites, all adjacent fcc-hollow sites become unavailable, forcing hydrogen to either bind to hcp-hollow or on-top sites (fig. 3.5).

In general, the adsorption process of hydrogen onto a ruthenium surface is determined by two subsequent steps: Firstly, the incoming molecule chemisorbs to the surface as a whole, before, as the second step, it dissociates into two hydrogen atoms. The dissociation happens step wise (e.g. one hydrogen atom remains on

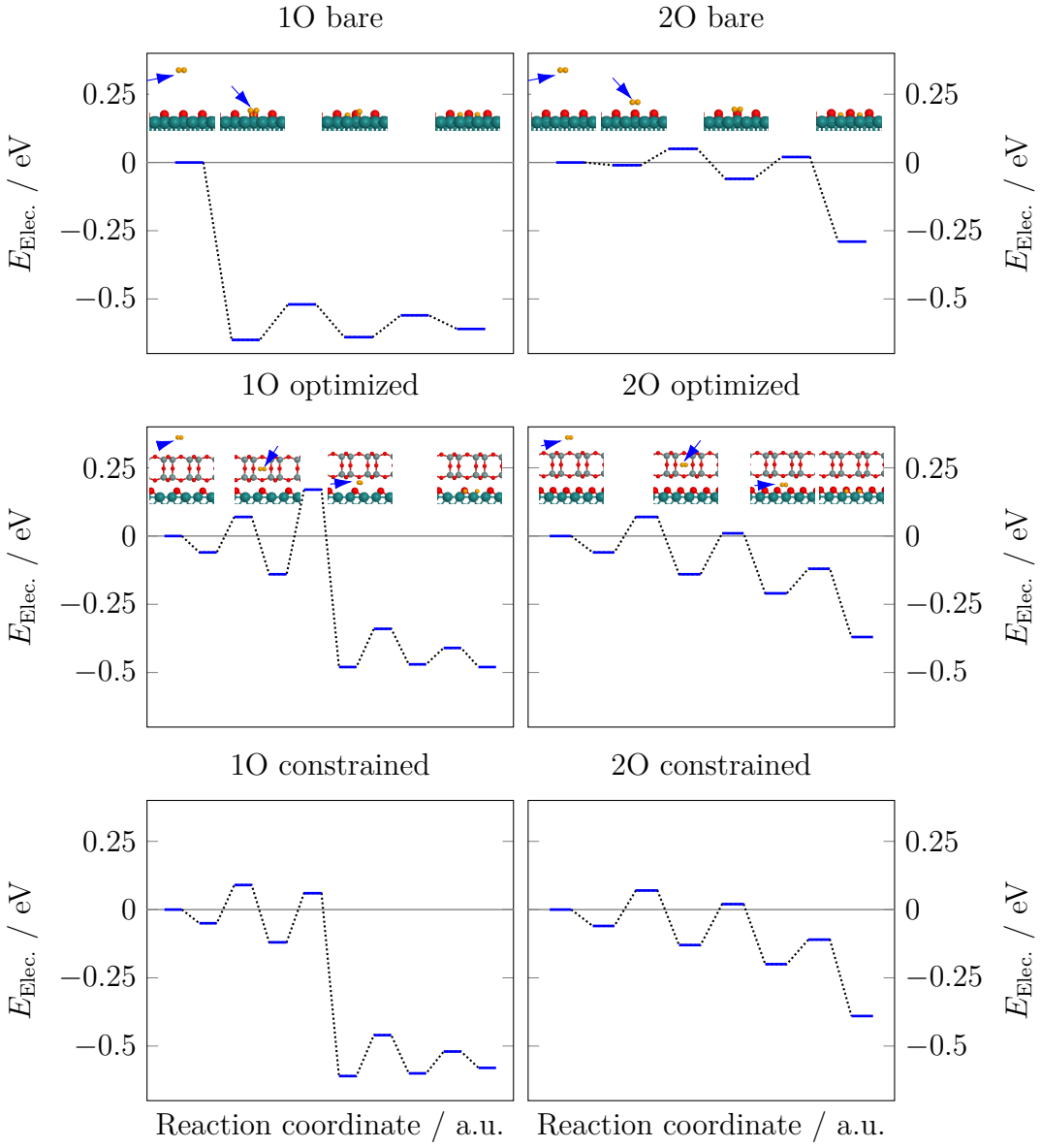

Figure 3.6: Comparison of the different electronic minimum energy pathways for the dissociative adsorption of hydrogen onto a partially oxidized Ru(0001) surface with different oxygen coverages. The position of the hydrogen molecule prior to adsorption is indicated with a blue arrow. The pictures for the constrained case have been omitted for clarity.

the on-top site while the other is moving to the hcp adsorption site). Since oxygen atoms introduce repulsive interactions between the adsorbates, an increased oxygen coverage also impedes adsorption of hydrogen, as the necessary on-top sites for splitting are getting too close to oxygen atoms.

As is seen from the calculated minimum energy pathways (MEP) (fig. 3.6 top), the electronic part of the hydrogen adsorption onto a bare surface with low oxygen concentration is barrierless and the gain in potential energy due to adsorption outweighs the cost of splitting the hydrogen molecule. When increasing the oxygen coverage on the surface, some of the on-top sites required for splitting H_2 are in close vicinity to an oxygen atom, resulting in a slightly activated process. For coverages higher than 0.75 ML (3 oxygens per (2×2) unit cell), adsorption becomes essentially impossible since there are not enough free binding sites neighboring each other.

The addition of a van-der-Waals-bound SiO_2 bilayer over the surface converts these adsorption processes into clearly activated processes, irrespective of the oxygen concentration on the surface. The penetration through the lower silica ring becomes the decisive energy barrier. It is strongly influenced by the nearby oxygens on the surface, as well as by the position of the bilayer relative to the required on-top site for splitting.

The different resulting adsorption processes for both systems are shown in fig. 3.6 (middle and bottom). One can note a higher barrier and a less negative adsorption energy in the optimized bilayer 1O case compared to the constrained one. This can be attributed to an additional movement of the bilayer in the optimized case needed for the incoming H_2 molecule to reach an on-top site, while in the constrained case, the bilayer is from the onset positioned in such a way, that the on-top site for H_2 is readily available. This effect is virtually absent in the 2O case, as the positions of the constrained and optimized bilayer are similar and all on-top sites are inconveniently located not far from an oxygen atom.

3.1.4.2 Formation of Water from Atomically Adsorbed Hydrogen and Oxygen

As was demonstrated in the last section, the addition of a silica bilayer over the ruthenium surface considerably changes the potential energy landscape for incoming hydrogen molecules, by introducing two new transition states, one for the passage of each layer of the silica sheet. In a second step, we will now consider three

elemental reaction channels on the surface that may contribute to the formation of water:

$$\mathrm{O}_* + \mathrm{H}_* \rightleftharpoons \mathrm{OH}_* \tag{3.1}$$

$$\mathrm{OH}_* + \mathrm{H}_* \rightleftharpoons \mathrm{H_2O}_* \tag{3.2}$$

$$2\,\mathrm{OH}_* \rightleftharpoons \mathrm{H_2O}_* + \mathrm{O}_* \quad , \tag{3.3}$$

of which the last one is in competition with the second but will only take effect when there is a considerable amount of OH or H_2O present on the surface. Consequently, a necessary intermediate step in the water-formation-reaction is the presence of hydroxyl (OH) groups on the surface, and since their concentration has direct influence on the overall reaction speed, special attention has to be given regarding their properties.

Figure 3.7 shows the obtained MEPs for the six different systems of interest for the first two reactions discussed above. The first barrier, corresponding to the formation of OH from atomically adsorbed O and H, features a large electronic barrier that is mostly independent of the chemical environment. This can be explained by the relatively large size of the SiO_2-bilayer rings, enclosing multiple reaction sites such, that there will be at least one mostly undisturbed site available for the reaction. Additionally, neither atomically bound hydrogen nor oxygen show considerable interaction with the bilayer due to their small size and absence of hydrogen-bridge bonding interactions.

In contrast to this first reaction channel, the formation of water from OH and H is energetically much more favorable on a bare 2O surface or one equipped with an optimized silica bilayer. The reason for the lowered activation energy and increased stability of water species on a 2O surface over a 1O surface can be explained by an interplay of stabilizing hydrogen bonding with higher oxygen coverage and a destabilizing influence from the mutual repulsive interactions between adsorbates: Since oxygen atoms destabilize surface binding of surrounding oxygen and hydrogen atoms, a higher oxygen concentration translates to an increased energy gain when the number of neighboring surface species is decreased, e.g. when OH or H_2O is formed. Additional energy is gained when the number of hydrogen bonding interactions is increased as a result of the reaction. These two features manifest themselves in a greater energy gain going from atomic O and H to H_2O for a 2O surface than a 1O surface, since on a 1O surface, there is no oxygen left

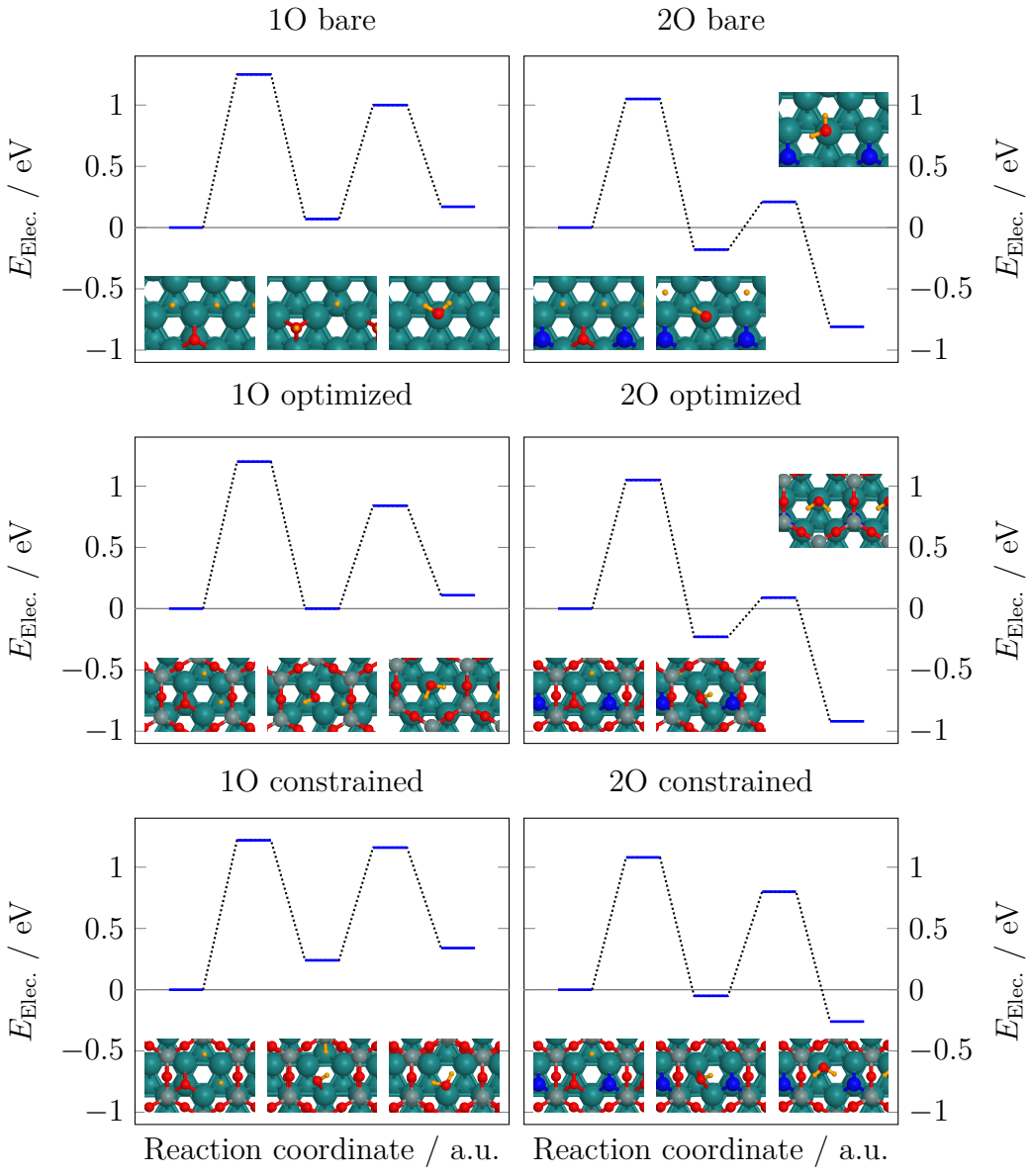

Figure 3.7: Comparison of the different electronic minimum energy pathways for the reaction cascade $2\,H_* + O_* \rightleftharpoons H_* + OH_* \rightleftharpoons H_2O_*$. The first step is virtually independent of its chemical surroundings while the formation of water becomes strongly dependent to the presence of free ontop binding sites. Adsorbed oxygen atoms that are not participating in the reaction are colored in blue.

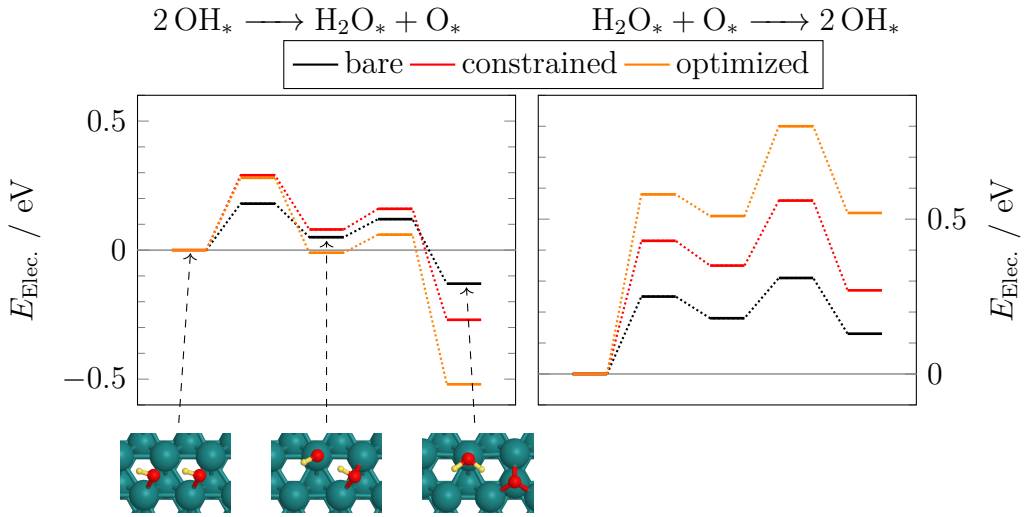

Figure 3.8: Comparison of the different electronic minimum energy pathways for the dispropotionation reaction $2\,OH_* \longrightarrow H_2O_* + O_*$ (left) and the reverse comproportionation reaction $H_2O_* + O_* \longrightarrow 2\,OH_*$ (right).

after the reaction, while one a 2O surface, one O remains, enabling the OH and H_2O molecules to interact via hydrogen bonding. Furthermore, the reduced energy barrier for the second reaction step on a 2O surface is explained by the "uncomfortable" hydrogen atoms, whose proximity to neighboring oxygen atoms raises their potential energy to almost match the transition state energy.

However, this effect is not observed for the constrained bilayer 2O system, since the formation of water from OH and H requires an on-top surface spot as active site for the transition state *and* the binding of the resulting water molecule, which is not available for the bilayer position chosen without moving it over the surface. Thus both the transition state and the resulting water get destabilized in their binding. From this it may be deduced that at a certain water concentration on the surface, the energy gain from water being able to access free on-top sites may outweigh the cost of shifting the bilayer and different reaction channels may be dominant at different concentrations.

The electronic MEP for the formation for water from two OH groups (eq. (3.3)) is shown in fig. 3.8 (left). We split the reaction up into a "diffusion" step and a reaction step, since the lowest energy configuration of two OH groups is separated by one higher minimum on the PES and at temperatures above $T = 0\,K$, according to our calculations the second maximum and therefore the intermediate minimum vanishes. It can be seen that the electronic barriers are small compared to the

formation of OH groups and consist mainly of bringing two hydroxyl groups close together. Consequently this reaction channel will increase the rate of water formation, but only when there is enough OH on the surface, so as to bring them close enough together before another reaction channel is preferred.

On the other hand, the reverse comproportionation is strongly dependent on the presence of a bilayer and whether it is constrained in its movement or not, being explained by the same reasoning of the requirement of an on-top site for water to bind to, which is only easily accessible in the unconstrained case.

3.1.4.3 Desorption of Water from the Surface

At higher concentrations, H_2O molecules form intricate hydrogen-bonding networks which are accompanied by partial dissociation of water molecules resulting in an increase in desorption energy.[148] However, at low concentrations, these networks are not possible and the average residence time of water on the surface is expected to decrease. Figure 3.9 shows the MEPs for the 6 different systems of interest. The desorption energies for a single water molecule from a bare surface with a concentration of 1O and 2O per (2×2) unit cell are 0.67 eV and 0.91 eV, respectively. The increase in the desorption energy is explained by the additional H-bonding that is possible with one O remaining on a 2O surface. As for the adsorption of hydrogen, the additional confinement introduces two additional transition states, one for passing each layer. In contrast to the adsorption of H_2, the transition state with the greatest total energy is the upper ring of the bilayer. Furthermore it can be seen that a fixed bilayer already includes the increase in potential energy of the water molecule bound to the surface discussed before, which effectively lowers the barrier of desorption as compared to a free moving bilayer or unconfined surface.

3.1.4.4 Diffusion on the Surface

The diffusion on the surface is integral to the description of the system at hand, since the change in diffusivity can have drastic effect on the overall reaction speed. Unfortunately there is a vast number of possible diffusion channels on the surface for each species. In order to obtain a first characterization of the possible mechanisms, we consider selected trajectories on the surface for hydrogen atoms, OH and water molecules. In a first step, we are considering the diffusion of hydrogen on a bare 1O surface traversing one unit cell. A representation of the diffusion path and the corresponding electronic energy diagram is shown in fig. 3.10 on the left.

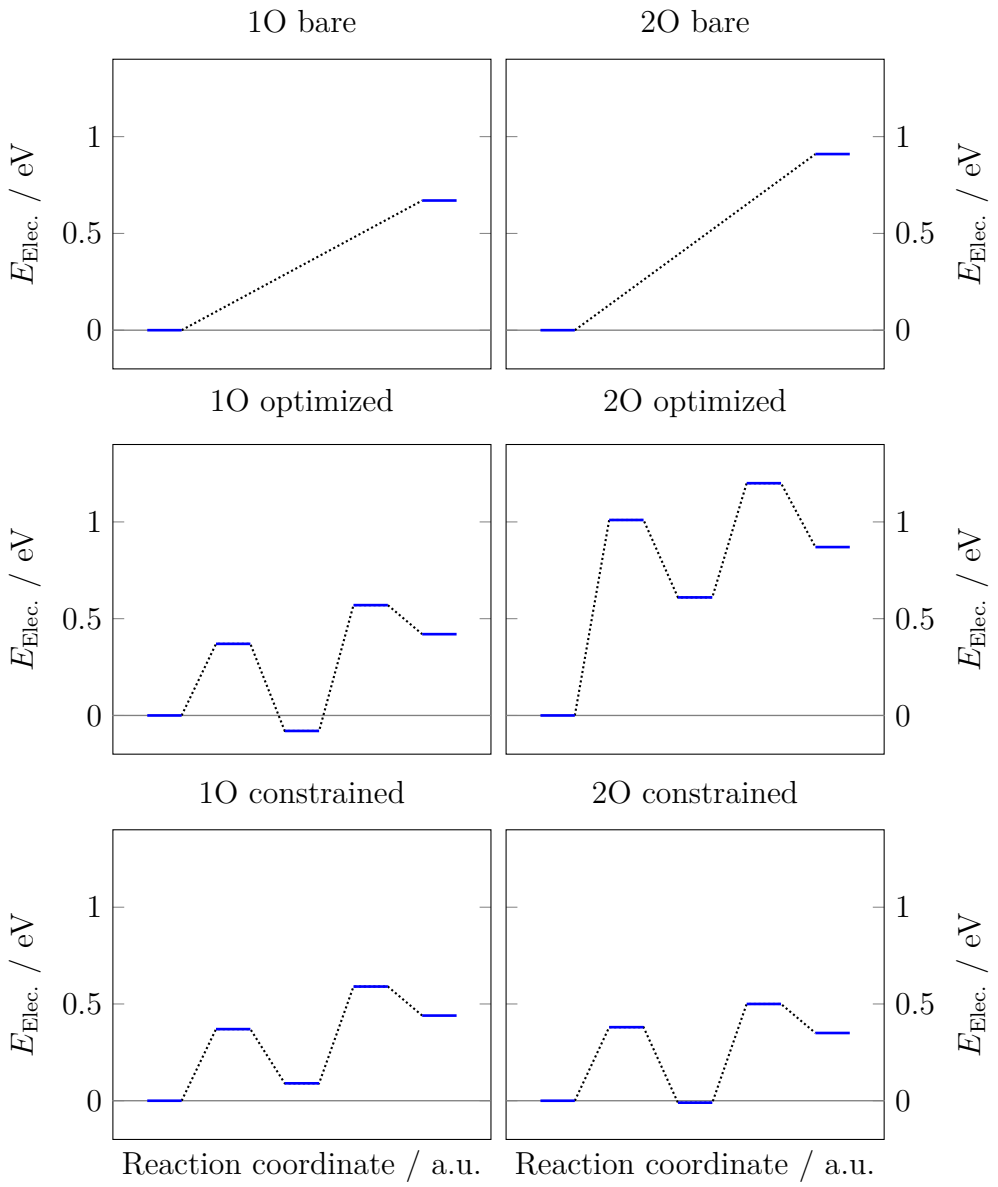

Figure 3.9: Comparison of the different electronic minimum energy pathways for desorption of H_2O from a Ru(0001) surface with various concentrations of oxygen. The bilayer introduces two new transition states, one for passing eacher layer.

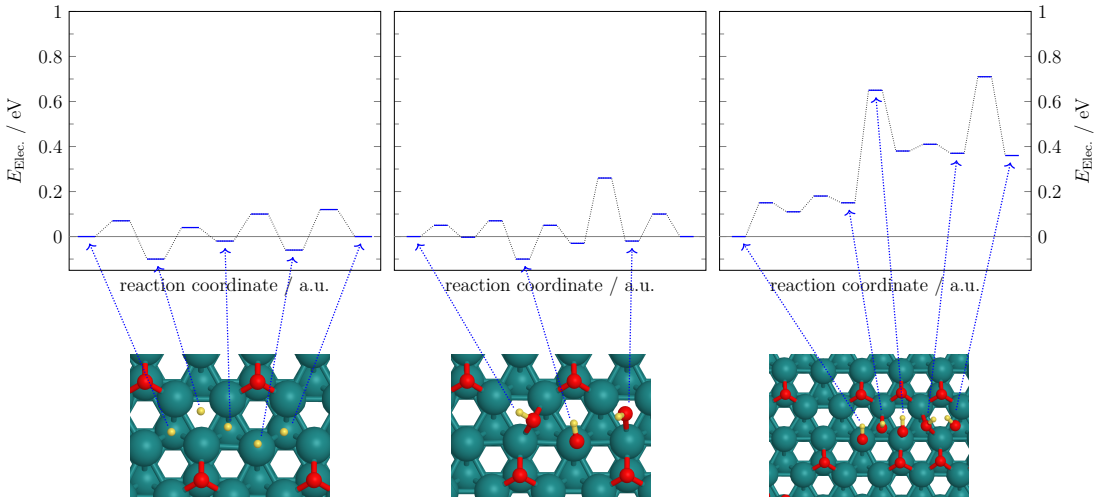

Figure 3.10: Middle and left: MEPs for the diffusion of atomic hydrogen (left) and OH groups (middle) on a bare 1O Ruthenium surface. The path completes one (2×2) unit cell and wraps around itself.
Right: MEP for the diffusion of OH groups across a 1O–2O domain boundary.

It is apparent, that with barriers between 0.1 and 0.2 eV, hydrogen is able to diffuse at sufficiently long distances at our experimental temperatures. Hydrogen shows little interaction with the surrounding oxygen atoms, as well as the bilayer and therefore may adsorb at relatively distant parts of the reaction front and diffuse over the surface to reach it in both the confined an unconfined case.

In a next step, we are investigating the diffusion of OH groups on a bare 1O surface, as well as across the 1O – 2O domain boundary. The corresponding paths and MEPs are shown in fig. 3.10 (middle and right). Barrier heights for the diffusion on a 1O surface are slightly increased (~ 0.4 eV) in comparison with hydrogen diffusion due to the additional H-bonding interactions with the surface oxygen atom. The barrier grows notably (~ 0.6 eV) when OH is diffusing across the 1O – 2O domain boundary. Since, especially in the vicinity of the reaction front, heterogeneity in the distribution of the oxygen concentration is expected, the diffusion of OH groups will still be hindered by the oxygen concentration boundaries. In addition, effective OH diffusion via hopping of hydrogen atoms from oxygen atom to oxygen atom on a 2O surface was investigated, but rendered much higher diffusion barriers (~ 0.8 eV).

Lastly, we are investigating the diffusion of water on a bare 1O surface, as well as one equipped with a silica bilayer. The considered MEPs are shown in fig. 3.11.

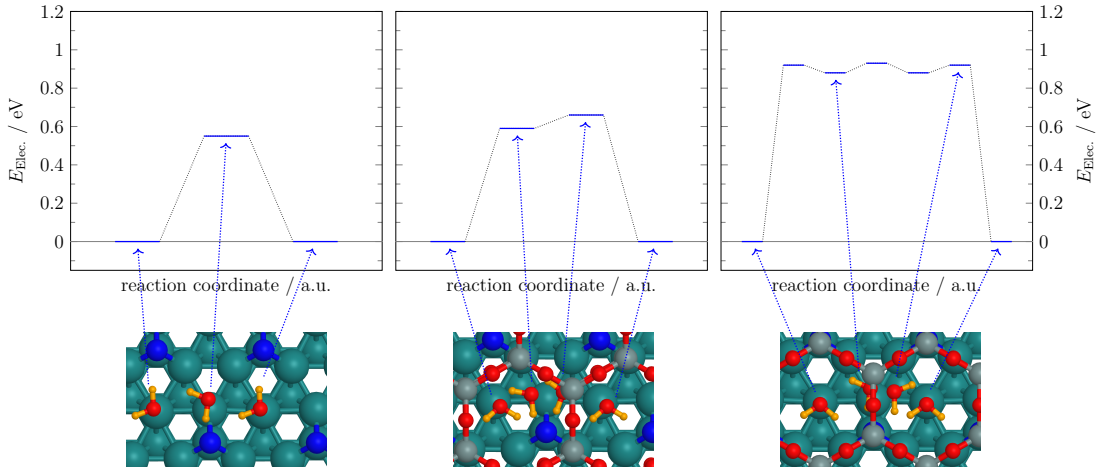

Figure 3.11: MEPs for the diffusion of water on a bare 1O surface (left), as well as one equipped with a constrained (middle) and a optimized bilayer (right). The movement of the bilayer in the optimized case has been omitted for clarity. The path completes one unit cell and wraps around itself. Surface oxygen atoms are colored in blue for distinction from water and the bilayer.

The barriers that were obtained for the bare surface are larger than those found for hydrogen and hydroxyl diffusion, being attributed to the strong interactions between water molecules and adsorbed oxygen atoms. The MEP between the two on-top positions has a rather flat maximum where only the highest point is shown. For the free moving bilayer, two additional, shallow minima are found when the bilayer moves in such a way that the water molecule can interact both with the bilayer and the additional oxygen atom on the surface. It should be noted, that the movement of the bilayer in the optimized case is not shown. In the constrained case, the shallow minima between the two on-top positions as seen in the optimized case vanish and are replaced by a plateau as in the bare case. The addition of the bilayer, especially for the free moving case, considerably raises the transition state energies to almost match the formation of OH groups from H and O. The chance of water desorbing before having diffused a considerable distance on the surface is thus very likely.

3.1.5 Micro-kinetic Modeling

Acknowledgment The following paragraphs will summarize the results obtained in the previous sections as well as extend the discussion to a mathematical model of the reaction kinetics. These simulations were carried out by Dr. Mark Schlutow from the Freie Universität Berlin and are shown here to provide deeper insight into the obtained results. In addition, we will use arguments obtained from experiments by Dr. Mauricio Prieto, Dr. Thomas Schmidt and others from the Fritz-Haber Institute of the Max-Planck Society Berlin. Further details can be found in the corresponding publication.[135]

In the preceding sections, we have investigated the relevant parts of the PES for the water formation reaction on a ruthenium surface. In order to investigate entropic effects at the experimental temperatures and further have access to rate constants, we calculated the Gibbs free energy surface, associated with the points discussed above for various temperatures. The summary for the reaction cascade

$$\mathrm{H_2}^{(g)} + 2* \underset{\mathrm{k_{-1}}}{\overset{\mathrm{k_1}}{\rightleftharpoons}} 2\,\mathrm{H}_* \tag{3.4a}$$

$$\mathrm{O}_* + \mathrm{H}_* \underset{\mathrm{k_{-2}}}{\overset{\mathrm{k_2}}{\rightleftharpoons}} \mathrm{OH}_* + * \tag{3.4b}$$

$$\mathrm{OH}_* + \mathrm{H}_* \underset{\mathrm{k_{-3}}}{\overset{\mathrm{k_3}}{\rightleftharpoons}} \mathrm{H_2O}_* + * \tag{3.4c}$$

$$\mathrm{H_2O}_* \underset{\mathrm{k_{-4}}}{\overset{\mathrm{k_4}}{\rightleftharpoons}} \mathrm{H_2O}^{(g)} + * \tag{3.4d}$$

$$2\,\mathrm{OH}_* \underset{\mathrm{k_{-5}}}{\overset{\mathrm{k_5}}{\rightleftharpoons}} \mathrm{H_2O}_* + \mathrm{O}_* \quad , \tag{3.4e}$$

where $*$ represents a free binding site on the surface, except for the last step, for $T = 500\,\mathrm{K}$ is shown in fig. 3.12. It should be noted, that the adsorption steps (transition states a) and b)) are computed for a 1O surface, while all subsequent steps are computed for a 2O surface to mimic the reaction front conditions.

The additional transition states for the adsorption of hydrogen and desorption of water, that are introduced by the confinement, are clearly visible. Furthermore, the rate-determining step, the formation of OH from H and O, is not changed between any of the systems, while the subsequent formation of water from OH and H is strongly dependent on whether the position of the bilayer is constrained or not. However, since all steps after the formation of OH are considerably faster, we conclude that the observed change in the reaction upon confinement is not introduced by the transition state effect, but is rather a result of the

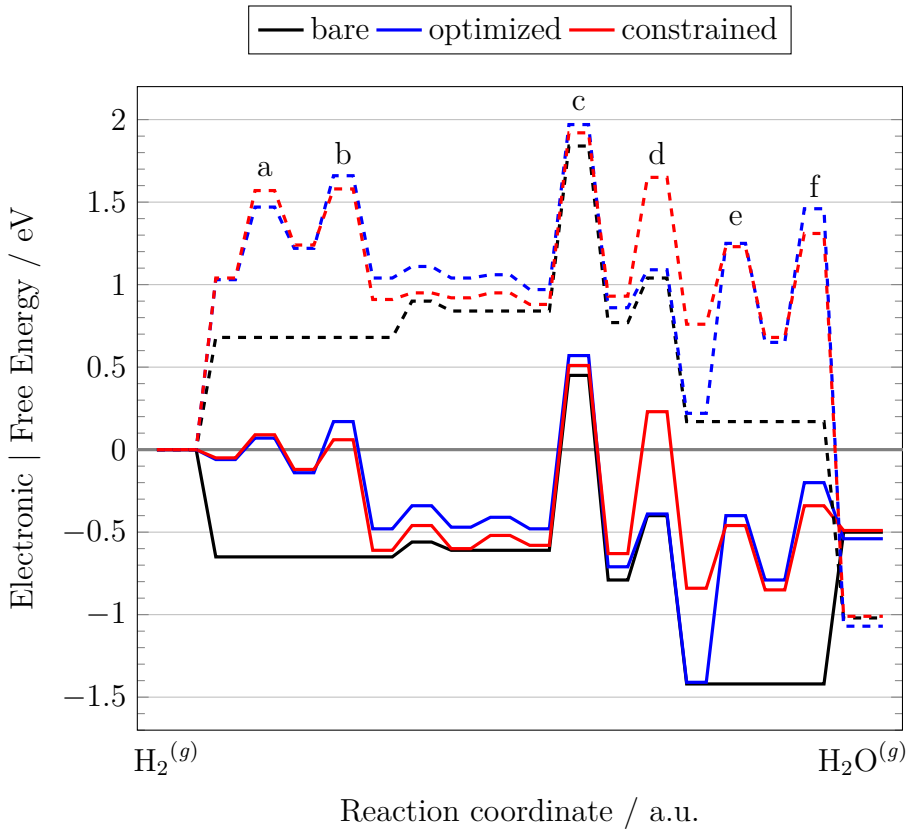

Figure 3.12: Electronic and Gibbs free energies (dashed lines) at $T = 500\,\mathrm{K}$ for the reaction cascade eqs. (3.4a) to (3.4d). Note that the first two steps (i.e. the adsorption of hydrogen) correspond to the process on a 1O surface, while all subsequent processes are calculated for a 2O surface. Transition states a) and b) correspond to the penetration of hydrogen through the bilayer, c) to the formation of OH from O and H, d) to the formation of water from OH and H and e) and f) correspond to the desorption of water through the silica bilayer.

k_i	$[k_i]$	bare	confined optimized	confined constrained
k_1	$\mathrm{m^2\,s^{-1}}$	3×10^{-15}	4×10^{-23}	4×10^{-22}
k_{-1}	$\mathrm{m^2\,s^{-1}}$	7×10^{-7}	3×10^{-13}	3×10^{-13}
k_2	$\mathrm{m^2\,s^{-1}}$	2×10^{-16}	2×10^{-16}	1×10^{-16}
k_3	$\mathrm{m^2\,s^{-1}}$	5×10^{-9}	1×10^{-8}	1×10^{-13}
k_4	$\mathrm{s^{-1}}$	1×10^{13}	4	2×10^{8}
D_H	$\mathrm{m^2\,s^{-1}}$	5.6×10^{-9}	1.9×10^{-9}	1.9×10^{-9}

Table 3.2: Kinetic rate constants k_i for the reaction cascade eqs. (3.4a) to (3.4e), as well as for the diffusion of hydrogen for a temperature of $T = 500\,\mathrm{K}$.

additional transition states for the adsorption and desorption of hydrogen and water, respectively. Furthermore, except for the loss of translational entropy going from the gas phase to the adsorbed state, the free and electronic energy surfaces are largely equivalent.

In order to evaluate the kinetic properties of the system, we calculated the rate constantss k_i for all steps in eqs. (3.4a) to (3.4e), as well as the diffusion coefficient for hydrogen D_H for various temperatures using the Eyring equation 2.176. The obtained values for $T = 500\,\mathrm{K}$ are summarized in table 3.2. It should be noted that the adsorption and desorption of hydrogen and water in the confined cases respectively, are comprised of two transition states with one minimum in between. Since the minimum of the hydrogen adsorption is shallow, we only consider the highest point on this path as the transition state from which we compute the rate constantss k_1/k_{-1}. For the desorption of water, the minimum is considerably deeper, thus opening the possibility of water-entrapment and re-adsorption to the surface. We thus compute effective rate-constants for the reaction $\mathrm{H_2O_*} \underset{\mathrm{k_{-e}}}{\overset{\mathrm{k_e}}{\rightleftharpoons}} \mathrm{H_2O^{cage}} \xrightarrow{\mathrm{k_f}} \mathrm{H_2O^{(g)}}$ in this case according to[149]

$$k_4^{\mathrm{eff.}} = \frac{k_e k_f}{k_e + k_{-e} + k_f} \quad . \tag{3.5}$$

It becomes immediately obvious, that the rate constants reflect the strong influence of the bilayer on the rate for adsorption of hydrogen (k_1 / k_{-1}) and the desorption of water (k_4). The extremely high values for the desorption and adsorption in the bare case corroborate very short residence times of the water molecule on the surface. Furthermore, the water concentration on the surface may

be estimated from the obtained kinetic rate constantss as

$$\theta_{\mathrm{H_2O}}^{\mathrm{max.}} = \frac{1}{4}\frac{k_2}{k_4}\sqrt{\frac{k_1}{k_{-1}}} \qquad , \tag{3.6}$$

which indicates, that the concentration during the reaction in all considered cases (estimated $3.9 \cdot 10^{-15}$, $1.7 \cdot 10^{-3}$, and $5.4 \cdot 10^{-11}$ ML for the bare, confined optimized, and constrained optimized case, respectively) remains low.

In the following paragraphs, we summarize the findings that were made upon utilization of the acquired rate constants in a micro-kinetic model, consisting of the following spatio-temporal differential equations:

$$\frac{\mathrm{d}n_{\mathrm{H}}}{\mathrm{d}t} = -2k_{-1}\, {n_{\mathrm{H}}}^2 + 2k_1\, {n_*}^2 - k_2\, n_{\mathrm{H}}\, n_{\mathrm{O}} - k_3\, n_{\mathrm{H}}\, n_{\mathrm{OH}} + D_{\mathrm{H}}\, \frac{\mathrm{d}^2 n_{\mathrm{H}}}{\mathrm{d}x^2} \tag{3.7a}$$

$$\frac{\mathrm{d}n_{\mathrm{O}}}{\mathrm{d}t} = -k_2\, n_{\mathrm{H}}\, n_{\mathrm{O}} \tag{3.7b}$$

$$\frac{\mathrm{d}n_{\mathrm{OH}}}{\mathrm{d}t} = k_2\, n_{\mathrm{H}}\, n_{\mathrm{O}} - k_3\, n_{\mathrm{H}}\, n_{\mathrm{OH}} \tag{3.7c}$$

$$\frac{\mathrm{d}n_{\mathrm{H_2O}}}{\mathrm{d}t} = k_3\, n_{\mathrm{H}}\, n_{\mathrm{OH}} - k_4\, n_{\mathrm{H_2O}} \tag{3.7d}$$

$$n_* = n^0 - n_{\mathrm{H}} - n_{\mathrm{O}} - n_{\mathrm{OH}} - n_{\mathrm{H_2O}} \qquad , \tag{3.7e}$$

where n^0 is the density of possible adsorption sites per unit cell, n_i is the surface coverage of the i-th component, D_{H} is the diffusion coefficient for hydrogen, t is time and x denotes the spatial dependence.

As is obvious, we discard the com- / disproportionation paths eq. (3.4e), as well as the diffusion of OH and H_2O species over the surface. For the bare and constrained bilayer cases, average residence times of water molecule estimated from computed diffusion coefficients are very short ($< 10^{-9}$ s), corresponding to near-instant desorption, while for the optimized bilayer we estimate a traveling distance of water molecules of around 3×10^{-3} nm, indicating that desorption still occurs within the reactive region of the front. While the contribution of the disproportionation channel eq. (3.4e) has been shown to be important for the WFR on Pt(111), it was attributed to the increased water coverage at lower temperatures observed in the experiment.[131] As was argued, in our case water coverage is expected to be very low, thus rendering this channel improbable. Additionally, experimental results based on high resolution electron energy loss

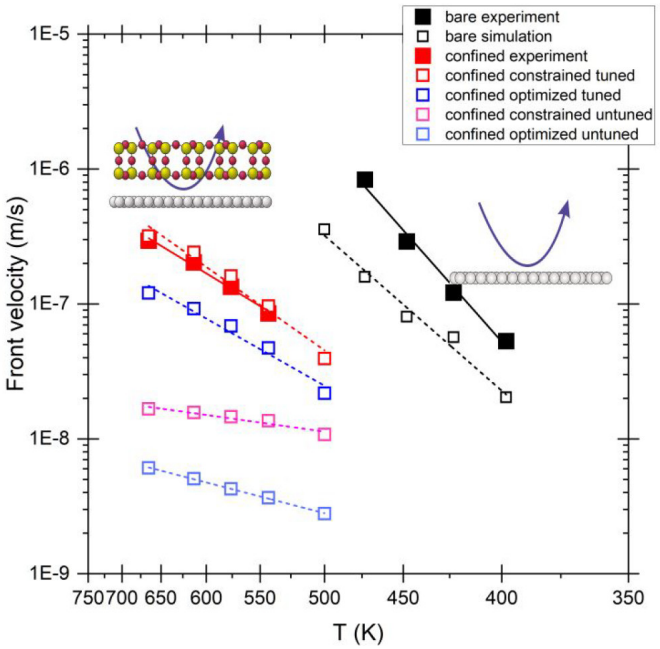

Figure 3.13: Theoretically and experimentally obtained front velocities as a function of the temperature. The simulated curves shown correspond to the data obtained correlating most with experimental findings. Reproduced with permission from the authors.[135]

spectroscopy (HREELS) indicate that the OH concentration on the surface for the system under consideration must be low as well, as it could not be detected during the reaction.[134] We thus disregard these channels in our kinetic model.

In order to have a certain flexibility in the kinetic model, we considered two cases for the adsorption of hydrogen: Firstly, k_1 and k_{-1} were used as obtained from our simulations and secondly, the ratio of k_1/k_{-1} was carefully adjusted, such as to optimally reproduce the reaction observed experimentally.

Using both approaches, we were able to compute the front velocities entirely from theoretical data at different temperatures and construct the corresponding Arrhenius plots, shown in fig. 3.13 together with the experimentally obtained curves. As can be seen, the first step, i.e. the adsorption / desorption of hydrogen has a strong effect on the overall kinetics of the process, and the tuned values are in very good agreement with experiment, especially for the confined constrained case. Interestingly, the "tuning" of the rate constants for k_3 (formation of water from OH and H) and k_4 (desorption) of water, did not show the same dependence on the front velocity – corroborating, that it is indeed the adsorption of hydrogen that is the key process.

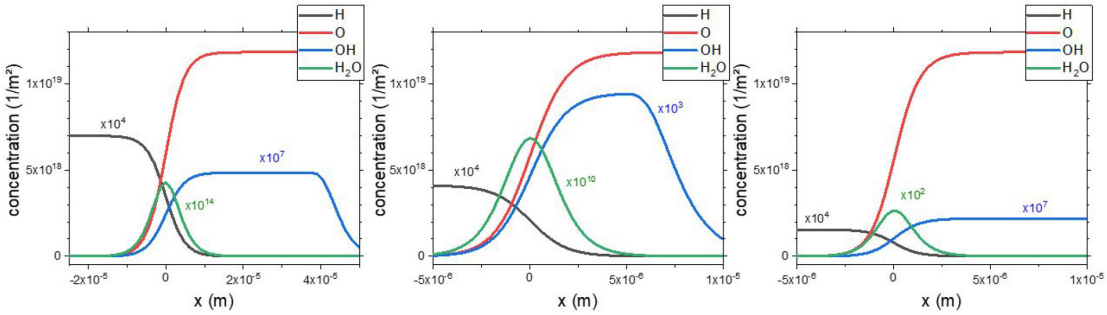

Figure 3.14: Concentration profiles of H_*, O_*, OH_* and H_2O_* for the water formation reaction obtained from the numerical simulations on (a) bare Ru(0001), (b) in confinement under a constrained SiO_2 crystalline bilayer, and (c) in confinement under an optimized SiO_2 crystalline bilayer. All concentration profiles correspond to the simulations exhibiting the best fits in the Arrhenius plots with the experimental profiles. Profiles calculated at 500 K by using k values for untuned and tuned cases for the non-confined and confined optimized and constrained BL scenarios, respectively. Note that the scaling of the y-axis is identical, while in the case of the x-axis there is a difference between confined and non-confined situations. Reproduced with permission from the authors.[135]

The kinetic model was solved on a discretized time and space grid and the resulting concentration profiles for the involved species are shown in fig. 3.14.

Our model can successfully reproduce a moving reaction front, both for the confined and non-confined scenario. In addition, the model reproduces the experimentally observed fact, that the reaction front moves slower under confinement. From the concentration profiles of OH and H_2O, we deduce that the active region is indeed limited to the front region, where their concentrations are at a maximum. Interestingly, the concentration of OH groups extends over a broad area in the unreacted part of the surface, indicating that hydrogen may be able to penetrate the 3O parts of the surface, even though there are not enough free adsorption sites available. This seems to be in line with the fact, that the diffusion barriers found for hydrogen were far less sensitive to the concentration of oxygen in the vicinity than for OH and H_2O. The successful prediction of moving fronts corroborates our assumptions. However, it should be kept in mind that some of the approximations made are rather crude and further refinement may unveil additional effects not seen here.

3.1.6 Summary and Conclusion

In the previous chapter, we have demonstrated that the water formation reaction on a Ru(0001) surface is controlled by the formation of OH from hydrogen and oxygen. The picture changes considerably when a silica bilayer is deposited atop the surface, as the additional transition states that are introduced by the porous structure impede the adsorption / desorption of hydrogen and water. The reaction mechanism as such is not strongly influenced, as the rate determining step remains the same. The formation of water from OH and H is hindered when the bilayer is constrained in its movement on the surface, indicating that at a certain concentration threshold, the bilayer may shift to accommodate more water molecules on the surface.

Under the experimental conditions, there is enough hydrogen available to quickly fill up any emerging vacancy and the process is thus determined by the formation of OH groups (k_2). However, the introduction of the confinement has a strong influence on the time required to reach the equilibrium hydrogen coverage and thus, the rate of hydrogen adsorption may become the rate limiting factor, when the hydrogen pressure is dropped such that there are not enough adsorbed hydrogen atoms on the surface within the vicinity of the surface to propagate the reaction front.

These results indicate, that a silica bilayer can be used in a variety of ways, for example as molecular sieve, since the pores have considerable influence on the ability of molecules to pass through. Furthermore, surfaces can be protected by such a bilayer, allowing only specific particles to pass. The ability to influence the surface processes without actively changing the chemical process is another point that may lead to interesting applications in catalysis or other fields of surface-science.

The presented model system, including contributions from experimental research, quantum mechanical and mathematical modeling supplies a valuable starting point for additional research that may investigate different types of ultra-thin films and surfaces. Yet, it has to be kept in mind that considerable approximations had to be introduced in order to cope with the complexity of the system, in particular to model the diffusion of surface species. Further investigations removing some of these limitations may yield further insight and possibly uncover further details that have escaped our treatment.

3.2 Plasma Functionalization of Silica Bilayers: Elucidation of Structures and Defects

Acknowledgment The findings that will be discussed in this chapter have been obtained in close collaboration with experimental insights by Dr. Mauricio Prieto and Dr. Thomas Schmidt, as well as contributions from others of the Fritz-Haber Institute of the Max-Planck Society Berlin and the Humboldt-University Berlin. Further details on the experimental setup and results can be found in the corresponding publication.[150]

3.2.1 Introduction

In the last section of this thesis we were looking at how the addition of a SiO_2-bilayer over a ruthenium surface changes the reaction kinetics of the water formation reaction on the surface, based on the confinement that is introduced by the bilayer. Our results indicated, that there is no chemical influence in how the reaction proceeds, but it is controlled by the ability of hydrogen and water to reach and leave the surface through the pores of the bilayer.

This demonstrates that reactions on surfaces can be influenced in a desired way by designing specific surface terminations or coverages by other materials and functional groups. This is not only of tremendous importance in heterogeneous catalysis, but also for example in biochemistry, where two-dimensional metal oxides such as molybdenum and manganese oxides have been studied as mechanism for drug delivery, bioimaging and biosensing, owing to their low toxicity and ability to be modified by doping, defect formation and functionalization by plasma treatment.[151] In this sense, the surfaces of these materials often act as a vehicle to increase local concentration of loaded substances and deliver them to the desired position.

Particularly silica based materials are of elevated interest, because of their wide abundance in nature[†] and their large variety in polymorphs ranging from the completely amorphous structure found in glass, to well ordered 3-dimensional crystals as found for example in zeolites, or the previously introduced ultra-thin silica films. Additionally, the abundance of silanol terminal groups in many of these materials renders them as prime candidates for anchoring substances either

[†]Silicon and oxygen are the most abundant elements in earth's crust.

via electro-static interactions due to the polarity of these groups, or by chemically attaching them via bridging Si−O−X bonds.[152]

Indeed, many solid state catalysts are designed in an analogous way, as they are commonly not composed of pure catalyst, but are rather manufactured by dispersing the catalyst onto other support materials such as powdered carbon, organic polymers, metals and metal oxides such as SiO_2, Al_2O_3, TiO_2 or ZrO_2. Their main purpose is to provide a large surface area and increase mechanical stability while reducing the amount of (precious) catalyst that has to be used. As mentioned before, these support materials are generally considered to be chemically inert and only provide access to the catalytic sites, however the role of the support material is still under intense research. For example, in a study investigating the selective hydrogenation of CO_2 to methanol using a silica supported cobalt catalyst, the authors proposed a mechanism where Si centers of the support actively participate in the reaction via Co−O−SiO_n linkages.[153] It is therefore crucial to get deeper insight into how these support materials actually affect the used catalyst and the reaction under consideration. A succesful example of importance for industrial applications of this type of system are vanadium-oxide based catalysts dispersed on metal oxides such as SiO_2 and TiO_2. For example, the oxidation of SO_2 to SO_3 by vanadium oxide catalysts in the contact process was invented in 1899 by R. Meyers and has evolved to become the most important vapor-phase oxidation reaction in terms of annual production amounts. The research that was triggered by this success yielded similar catalysts in other applications, such as the production of phthalic acid via the oxidation of naphtalene or *o*-xylene, synthesis of vitamin-B precursors from alkyl pyridines or the selective reduction of NO_x emissions from power plants.[154]

Raman, XANES and ^{51}V-NMR studies revealed that at low concentrations the active catalytic sites in the dehydrated catalyst are composed vanadyl V^{5+}=O groups bound to the surface in the so called *three-legged* structure via three bridging V−O−Si bonds.[154,155] At higher loadings, these monomers tend to oligomerize on the surface via bridging V−O−V bonds, while Vanadium remains in its +5 oxidation state. A sketch of the active sites is shown in fig. 3.15 on the left. The formation of the vanadium-oxide layer on the support by reaction of V_2O_5 with the terminal OH groups on the surface is thermodynamically strongly favored, so that heating of a mixture of V_2O_5 with the support material results in complete transformation of the surface into a vanadium-oxide layer.[156,157]

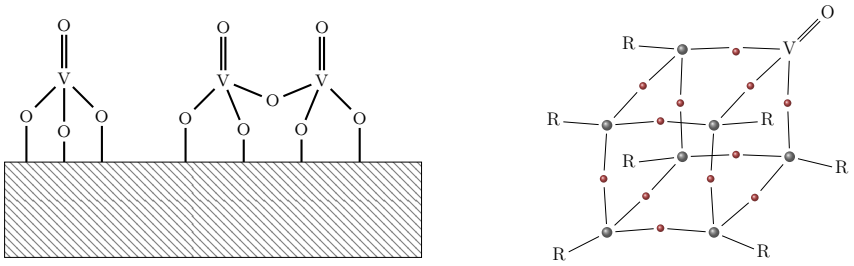

Figure 3.15: Left: Sketch of the active phase (monomer left, dimer right) in a dehydrated V_2O_5 catalyst supported on a SiO_2 surface.
Right: Corresponding POSS model with the vanadyl group in the upper right. Silicon and oxygen atoms are represented as black and red spheres, respectivley.

One of the model systems that has been developed for the study of the role of the support material on the catalytic behavior is the so called POSS (polyhedral oligomeric silsesquioxanes) family. They consist of cage-structures built up by Si-O-Si bridging bonds with various terminal groups at the edges of the cage. Thus, their chemical structure is akin to silica nano-cluster and when one or two of the Si−R corners are replaced by V=O, an excellent model of the prevailing vanadium oxide species mentioned above is obtained. A schematic representation is shown in fig. 3.15 on the right. These structures are experimentally easily available and have been suggested for example for the catalyzation of the oxidation of methanol to formaldehyde.[158] In a study using GGA and hybrid DFT methdods, Sauer et al. employed models based on POSS and finite cluster structures to study the catalytic oxidation of methanol to formaldehyde and found that the surface V^{5+} centers are reduced to V^{3+} upon coordinating the methoxy group and dissociativley adsorbing the hydrogen atom from methanol. The authors also pointed out, that the coordination between studied gas-phase POSS clusters and single-crystal surfaces is different. Even though both are composed of 4-fold oxygen coordinated vanadium centers with one vanadyl bond, the lower layers of the crystal have a non-negligible influence on the surface species.[159]

As an alternative to the study of gas-phase clusters, the new two dimensional ultra-thin silica films introduced in the previous chapter offer a new and exciting way of studying the interaction of catalysts with well-defined periodic and amorphous surfaces. The chemical robustness of the material was demonstrated in the previous sections, as exposure to oxygen and hydrogen gas at elevated temperatures did not bring about any changes in the observed LEED and LEEM spectra. This offers the

possibility to utilize it in demanding chemical environments, while it also introduces the difficulty of chemically altering it in a desired way, for example by introducing controlled defects and functional groups. The structure of the silica-bilayer is self-contained, meaning that all bonds are saturated and the registry between the top and the bottom layer is maintained by the interlayer-oxygen bonds, which makes chemically attacking the bilayer in a controlled way a challenging task.

As mentioned before, one of the possible routes is functionalization of the bilayer by introducing terminal hydroxyl (OH) groups, as these are excellent starting points for anchoring other substances. To achieve this, generally two pathways are applied. For one, directly exposing the prepared film to solutions of different pH will not only functionalize it, but also dissolve it once functionalization of the film has started, which is in line with the behavior of bulk-silica samples and nano-particles.[160,161] On the other hand, the deposition of an ice-layer atop the silica bilayer at around 100 K and subsequent desorption at elevated temperatures also introduces hydroxyl groups into the bilayer. When the ice-layer is additionally irradiated with an electron-beam, a higher yield of hydroxylation is observed, corroborating the fact that the mechanism requires activation.[162]

A different route that will be explored in this section is the exposure of the silica-bilayer film under UHV conditions to hydrogen plasma gas. This offers a new way of manipulating the demanding Si−O−Si bonds under otherwise mild chemical conditions, exploiting the presence of radicals, charged and excited species present in the plasma. Within the experimental setup discussed here, the plasma source is operated at mild temperatures (~ 300 K), leading to the assumption that the main chemically active species in the plasma are singly charged H_2^+ cations. As a result, the interaction of a single hydrogen molecule with the siloxane bonds of the bilayer is anticipated, resulting in a heterolytic bond dissociation and formation of neighboring Si−OH and Si−H hydride groups.

In order to characterize the effect of hydrogen plasma on the silica bilayer film, it was exposed to plasma for up to 64 minutes, while being periodically characterized by LEED and XPS measurements. During the experiment, the recorded LEED pattern preserved the (2×2) spots characterizing the symmetry of the film. However, overall intensity of the spots was lost in detriment of a diffuse background signal, indicating that during the reaction defects are created such that the crystallinity of the film is preserved. XPS spectra of the Si 2p and O 1s states revealed the consumption of surface-oxygen atoms remaining from

the preparation of the bilayer in alignment with our previous chapter. The same monotonic shift towards higher binding energies is observed, resulting from the removal of the interface dipole created by the adsorbed oxygen atoms. However, in addition to the expected features, a new shoulder is observed in the Si 2p spectrum at slightly lower binding energies (~ 1 eV red-shifted), indicating the emergence of a new silicon bond type.

In order to obtain further insight, complementary infrared reflection-absorption spectra (IRAS) were recorded. It should be noted at this stage, that for the IRAS characterization, the plasma source was operated using deuterium instead of hydrogen gas in order to increase distinction between background water remaining in the reaction chamber. Additionally, the spectra were both recorded under the mild conditions described before, as well as using a doubled plasma-source voltage, resulting in increased functionalization and thus a better noise to background ratio. The recorded spectra (fig. 3.16) exhibit an intense absorption at around $1290\,\mathrm{cm}^{-1}$ attributed to the collective in-phase excitation of the Si–O–Si interlayer bond, as well as two new bands at $2762\,\mathrm{cm}^{-1}$ and $1654\,\mathrm{cm}^{-1}$, which are not observed in the spectrum of the pristine bilayer. Interestingly, the interlayer Si–O–Si band continuously shifts towards lower frequencies up to $1262\,\mathrm{cm}^{-1}$, indicating that the registry between the two sheets is compromised. The appearance of the two new absorption bands are in alignment with the characteristics of Si–D and Si–OD bands, thus indicating that it is indeed single silanol bonds that are functionalized.

In the following, we use our existing silica bilayer model from the previous section and study the effect of heterolytic splitting of silanol bonds by means of single, as well as double hydrogen/deuterium addition. We compute the binding-energy shifts for the Si 2p and O 1s components in the initial state approximation as discussed in section 2.8, as well as the IRAS spectra for various possible addition scenarios in order to pin-point any structures more likely to be observed in experiment.

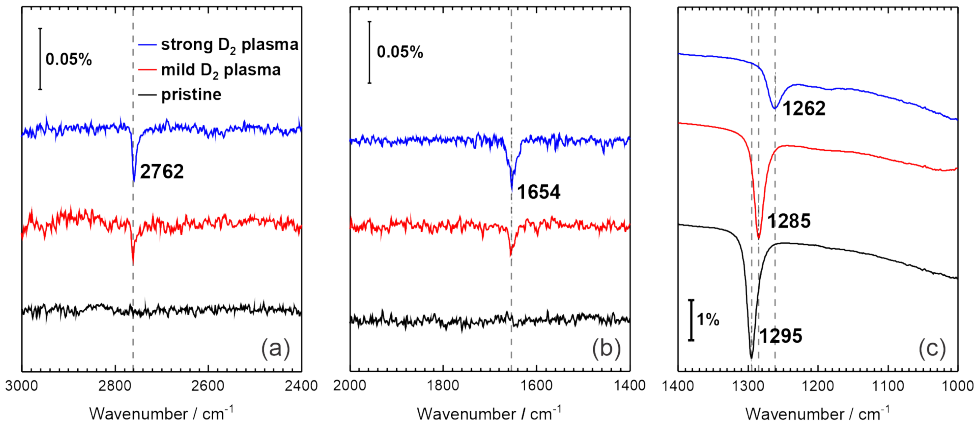

Figure 3.16: Experimentally observed IRAS spectra for a crystalline SiO_2 bilayer adsorbed on Ru(0001) before and after the plasma treatment. The characteristic O–D bands (a) and Si–D (b) bands are observed after the treatment, as well as a red-shift of the interlayer Si–O–Si band (c). Reproduced with permission from the authors.[150]

3.2.2 Description of the Employed Model

In order to obtain a model for the anticipated defect sites introduced by the hydrogen plasma, we utilize the same Ru(0001) surface equipped with a crystalline bilayer as introduced in section 3.1. However, in this instance, our structures are based on those reported in reference [162]. Within this study, the effect of the addition of two water molecules instead of hydrogen has been considered, resulting in various possible defect sites. We adapted these structures by replacing two OH groups with hydrogen atoms, corresponding to the reaction with two hydrogen molecules instead of water. The corresponding unit cell is a repeated-slab Ru(0001) surface consisting of five layers of metal atoms, of which the bottom three are fixed at bulk position at all times, while the top two were allowed to relax. The surface is covered with a 0.25 ML oxygen layer (1O surface in the nomenclature of section 3.1), resulting from the consumption of the initial 3O layer during the experiment. A representation of the unit cell for the defect-free system is shown in fig. 3.17. Within the aforementioned study, three types of defects were considered, of which we adapt the nomenclature as follows:

- Vicinal I:

  Here all defects (two OH groups and two H atoms) are evenly distributed amongst four directly neighboring Si atoms. The corresponding structures are shown in fig. 3.18.

- Geminal:

  Here two defects are located at the same Si atom, while the other two are distributed amongst the remaining two neighboring Si atoms. This is equivalent to cleaving two Si−O−Si bonds for the same Si atom. We refer to these two sets (vicinal I and geminal) as double H_2 type defects. Representations of the structures are shown in fig. 3.19.

- Vicinal II:

  This set of structures is also adapted from ref. [162], however in contrast to the other two, these structures feature covalent Si−Ru bonds between the bilayer and the metal substrate, in addition to two hydride defects in the top layer. Since this is equivalent to reacting with a single H_2 molecule as for the next set discussed (see below), we refer to these as single hydrogen type defects. The two corresponding structures are shown in fig. 3.20.

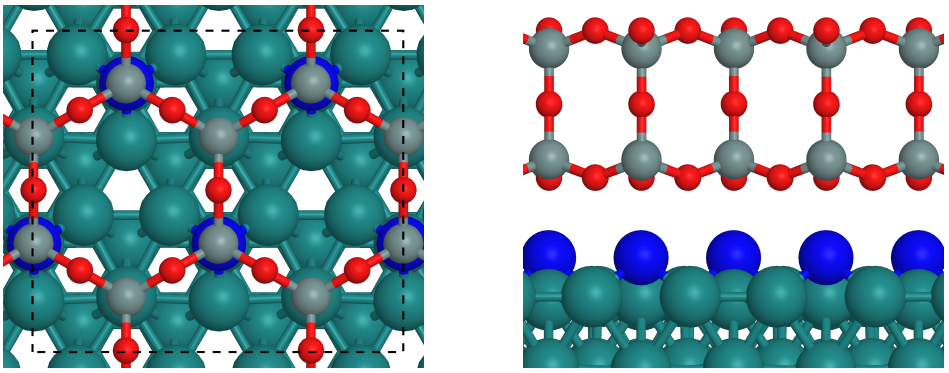

Figure 3.17: Top (left) and side (right) view of the ruthenium (0001) surface covered with a 0.25 ML oxygen coverage and a pristine SiO_2 bilayer adsorbed on one side.
Silicon, oxygen and ruthenium atoms are shown in yellow, gray, red and green, respectively. Surface oxygen atoms are colored blue for distinction from the bilayer.

In addition, a further set of structures was created by mending one of the defects described above by removing one hydrogen atom and an OH group such that the corresponding silanol bond of the bilayer was reconstituted. This also corresponds to the addition of a single hydrogen molecule to the bilayer. The obtained trial structures are shown in fig. 3.21.

All obtained structures were re-optimized. Note that the numbers used in our nomenclature – 1 and 2 – refer to structural isomers of the same type, that include different hydrogen bonding motifs between hydroxyl groups and the interlayer oxygen atoms of the silica bilayer.

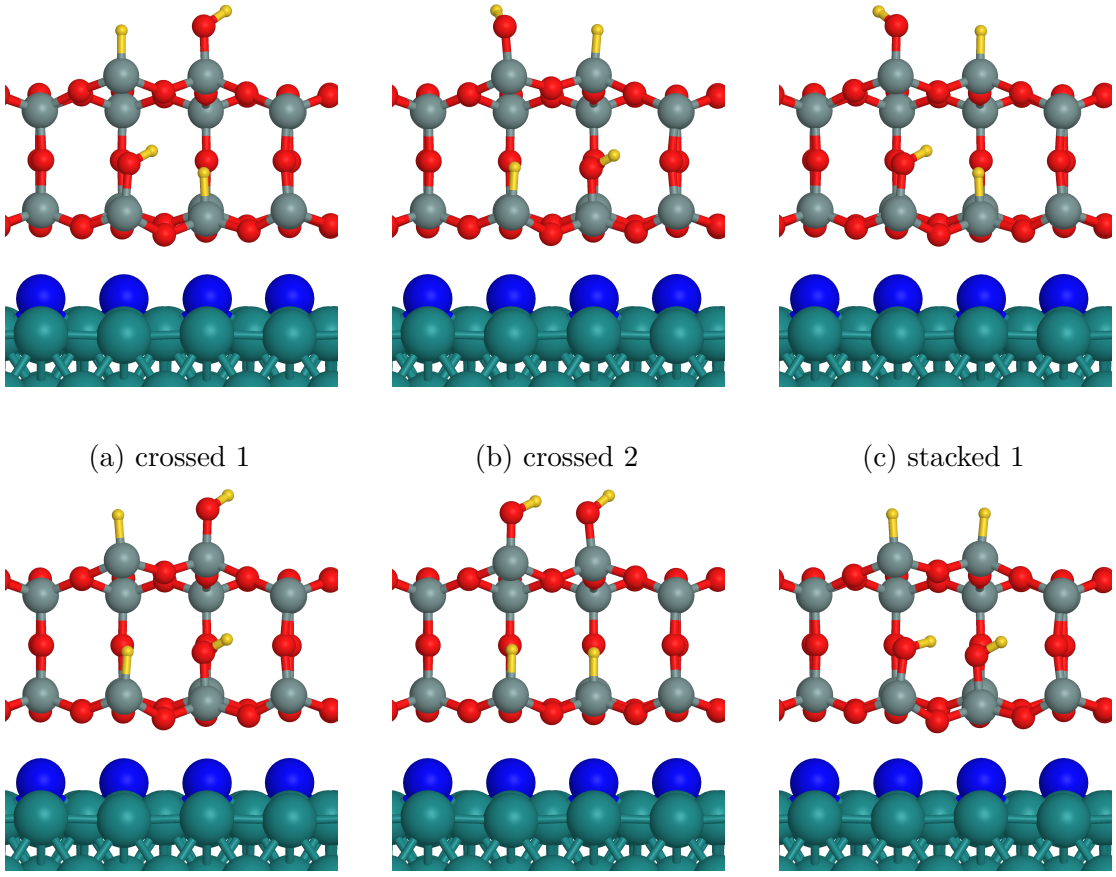

(a) crossed 1 (b) crossed 2 (c) stacked 1

(d) stacked 2 (e) sameside 1 (f) sameside 2

Figure 3.18: Different bilayer configurations for vicinal I type geometries. The number – 1 or 2 – labels different permutations of the OH groups. Hydrogen, silicon, oxygen and ruthenium atoms are shown in yellow, gray, red and green, respectively. Surface oxygen atoms are colored blue for distinction from the bilayer.

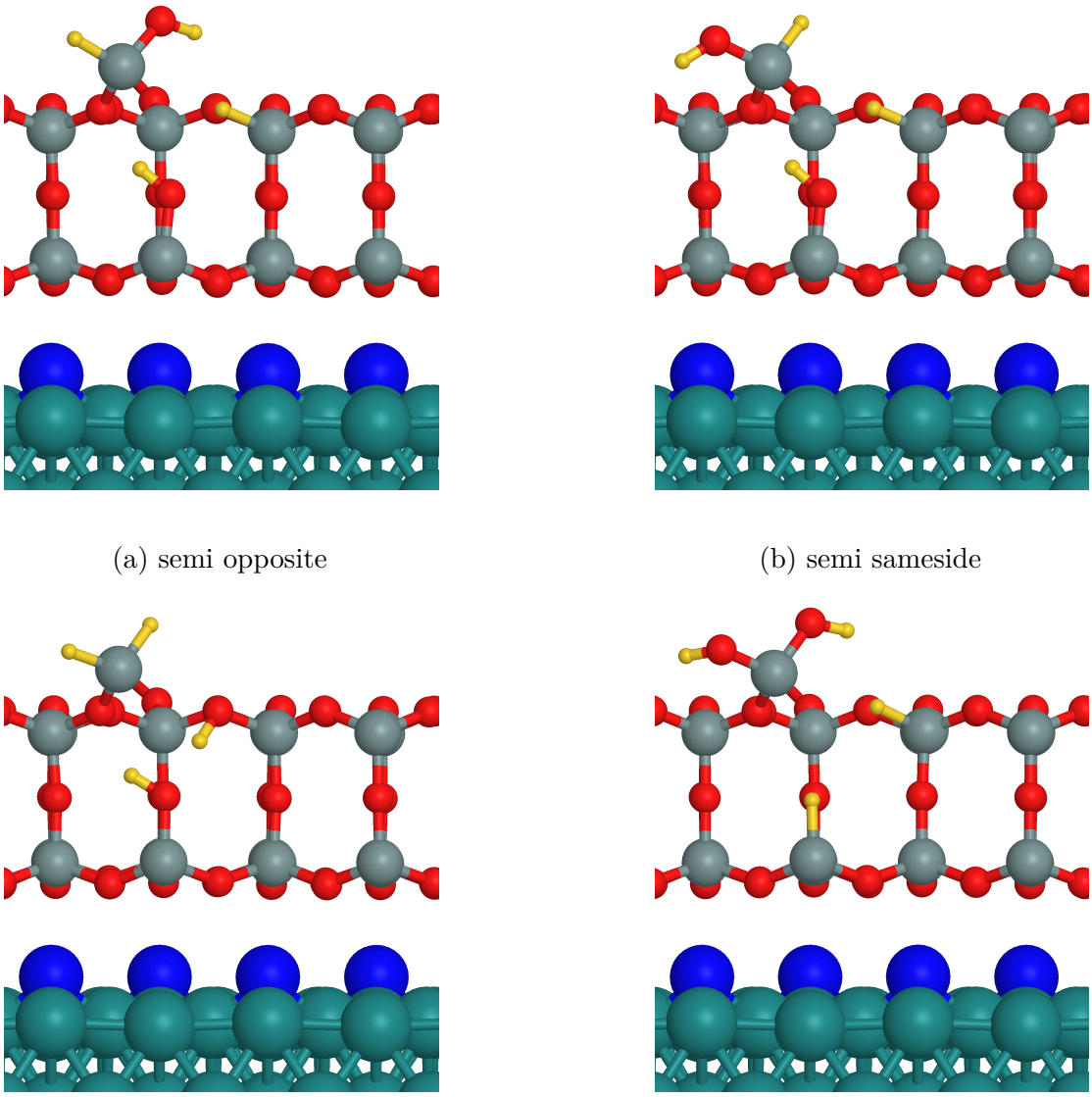

(a) semi opposite

(b) semi sameside

(c) geminal

(d) inside

Figure 3.19: Different bilayer configurations for geminal type geometries. Hydrogen, silicon, oxygen and ruthenium atoms are shown in yellow, gray, red and green, respectively. Surface oxygen atoms are colored blue for distinction from the bilayer.

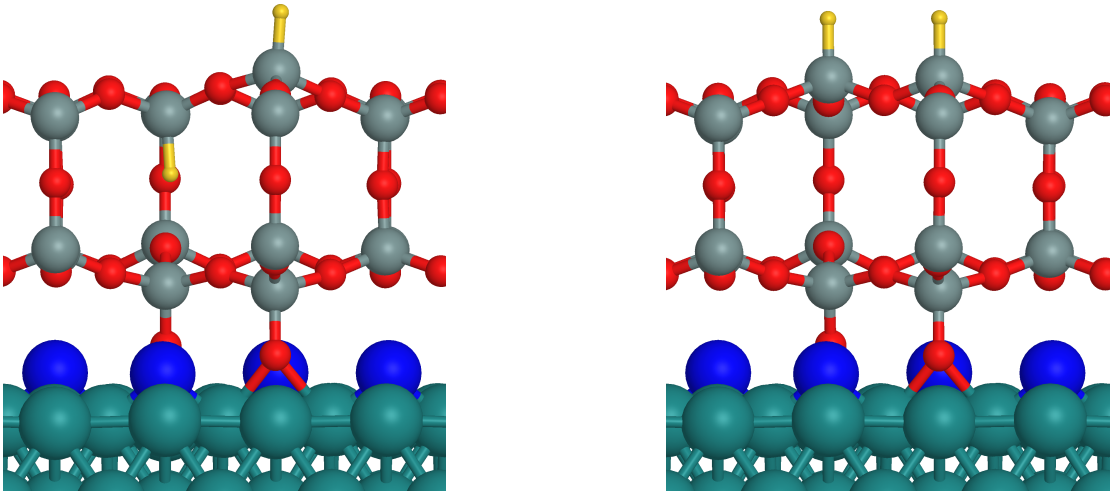

(a) opposite (b) sameside

Figure 3.20: Different bilayer configurations for vicinal II type geometries. Hydrogen, silicon, oxygen and ruthenium atoms are shown in yellow, gray, red and green, respectively. Surface oxygen atoms are colored blue for distinction from the bilayer.

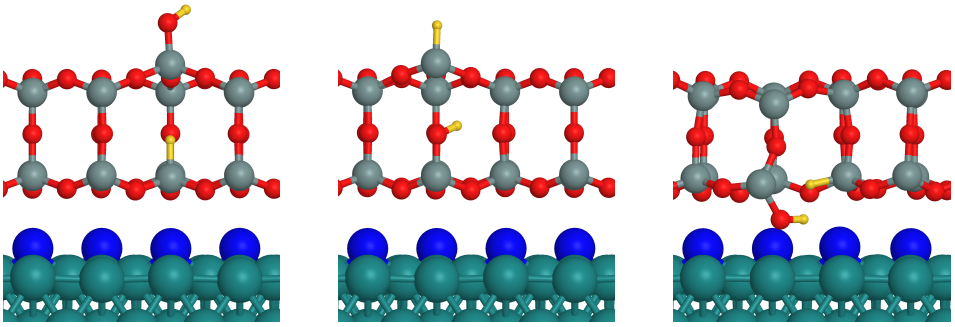

(a) OH top (b) OH bottom (c) both bottom

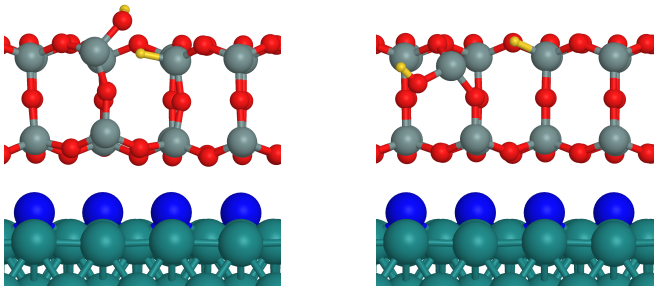

(d) both top (e) both top flipped

Figure 3.21: Different bilayer configurations for bond-saturating single H_2 type geometries.
Hydrogen, silicon, oxygen and ruthenium atoms are shown in yellow, gray, red and green, respectively. Surface oxygen atoms are colored blue for distinction from the bilayer.

3.2.3 Employed Computational Methods

Structure optimizations, as well as evaluation of infrared (IR) spectra and binding energy (BE) shifts were performed at the DFT level, using the PBE functional[78] and an additional dispersion correction D2.[89] Calculations were carried out, using the plane-wave code VASP,[140] employing the projector-augmented wave method to represent core states. The first Brillouin zone was sampled using a weighted, uniform $4 \times 4 \times 1$ k-point grid.[142] The plane wave energy cut-off was chosen to be $E_{\mathrm{PW}} = 400\,\mathrm{eV}$. To accelerate SCF convergence, a Methfessel-Paxton[163] type smearing with a width of 0.05 eV was utilized. The convergence thresholds in the structure optimizations were $5 \times 10^{-3}\,\frac{\mathrm{eV}}{\mathrm{Å}}$ for forces and $1 \times 10^{-5}\,\mathrm{eV}$ for the change in electronic energy. BE shifts were estimated using the initial state approximation as introduced in section 2.8, while infrared intensities were obtained from finite-difference dipole-moment derivatives within the harmonic approximation.

For the calculation of IR spectra, the ruthenium slab was reduced to three layers and subsequently re-optimized with only the bottom layer fixed at bulk position. The displacements of the Ru atoms were excluded from the computed Hessian matrix. A dipole correction was added, in order to compensate for spurious interactions due to the dipole moment in the direction orthogonal to the surface. The Hessian matrix and the dipole moment changes were evaluated, using a central finite-differences scheme. For comparison to experimental IR spectra, the calculated intensities include only the component orthogonal to the surface of the respective dipole moments.

To correct for systematic errors within the harmonic DFT calculations, the frequencies of the Si–O–Si modes were scaled by a factor of $f_{\mathrm{SiOSi}} = 1.0341$,[164] the O–D modes by a factor of $f_{\mathrm{OD}} = 0.9951$,[162] while the Si–D mode frequencies were not scaled. The latter was based on the fact, that the harmonic PBE-D2 frequencies for the SiD_4 molecule virtually reproduce the experimental values (PBE-D: $1589.5\,\mathrm{cm^{-1}}$, $1589.3\,\mathrm{cm^{-1}}$, $1589.2\,\mathrm{cm^{-1}}$; experiment:[165] $1592.7\,\mathrm{cm^{-1}}$, $1589.2\,\mathrm{cm^{-1}}$, $1584.7\,\mathrm{cm^{-1}}$).

3.2.4 Comparison of Experimental and Theoretical X-Ray Photoelectron Spectra

In a first step, we computed the core-level binding energy shifts between the crystalline system and the defect sites. To this end, the O(1s) and Si(2p) core level shifts obtained for the atoms participating in the defect were subtracted from the average core level energies for the respective atoms in the pristine bilayer:

$$\Delta BE_i = E_i^{\text{defect}}(1\text{s}/2\text{p}) - E_{\text{cryst.}}^{\text{aver.}}(1\text{s}/2\text{p}) \qquad , \tag{3.8}$$

where ΔBE_i is the binding energy shift for the i-th defect atom, $E_i^{\text{defect}}(1\text{s}/2\text{p})$ is the core-level eigenvalue for the considered state and $E_{\text{cryst.}}^{\text{aver.}}(1\text{s}/2\text{p})$ is the average core level value for the crystalline system.

The obtained ΔBE values are shown in figs. 3.22 to 3.25 for the atoms under consideration. In general, all investigated core-level shifts exhibit a uniformly negative trend in the range between 0 and $-0.8\,\text{eV}$. In all cases, the silica atoms containing a hydride group show a slightly stronger shift than the hydroxylated species. In both cases, there is scattering between seemingly comparable species and an unambiguous trend of the shift depending for example on hydrogen-bonding could not be observed.

For the single H_2 type structures, there is one outlier for the "both bottom" type geometry (fig. 3.25), likely resulting from the strong interaction of the OH group with the metal interface. Although these results are in line with the experimental shifts, they do not allow for identifying any particular candidate structures. In order to characterize distinct features for each structure, we calculated the IR spectra for all considered structures, so as to provide a comparison to experiment.

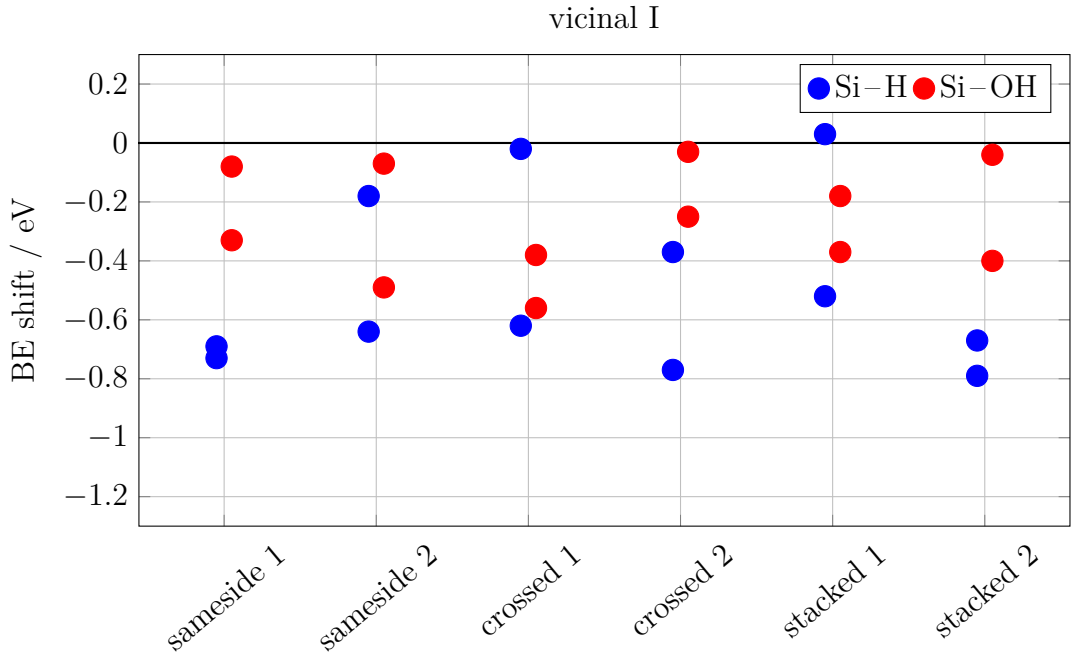

Figure 3.22: Vicinal I Si 2p BE shift values for selected atoms obtained within the inital state approximation.

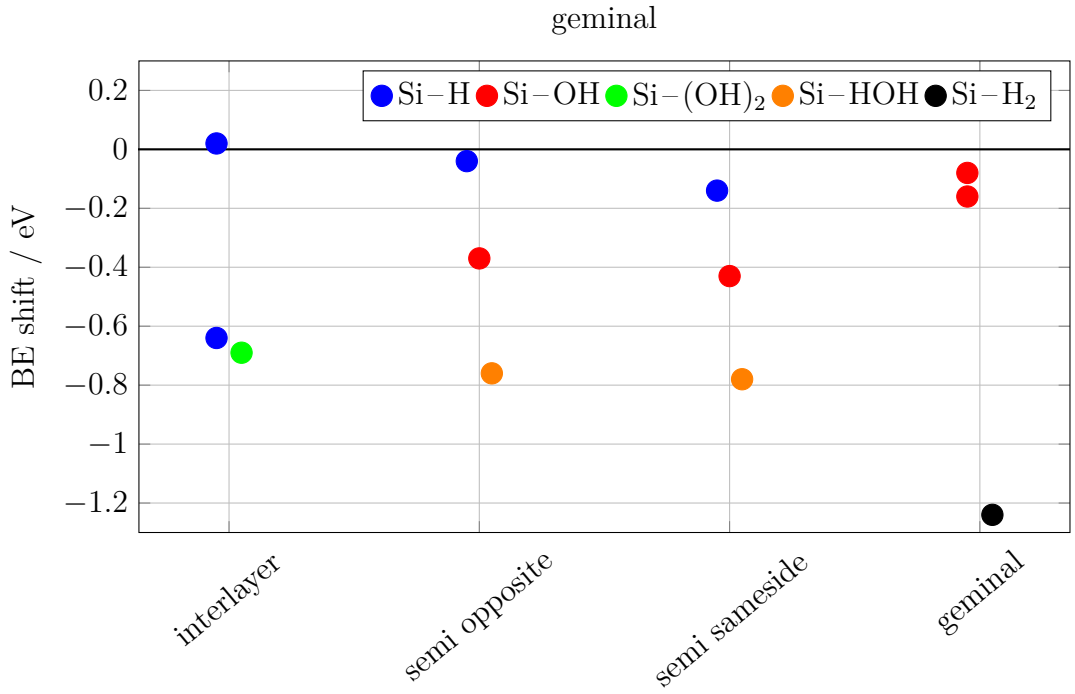

Figure 3.23: Geminal Si 2p BE shift values for selected atoms obtained within the inital state approximation.

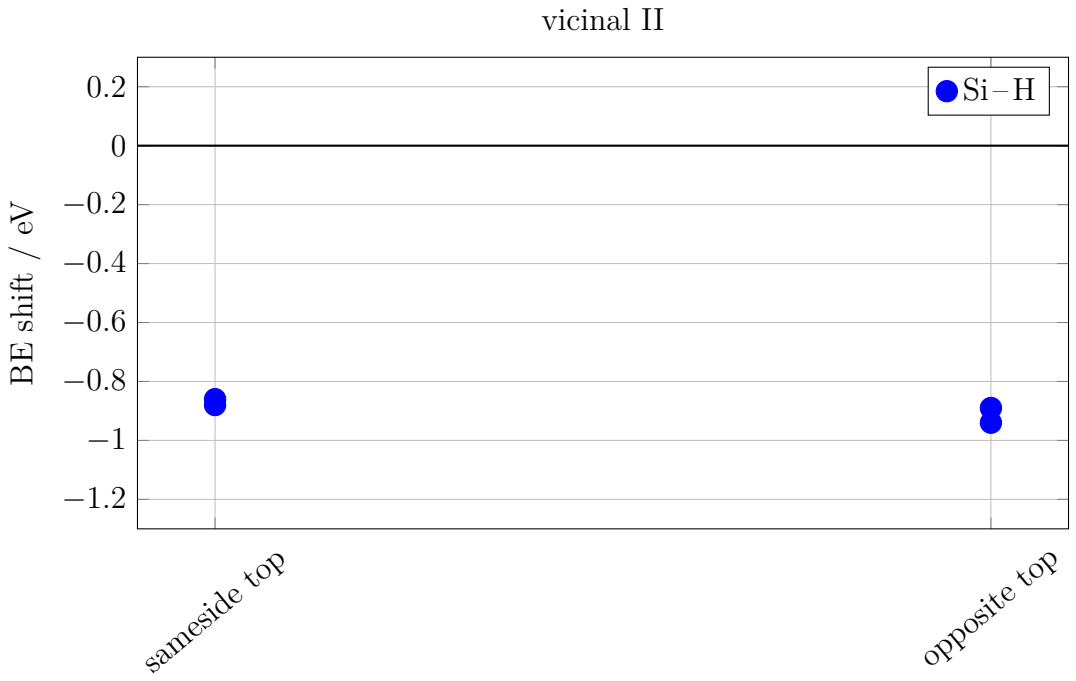

Figure 3.24: Vicinal II Si 2p BE shift values for selected atoms obtained within the inital state approximation.

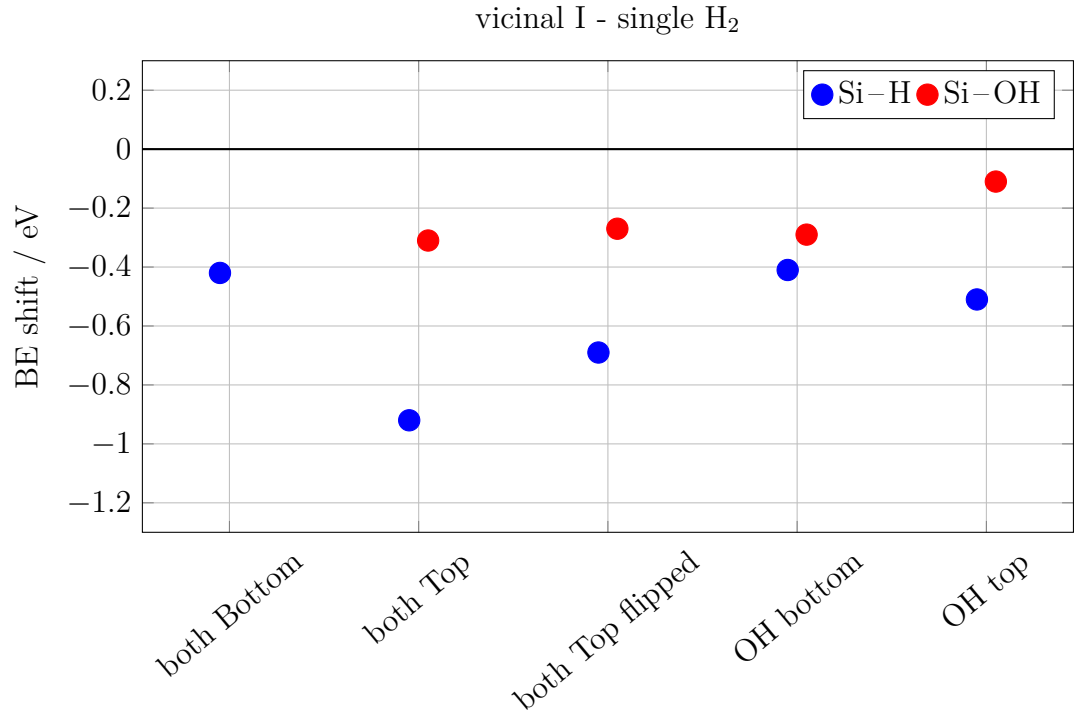

Figure 3.25: Bond-saturating single H_2 Si 2p BE shift values for selected atoms obtained within the inital state approximation.

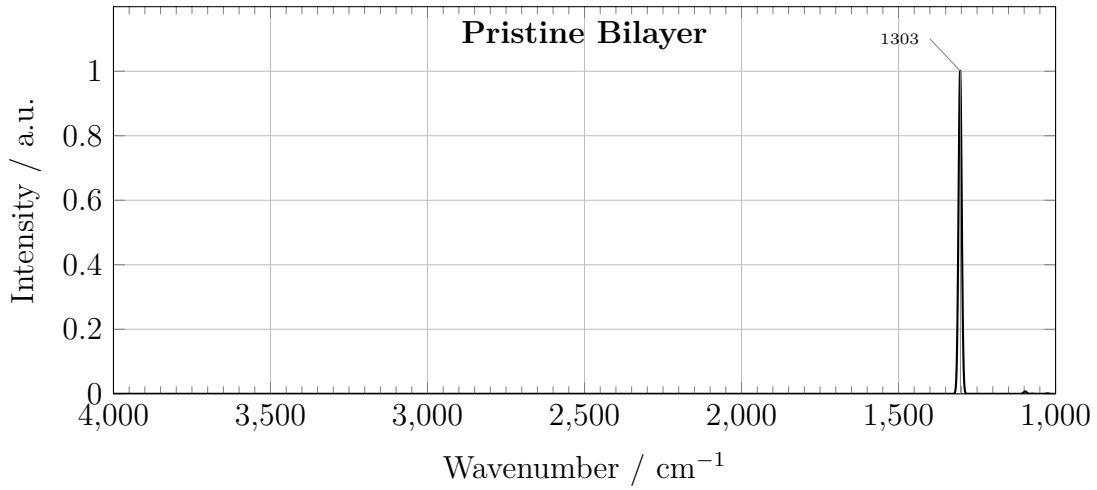

Figure 3.26: The IR absorption spectrum for the pristine bilayer, calculated using the z-component of the dipole-moment derivative only.

3.2.5 Comparison of Experimental and Theoretical Infrared Absorption Spectra

3.2.5.1 Pristine Bilayer

For the IR characterization, in a first step, the spectrum of the pristine, crystalline SiO_2 bilayer adsorbed on a (0001) ruthenium surface (fig. 3.17) was calculated and the result is shown in fig. 3.26. It should be noted that the plots only show the obtained spectra in the wavenumber range $> 1000\,\mathrm{cm}^{-1}$, since this is the experimentally accessible range that was compared to.

The spectrum features a single distinctive peak, which is attributed to the symmetric stretching mode of the interlayer oxygen bonds at $1303\,\mathrm{cm}^{-1}$. A second peak, identified with the distortion of the SiO_4-tetrahedron motifs at $633\,\mathrm{cm}^{-1}$ is not within the observed range. These findings are in alignment with the single peak observed at $1295\,\mathrm{cm}^{-1}$ in experiment.

3.2.5.2 Defective Bilayer

The following figures show the IR spectra, that were calculated for the structures discussed above, where all hydrogen atoms have been replaced with deuterium atoms. For all calculations, the ruthenium atoms were excluded in the calculation of the Hessian matrix and dipole moments, i.e. they act as a rigid support material.

The figures are in order of appearance:

- Vicinal I — Figure 3.27
- Geminal — Figure 3.28
- Vicinal II — Figure 3.29
- single-H_2 — Figure 3.30

In general, the plots for the defect structures feature the O–D stretching modes at around 2450 – 2800 cm^{-1}, Si–D stretching modes at around 1550 – 1700 cm^{-1} and a strong peak of the interlayer oxygen stretching mode slightly below 1300 cm^{-1}. Comparing the latter to the frequency of the Si–O–Si vertical stretch of the pristine bilayer, one can see a redshift for this mode by 15 – 30 cm^{-1}, for all defects considered. This redshift is also observed in experiment, where with continuous plasma exposure time, the band shifts from 1295 cm^{-1} up to 1262 cm^{-1}. This is attributed to the degradation of the registry between the two sheets, which has a strong impact on this mode.

For the double H_2 and vicinal II type defects, the deviation in the chemical environment for the different OD or SiD groups results in a splitting of the O–D and/or Si–D bands. The only exceptions are geminal – inside and vicinal II – sameside geometries.

In general, a hydroxyl group in the top layer is only able to interact via hydrogen bonding if both OD groups are located on the top layer, while OD groups in the bottom layer may also interact with the interlayer oxygen atoms of the silica bilayer. Consequently, the top O–D stretching mode is largely independent of other defects, while the bottom mode does show a dependence.

More subtle effects are observed for the structural isomers of the same type, where different locations of the OD groups influence also the position of the Si–D stretching mode. This results, for example, in the "inversion" of the Si–D stretching modes, observed in the vicinal I – crossed case or the splitting of the degenerate Si–D stretching mode in the vicinal I – stacked case.

Vicinal I Type Defects The vicinal I type defect consists of two OD and two deuterium terminated silicon atoms, resulting from the attack of two deuterium molecules on the intralayer oxygen bonds. From the six different geometries under consideration, the sameside – 1 is different from the crossed and stacked

configurations, as it features twice the same defect in one layer, while for the others, the two defect types are always distributed evenly across the top and bottom layer.

This property is also observed in the corresponding infrared spectra (Fig. 3.27 bottom), where the peaks corresponding to the O–D stretching mode are redshifted considerably between the two isomers sameside – 1 and sameside – 2, while for the other structures, they are largely comparable.

Geminal Type Defects Similar to the vicinal I type defects, the geminal structures are formed by attack of two Si–O–Si-intralayer bonds, however in this instance, one of the participating silicon atoms carries both defects. Due to the alignment of the OD-groups on the upper defect with the xy-plane, there is almost no change in the z-component of the dipole moment vector when stretching this bond. Consequently the intensities in the IR spectrum are extremely low.

Vicinal II Type Defects For the vicinal II type geometries, the additional bilayer-substrate bonds alter the chemical environment considerably. Additionaly, due to the absence of hydroxyl groups in these structures, the corresponding bands are entirely missing in the spectrum (fig. 3.29).

Single H_2 Type Defects The main difference between the single H_2 and the other defects is, that there is exactly one Si–H(D) group and one OH (OD) group per unit cell (rather than two or none). Consequently, there is exactly one peak for the stretching mode of each group in the spectrum. However, for some of the structures (both-bottom, both-top and both-top-flipped), these peaks are extremely weak, as the defects are oriented parallel to the surface and therefore a virtually zero dipole change occurs along the z-coordinate as observed before.

Comparision to Experiment The computed IR spectra show the anticipated O–D and Si–D stretching modes, however their exact position depends considerably on the direct environment.

Since within experiment, only a single peak is observed for each region ($2762\,\mathrm{cm}^{-1}$ for the O–D and $1654\,\mathrm{cm}^{-1}$ for the Si–D stretching), we conclude that the silanol bonds are attacked “one by one“ instead of a clustered occurrence, that is the single H_2 and vicinal II type geometries are candidates only. However, for the latter the strong interaction of the covalently bound bilayer to the surface shifts the calculated adsorptions considerably out of the observed range.

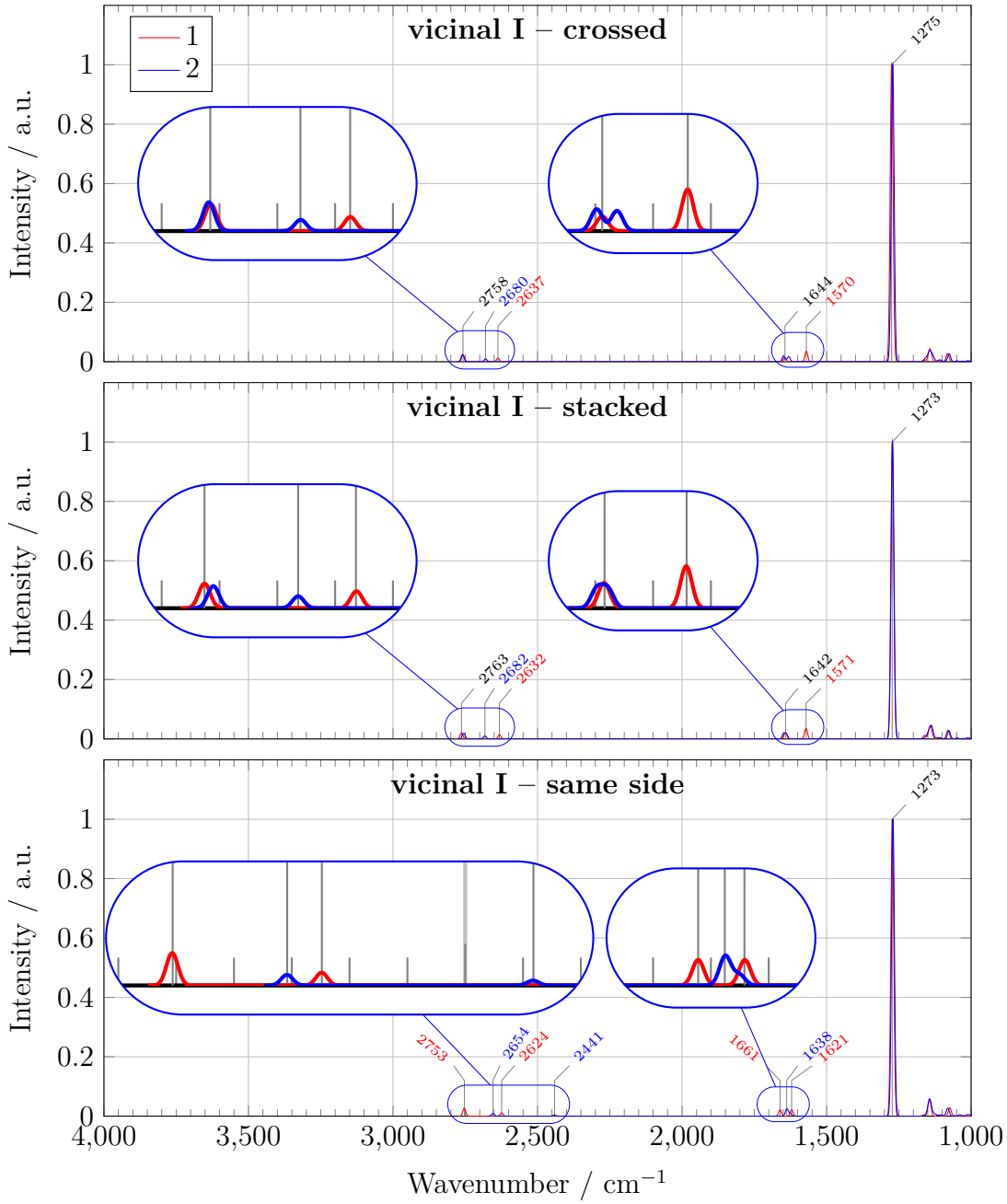

Figure 3.27: The IR absorption spectrum for the different vicinal I geometries under consideration with all hydrogen atoms replaced by deuterium atoms, calculated using the z-component of the dipole-moment derivatives only).

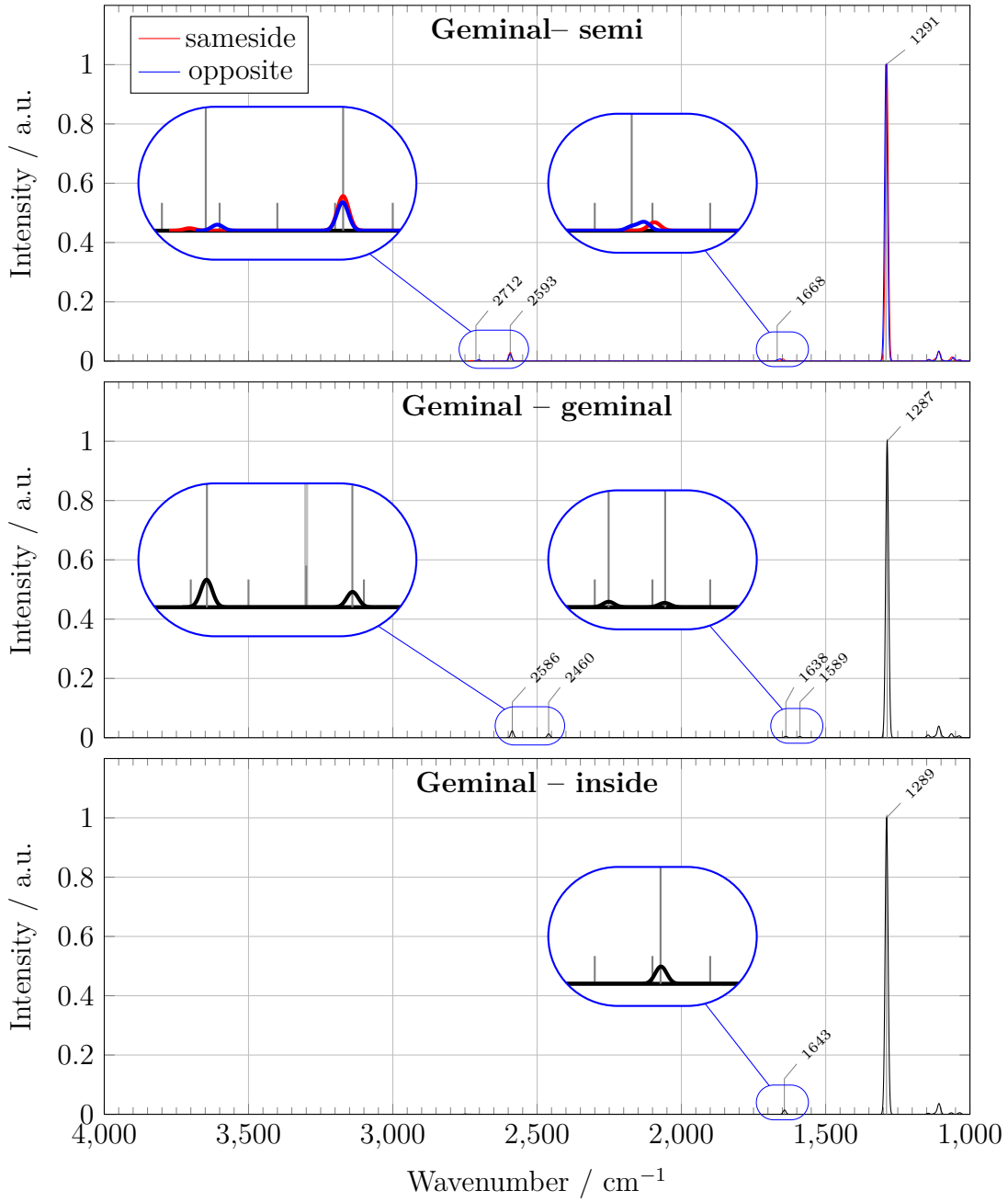

Figure 3.28: The IR absorption spectrum for the different geminal type defects under consideration with all hydrogen atoms replaced by deuterium atoms, calculated using the z-component of the dipole-moment derivatives only).

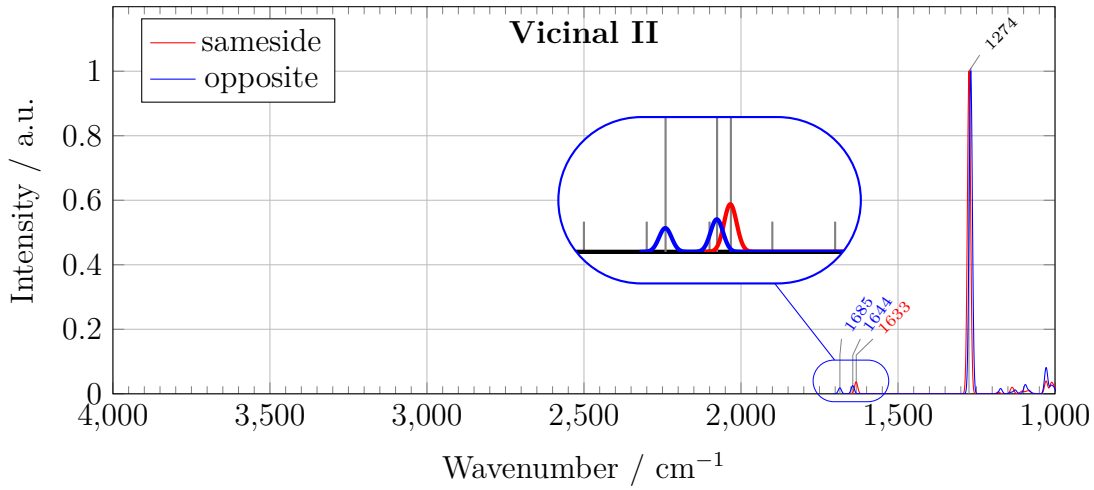

Figure 3.29: The IR absorption spectrum for the different Vicinal II geometries under consideration with all hydrogen atoms replaced by deuterium atoms, calculated using the z-component of the dipole-moment derivatives only).

An excellent correspondence between theoretical and experimental values is observed for the single H_2 – OH top structure (fig. 3.21 (a), OD: 2759 cm^{-1}, Si–D: 1625 cm^{-1}), rendering this the most promising structure. These results further corroborate the assumption, that it is the interlayer bonds that are compromised, while the six-membered rings remain largely intact. However, due to the fact that plasma species are known to be highly reactive, the presence of several different species is very likely.

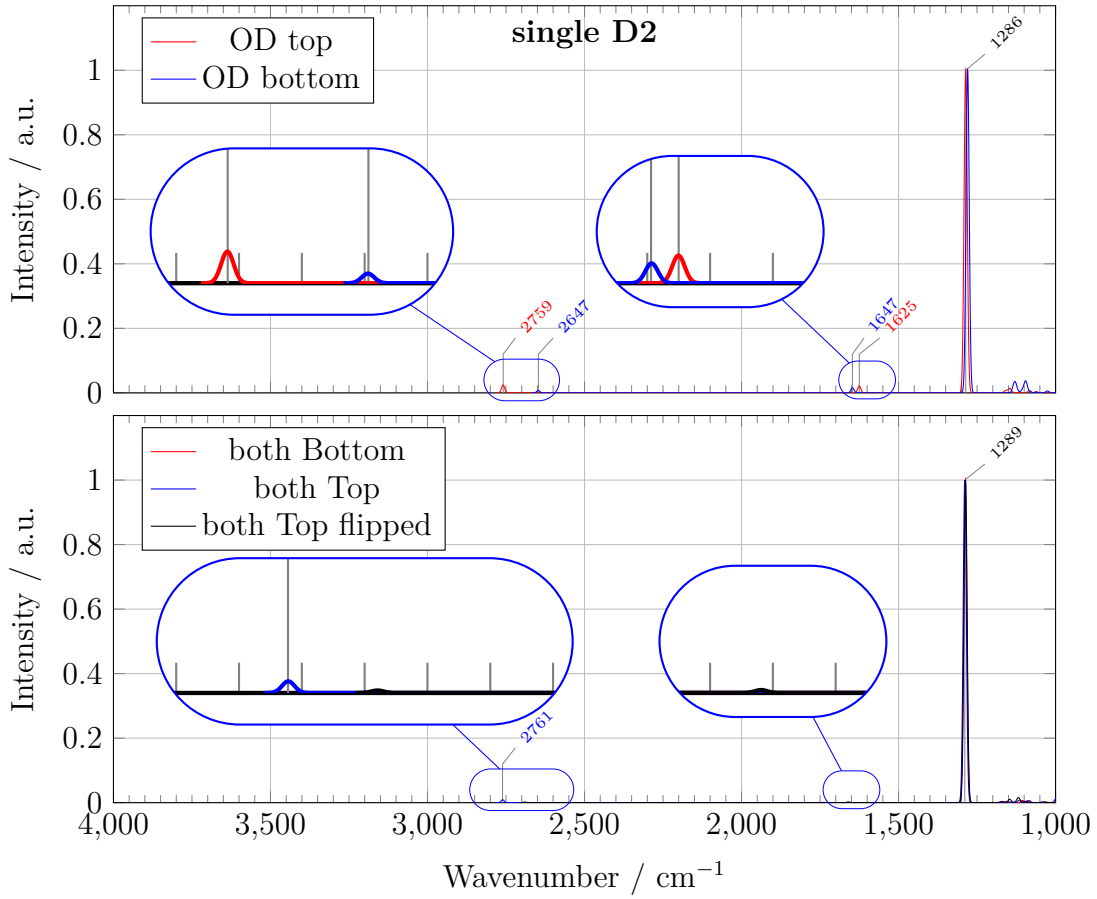

Figure 3.30: The IR absorption spectrum for the different bond-saturating single H_2 geometries under consideration with all hydrogen atoms replaced by deuterium atoms, calculated using the z-component of the dipole-moment derivative only).

	Structure	E_{rel} / eV
geminal	geminal	0.08
	inside	0.09
	opposite	0.07
	sameside	0.00
vicinal I	crossed 1	0.29
	crossed 2	0.38
	sameside 1	0.20
	sameside 2	0.13
	stacked 1	0.31
	stacked 2	0.36

(a) double H_2 defects.

	Structure	E_{rel} / eV
single H_2	OH top	0.09
	OH bottom	0.26
	both top	0.80
	both top flipped	0.00
	both bottom	0.32
vicinal II	sameside	1.14
	opposite	1.20

(b) single H_2 defects.

Table 3.3: Relative electronic energies for all structures under consideration with respect to the lowest energy structure found for each type.

3.2.6 Comparison of Electronic Energies

In order to eliminate further candidates, we analyzed the defect structures from an energetic point of view. To do so, we compare DFT total energies for all optimized defect structures considered.

Table 3.3 summarizes the relative electronic stability for both types of defects considered. For the double H_2 defects, the geminal type structures are energetically the most preferable. All of them lie within a 0.1 eV (2.3 kcal/mol) range with respect to our global minimum structure. The vicinal I structures are somewhat higher, which does not render them inaccessible, as kinetic hindrance may still prevent these structures from finding energetically lower configurations. Nonetheless, the energy difference for most of the vicinal II type structures is above the geminal type by about 0.3 eV (7 kcal/mol) or more.

As for the single H_2 defects, the energetically lowest structures are "OH top" and "both top – flipped". The "OH bottom" and "both bottom" structures are somewhat higher in energy. The "both-top" and especially the vicinal II type structures are substantially higher, which suggests that their presence is most unlikely.

These findings further corroborate the assumption that the single H_2 – OH top structure is the prevailing defect type upon plasma treatment of the silica bilayer.

3.2.7 Conclusions

In the previous sections, we have studied all considered defect structures in terms of XPS binding energy shifts, infrared absorption spectroscopy and electronic energies.

XPS BE shifts are (except for one outlier) uniformly negative and are in good alignment with the shifts observed in experiment. However, the non-systematic scattering of the values precludes the identification of any particular trial structure.

In terms of vibrational analysis, we discard the vicinal II and geminal – inside geometries, as the corresponding spectra lack the O–D band observed experimentally. Secondly, the double H_2 defect spectra are generally inconsistent with the experimental ones, as the latter do not manifest any splitting of the O–H (OD) or Si–H (SiD) bands, common in all remaining double H_2 type structures. Analysis of the single H_2 defect spectra reveals, that the only structure that agrees with the experimentally observed IR spectra qualitatively and quantitatively is the "single H_2 – OH top" geometry. The XPS shifts for this structure are also consistent with experiment. Finally, although this defect is not the global minium in terms of electronic energy, it is a mere 0.09 eV above the most stable configuration. The actual defect formation process depends on the potential energy surface landscape and the involved barriers more than on the final relative stability. Consequently, a slightly increased energy for this local minimum does not exclude the formation of these defects. From this analysis we conclude, that the most likely structure of the defect formed by H_2 attacking the silica bilayer is the "OH-top" of fig. 3.21a and that it is the registry between the two layers that is compromised.

3.3 Beyond DFT – Reaction Barriers on Non-Conducting Surfaces: Diffusion of Hydrogen on α-Al_2O_3(0001) as a Test Case

3.3.1 Introduction

Density functional theory, as suggested by Kohn and Sham, in conjunction with various flavors of exchange-correlation functionals provides a "quantum-chemist's toolbox" to model anything from a single atom, up to ten thousands of atoms, for example in DNA-chain sequencing or protein structure elucidation.[166,167] If one combines these tools with Bloch's theorem and possibly suitable pseudo-potentials to accurately represent localized parts of the wavefunction, they yield the same power for periodic systems. In the previous two chapters, we demonstrated that these tools can complement as well as extend experimental observations and yield reliable insights inaccessible by other means. The fact that in general, DFT approaches using GGA or even possibly higher-level approximations are superior to simple Hartree-Fock calculations, not only in their predictions but (at least for GGAs) also in their computational expenditure, meant that for the majority of time density functional theory was the only routinely applied methodology.[92,168]

Furthermore, the fact that a plane wave basis allows for a simple control of the quality by simply increasing the allowed number of plane waves and that they do not suffer from non-orthogonality meant that LCAO approaches, as they are the standard case in molecular calculations using atomic orbitals, were strongly underrepresented. While for a plane wave basis difficulties arise in representing localized parts of the wavefunction, these problems can efficiently be treated by the use of various types of pseudo-potentials. These are based on highly accurate free-atom calculations and are constructed in such a way, that within a sphere around each atom in the unit cell, the true effect of the wavefunction is replaced by a pseudo-potential term in the Hamiltonian which is inferred from the free-atom calculation.[72] The accuracy of these is sufficient for routinely carried out investigations[169] and consequently they are a standard tool in most quantum chemistry codes. While plane waves are inherently delocalized, atom-centered (Gaussian) basis sets are at the other end of the spectrum and can be considered the prototype of a chemically localized wavefunction. Naturally, their strength lies in representing wavefunctions that are similar to the free-atom states, while strongly

delocalized features are inherently more difficult. These require the addition of multiple low-exponent Gaussians in the expansion, so as to increase the flexibility of the basis set. This quickly leads to (near) linear dependencies which introduce numerical noise, becoming especially critical for metallic systems, for which a characteristic of the band structure is the similarity to the free electron-bands.[72]

So far, strong points were made in favor of DFT methods. However, a clear drawback of this approach is the fact, that the correct form of the correlation functional is unknown and as a result there is no strict hierarchy on how to approach the exact solution in a systematic way. In addition, standard GGAs suffer from the self-interaction-error as well as the resulting over-delocalization and are unable to describe dispersive London forces, which are especially important for extended systems.[170,171] These shortcomings can be mediated by employing the random phase approximation (RPA)[172] at the expense of increased computational cost, which renders it inapplicable to extended systems, or by addition of an empirical pairwise correction like the Grimme scheme.[89,90] This introduces empirical dependencies, which is clearly unfavorable in an *ab-initio* approach.

By contrast, both configuration interaction and coupled cluster exhibit natural ways on how to systematically lift the imposed approximations. For many electronic properties, the correlation contribution plays an important role, which in many cases cannot be captured accurately by standard exchange-correlation functionals.[173] However, the calculation of correlation energies using perturbative or CI approaches is more difficult, because the reference cell in principle interacts with an infinite number of images, which may lead to a slow convergence in the expression of the energy. Through the years, various approaches on how to implement efficient MP2 and coupled cluster schemes for extended periodic systems have been suggested.[174–181] However, the computational cost and the steep scaling of these methods with the system size limits them to applications with small cells.

A possible remedy of these problems is the construction of molecular clusters, i.e. small to medium sized discrete representations of the periodic structure. While it is able to leverage the well tested arsenal of molecular codes, clearly this approach suffers from the same scaling problems as do all molecular calculations and it may not be possible at all to reach a cluster size which can meaningfully mimic the true solid. In addition to that, metallic and ionic systems usually do not feature covalent bonds, which in case they have to be cut can be saturated using hydrogen atoms. As a result, the construction of clusters is not easy and in many cases not

possible at all. One of the successfully implemented variants of this approach is the so called incremental scheme by Stoll, where the occupied space is localized and the orbitals are grouped into local domains. The correlation energy is then represented in terms of a multipole expansion in these groups.[182–184] This scheme recovers the periodic limit, however the order of the many-body expansion can vary strongly and the desired accuracy may therefore not be reachable.[171]

An alternative is provided by high level – low level embedding, where a higher level of theory is applied to a subsystem embedded in the environment of the full system, which is treated at a lower level of theory. Examples are DFT-in-DFT embedding, where the two parts are evaluated using different exchange-correlation functionals or wavefunction-in-DFT embedding, where the environment is modeled at the DFT level of theory, while the subsystem is subjected to a wavefunction based treatment. Of course, one may employ wavefunction-in-wavefunction embedding, where the subsystem that is treated at the post-HF level of theory is embedded in the frozen HF coulomb and exchange field of the environment.[185–189]

One of the most effective techniques is to use the local approximation as introduced in section 2.4.5 and restrict the number of electron pairs that contribute to the correlation energy based on their spatial proximity. The parametrization in terms of spatial locality also enables us to go along the route of the so-called fragment embedding technique as introduced in section 2.6.3. This allows us to define a set of orbitals centered on a group of atoms as the "orbital-fragment", which is then treated at a higher level of theory, while being embedded in the frozen coulomb and exchange filed of the periodic HF solution. This becomes especially useful for ionic solids, since for these systems the valence states are localized on (for lone pairs) or between (for bonding pairs) atomic sites.

In a previous study by Heiden et al.,[44] investigating the performance of several plane-wave and atomic-orbital based exchange-correlation functionals including PW91, PBE (both GGAs), B3LYP and HES06 (both hybrid functionals) in comparison to the fully periodic local MP2 (LMP2) method, it was found that GGAs underestimate the reaction barrier as expected, while hybrid functionals were in much better agreement with the LMP2 results. Nonetheless, there was considerable scattering between the results and the question, which of these methods performs best, could not be decided. An accurate description of reaction barriers is especially important in the field of chemistry, as errors in energy barriers have dramatic influence on subsequently obtained kinetic parameters, as was

demonstrated in section 3.1. In order to reach the required accuracy, it is necessary to go beyond the currently employed methods and reach at least the coupled cluster singles and doubles with perturbative triples (CCSD(T)) level of theory in addition to a basis set of decent size.

In this section we aim at leveraging the embedded fragment approach at the CCSD(T) level of theory, the current "gold standard" in computational chemistry, together with fully periodic LMP2 calculations in conjunction with a hierarchical error correction protocol to obtain energy barriers for the diffusion of hydrogen on a α-$Al_2O_3(0001)$ surface below chemical accuracy of $1\,\frac{\text{kcal}}{\text{mol}}$. This enables us to provide a benchmark, both for the performance of typical DFT models which we compare to, as well as the accuracy of the periodic fragment approach by successively computing hierarchical error corrections to the periodic Hartree Fock barrier up to the CCSD(T) level of theory.

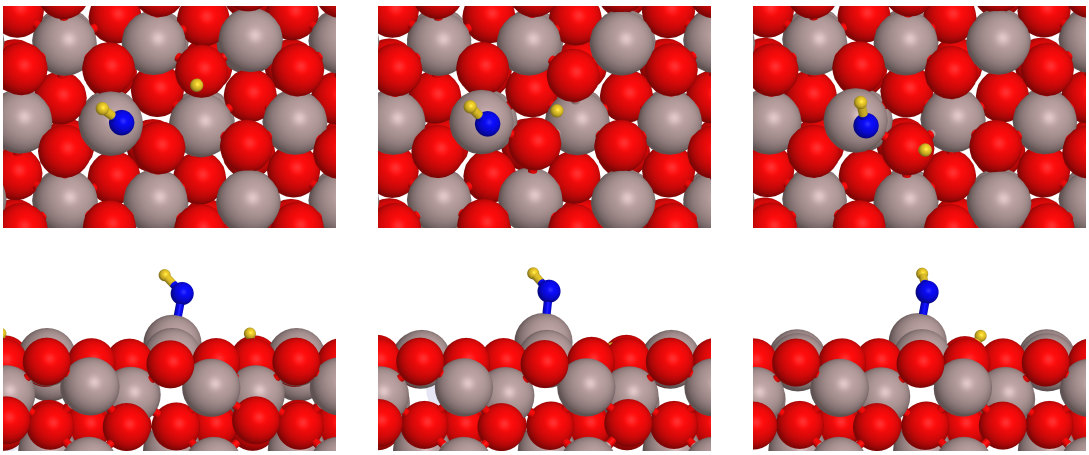

Figure 3.31: Top (top) and side view (bottom) of the 1–4 (left), transition state (middle) and 1–2 geometries (right). Oxygen, aluminum and hydrogen atoms are shown in red, gray and yellow, respectively. The oxygen atom originating from the dissociative adsorption of water is colored blue and reduced in size for distinction from the surface.

3.3.2 Structures

The system under consideration is the α-Al_2O_3(0001) surface, having one hydrogen and one hydroxyl group (OH) adsorbed per super-cell, resulting from the dissociative adsorption of one water molecule (corresponding to a 0.25 ML).

We adopt the nomenclature from references [44] and [190] for the two surface configurations of hydrogen sitting in the global minimum "1–2" position and in the energetically slightly increased "1–4" position (about 0.4 eV according to LMP2 and B3LYP+D3), corresponding to the initial and final state of an elementary diffusion step. The corresponding structure, together with the transition state (TS) separating these two states is depicted in fig. 3.31.

Our computational model consists of a nine-layer thick α-Al_2O_3 surface-slab terminated with a surface in the (0001) direction. Since we are employing atomic-orbital basis sets, we do not replicate the slab in the $\vec{z}$-direction, as is done in plane wave based calculations. The coordinates for the respective structures are taken from reference [44], where they were optimized at the B3LYP+D3 level within a 63 atom containing super cell.

At this point, it may be worth mentioning, that in this section we are not investigating any error contributions that stem from the slab-representation of the surface itself. For periodic systems, it is still currently a challenge to go beyond DFT methods for geometry optimizations and thermal properties. In addition,

DFT geometries and vibrational spectra are of reasonable quality, in particular for methods beyond the GGA approximation. Reaction barriers are usually described in terms of two single point calculations at the initial and transition state and thus when this barrier is captured with high accuracy, it provides a valuable reference for experiment. In addition, a high accuracy electronic barrier provides a benchmark for other methods such as DFT, irregardless of experimental application.

In the subsequent sections, we will first outline the various possible error sources and establish our correction scheme. We then investigate the various errors for the system at hand and subsequently apply the embedded fragment approach to reach the CCSD(T) level of theory.

	B3LYP+D3*	HF*	LMP2*	PW91**	PBE+D2**	HSE06**
$\Delta E^{\ddagger}$ / eV	0.69	1.17	0.60	0.42	0.44	0.56
$\Delta G^{\ddagger}$ / eV	0.58	1.06	0.49	0.27	0.29	0.41

Table 3.4: Summary of the electronic ($\Delta E^{\ddagger}$) and free energy ($\Delta G^{\ddagger}$, $T = 300\,\mathrm{K}$) barriers for the diffusion of hydrogen from the 1–2 position to the 1–4 position for various methods. A single asterisk (*) indicates an atomic orbitals basis, while a double asterisks (**) indicates a plane wave basis. Exact specifications of the basis together with the computational details are found in reference [44].

3.3.3 Employed Error Correction Scheme

3.3.3.1 Reference Values and Basis Set Specification

In order to provide context, table 3.4 summarizes the electronic ($\Delta E^{\ddagger}$) and free energy ($\Delta G^{\ddagger}$) barriers at $T = 300\,\mathrm{K}$ obtained with various methods and basis sets for the reaction discussed above as taken from ref. [44].

It becomes immediately apparent, that there is considerable scattering of the calculated free energy barrier among the methods. By far the largest outlier is (naturally) the HF method, but even when disregarding this, the predictions range from 0.27 eV (PW91) up to 0.58 eV (B3LYP+D3) with the LMP2 method sitting in the middle with a value of 0.49 eV. While it is likely that PBE notably underestimates the reaction barrier, it is not clear whether LMP2 or one of the hybrid-functionals (B3LYP/HSE06) performs better and if so, which one.

Since the zero-point energy and thermal contributions are largely the same for B3LYP+D3 ($-0.11\,\mathrm{eV}$) and PBE ($-0.15\,\mathrm{eV}$) we focus solely on the electronic part of the energy:

$$\Delta E \coloneqq \Delta E^{\ddagger}_{\mathrm{elec}} = E_{\mathrm{elec}}(\mathrm{TS}) - E_{\mathrm{elec}}(1\text{–}4) \qquad . \tag{3.9}$$

Our starting point is the fully periodic Hartree-Fock solution, employing atomic orbital (AO) basis sets, obtained using the Crystal code.[191] As mentioned above, molecular basis sets that are conventionally employed are problematic for periodic calculations since even slightly diffuse orbitals quickly cause near linear dependencies and as a result, the algorithm becomes numerically unstable. Consequently, for most calculations in this work we use a VTZ quality basis set which is optimized for periodic calculations. This basis set was already employed in reference [44] under the name AO3, while we refer to it as VTZ.

On the other hand, it is possible to improve the quality of the basis by placing additional functions on selected atoms only. Thus, one may use a hierarchical basis set treatment for a defined set of atoms. To this end, we employ the cc-pVTZ and cc-pVQZ basis sets of the Dunning family[192] for the three fragments defined below. These fragments only contain oxygen and hydrogen atoms, as the cc-pVXZ basis for aluminum contains very diffuse orbitals, which are not applicable in this context. In addition, since only AOs up to f-like functions are implemented in Cryscor at the moment, the oxygen g-like orbitals were removed for the cc-pVQZ basis. For all other atoms, the VTZ basis described above is used.

A further point that needs to be addressed is the fact, that accurate post-HF correlation calculations require high angular momentum diffuse orbitals to be part of the basis set. In order to include these, we make use of the so called dual basis set technique, i.e. we only include them for the post-HF treatment.[193] These will be referred to as (A)VTZ and (aug-)cc-pVXZ .[194] Within this technique, one can approximate the effect of the additional basis functions on the HF energy through the so called first-order singles:[193,195]

$$\delta^{\text{sing}} E_{\text{HF}} = \frac{2}{N_{\vec{k}}} \sum_{\vec{k}} \frac{\left| F_{ai}\left(\vec{k}\right) \right|^2}{\varepsilon_a(\vec{k}) - \varepsilon_i(\vec{k})} \quad , \tag{3.10}$$

where $N_{\vec{k}}$ is the number of $\vec{k}$-points within the first Brillouin zone, $\varepsilon_a(\vec{k})$ and $\varepsilon_i(\vec{k})$ are the occupied and virtual orbital energies and $F_{ai}(\vec{k})$ are the occupied-virtual elements of the Fock matrix. The latter do not all vanish due to the additional basis functions in the dual basis set technique that are added after HF converged.

We also employ the dual basis set technique to check for effects of the frozen core approximation by adding additional tight orbitals from the cc-pwCVTZ basis set on aluminum atoms (vide infra).[196]

3.3.3.2 Local MP2 method

Our post-HF treatment is based on the local MP2 level of theory (sections 2.4.4.2 and 2.4.5). Within our local ansatz, the occupied manifold is rerpesented using Wannier functions (WF) and the virutal manifold by projected atomic orbitals (PAOs). The pair list for the caluclation of the MP2 correlation energy eq. (2.106) is truncated according to the distance between i and j. The pair list is denoted $\mathbb{P}$ and for each pair $ij \in \mathbb{P}$ the list of virtual orbitals is denoted $[ij]$.

3.3.3.3 Frozen Core Approximation

For the calculation of correlation contributions, the frozen core approximation restricts the pair list $\mathbb{P}$ to occupied valence states only. It assumes, that any core contribution to the correlation energy will cancel in differences when computing for example reaction barriers. While in general, this is a very good approximation, the influence of the higher aluminum core levels may still contribute to the correlation in a non-negligible way. To check for the error contribution from the frozen core approximation, we compute the periodic LMP2 energies with and without the 2s2p core states of aluminum explicitly correlated:

$$\delta^{\text{core}} \Delta E_{\text{corr}}^{\text{LMP2}} = \Delta E_{\text{corr}}^{\text{LMP2}}\left(\text{FC}_{\text{1s}}\right) - \Delta E_{\text{corr}}^{\text{LMP2}}\left(\text{FC}\right) \qquad , \tag{3.11}$$

where FC denotes the frozen core and FC_{1s} that only the 1s core of oxygen and aluminum is frozen. For these calculations we employ the (C)VTZ and (AC)VTZ basis sets containing special tight orbitals from the cc-pwCTZ basis of aluminum atoms.

3.3.3.4 Local Pair and Domain Approximation

The next set of approximations considered are the so called local approximations, which include the restriction of the pair list $\mathbb{P}$ to spatially close pairs and the domain list for each pair $[ij]$ to virtual orbitals that are either close to i or j.

The local approximation is based on the fact, that the pair-energy contributions decay as R^{-6} with R being the distance of the two pair functions and that consequently the contributions decay relativley quickly with increasing distance. In molecular calculations, the pair list is restricted to increase computational efficiency, while in the limit of full pair lists, the true MP2 energy is retrieved. In periodic calculations, this cannot be achieved, even formally, since the pair list is infinite. Due to the rather quick convergence of the expansion with the pair distance, the sum still converges within reasonable limits. In order to investigate the error stemming from the truncation with the distance, we progressively expand the pair lists until convergence of $\Delta E_{\text{corr}}^{\text{LMP2}}$ is achieved.

For the representation of the virtual space we chose projected atomic orbitals (PAO), which are obtained by projecting out the occupied subspace from the atomic orbital basis. The minimal PAO domain is then the set of PAOs on a single atom for a lone pair or on two atoms for a bonding pair ij. In order to systematically

investigate the error correction from the domain approximation, we increase the domains from the minimal domains (iext=0) to the inclusion of nearest neighbor atoms (iext=1) and second nearest neighbor atoms (iext=2). For α-Al_2O_3, which is largely ionic in character, the valence WF are localized on oxygen atoms, thus the minimal PAO domains consist only of the PAOs located on oxygen atoms. The extended domains then additionally consist of the neighboring aluminum atoms (iext=1) and the next shell of oxygen atoms (iext=2).

While PAOs are attractive because a global virtual space is used to construct individual, compact pair domains, one of the drawbacks is the fact, that the domain regions can only be varied rather coarsely by either including all the PAOs on an atom or not. This may lead to discontinuities on the potential energy surface (PES) when the domain size changes. To compensate for this shortcoming, we use as a second set of virtual orbitals, the so called orbital specific virtuals (OSV).[197,198] These are defined for a given orbital i as the MP2 virtual natural orbitals for the diagonal pair ii. The OSV pair domain for an off-diagonal pair $ij \in \mathbb{P}$ is then the union for the orbitals $i \cup j$. OSVs have an intrinsic bias towards short-range correlation, which is counterbalanced by the addition of the most diffuse PAOs from the corresponding minimal PAO domain. The domain size for OSVs in Crystal is controlled via an energy threshold, which provides a convenient way of systematically improving the domain size. While OSVs suffer much less from the PES discontinuities that PAOs evoke, the energy cut-off is harder to tighten, as this also requires progressive expansion of the fitting basis. To elucidate the effects a choice of virtual basis has, we calculate the results using either appraoch and compare them to each other.

3.3.3.5 Density-fitting Approximation and Local Correlation Partitioning

The density fitting approximation for the decomposition of the two-electron four index integrals $\langle ij \,|\, kl \rangle$ was introduced in section 2.4.5. In this work we utilize the so called local robust density fitting,[199] which is known to be efficient for bulk systems in conjunction with Poisson type orbitals (PTO)[200,201] converted from a MP2 optimized Gaussian type orbital (GTO) fitting basis.[202]

While, as stated before, the density fitting approximation is in general a very accurate approximation, it is worthwhile verifying the extent to which it contributes to the error. To this end, we compared the deviation in $\Delta E_{\mathrm{corr}}^{\mathrm{LMP2}}$ for the fitting basis converted from the (aug-)cc-pVTZ and (aug-)cc-pV5Z GTO fitting basis. It

turns out, that the difference in the energy between these two fitting basis is below 1×10^{-5} eV, which corroborates the quality of the approximation. Since this value is far below any of the siginificant error contributions, we do not further discuss it here.

Next, we focus on the pair energies e_{ij} (eq. (2.65)), which, within the local approximation, can be partitioned into the three physically interpretable contributions stemming from the intra-fragment ($E_{\text{intra-frag}}$), extra-fragment ($E_{\text{extra-frag}}$) and inter-environment-fragment (E_{inter}) interactions:

$$E_{\text{corr}}^{\text{LMP2}} = E_{\text{intra-frag}} + E_{\text{extra-frag}} + E_{\text{inter}} \quad , \tag{3.12}$$

with

$$E_{\text{intra-frag}} = \sum_{\substack{i \in \text{frag} \\ j \in \text{frag}}} e_{ij} \tag{3.13}$$

$$E_{\text{extra-frag}} = \sum_{\substack{i \notin \text{frag} \\ j \notin \text{frag}}} e_{ij} \tag{3.14}$$

$$E_{\text{inter}} = \sum_{\substack{i \in \text{frag} \\ j \notin \text{frag}}} e_{ij} + \sum_{\substack{i \notin \text{frag} \\ j \in \text{frag}}} e_{ij} \quad . \tag{3.15}$$

One of the advantages of this partitioning is, that it is possible to apply different pair list restrictions to the different contributions and thus reduce the number of required terms, depending on their contributions.

3.3.3.6 Basis Set Convergence of the Correlation Energy

Since it is well known that the convergence of the correlation energy depends rather strongly on the size of the basis,[203] it is important to extrapolate the correlation contribution to the energy barrier instead of remaining at the (A)VTZ level. In order to do so, we estimate the convergence of our basis sets using two different techniques. Firstly, we use the standard inverse cubic extrapolation formula, based on the results obtained with the (aug-)cc-pVTZ and (aug-)cc-pVQZ functions positioned on the atoms belonging to the fragment.[41] This is carried out for both, the PAO and the OSV basis sets.

The additional basis functions are only placed on the oxygen and hydrogen atoms of the fragment, while the rest, including all aluminum atoms, remain at

the (A)VTZ level. However, since Al_2O_3 is to a large extent ionic and all valence Wannier functions (WF) are centered on oxygen atoms, we expect this to be sufficient.

Secondly, we use the explicitly correlated LMP2-F12 method to compare against, which is currently only implemented for PAOs.[65]

3.3.3.7 CCSD(T) Correction

Lastly, we focus on the LMP2 method error itself. In order to calculate the correction to the LMP2 energy barrier, we employ the embedded fragment approach as introduced in sections 2.6.3 and 3.3.1, together with the coupled cluster singles, doubles and perturbative triples (CCSD(T)) approach. We use three fragments of progressive size defined below, on which the localized orbitals (occupied and virtual) used for the post-HF calculation are centered. The periodic LMP2 solution is generated using Cryscor[51] and the resulting Hamiltonian matrix elements h_{pq}^{frag} and two electron integrals $\langle pq \,|\, rs \rangle$ are transferred to the molecular code Molpro[204] using the FCIDUMP interface.[205] The method error correction to the barrier is then calculated according to

$$\delta^{\text{CCSD(T)}} \Delta E = \Delta E^{\text{CCSD(T)}}_{\text{emb.frag.}} - \Delta E^{\text{LMP2}}_{\text{emb.frag.}} \quad . \tag{3.16}$$

En route, we also report the method corrections at the CCSD, DCSD[206] (distinguishable cluster with singles and doubles) and SCS-DCSD[207] (spin-component scaled DCSD) level of theory as they are available "for free" during the process.

3.3.3.8 Specification of the Fragments

The three fragments used for the basis set extrapolation and CCSD(T) error correction are shown in fig. 3.32. It should be noted, that the oxygen atoms on which the WFs belonging to the fragment are centered, are colored in blue. The minimal PAO domains then consist of the PAOs centered on the oxygen, hydrogen and one aluminum atom (marked in dark green) belonging to the fragment. For fragment 2 and the VTZ basis we use an additional extended PAO domain, which includes four additional aluminum atoms marked in light green.

A summary of the occupied and virtual spaces is shown in table 3.5. It should be noted, that the actual number of orthogonal virtual orbitals is slightly smaller than the number of PAO functions. The reason is that PAOs constitute a non-

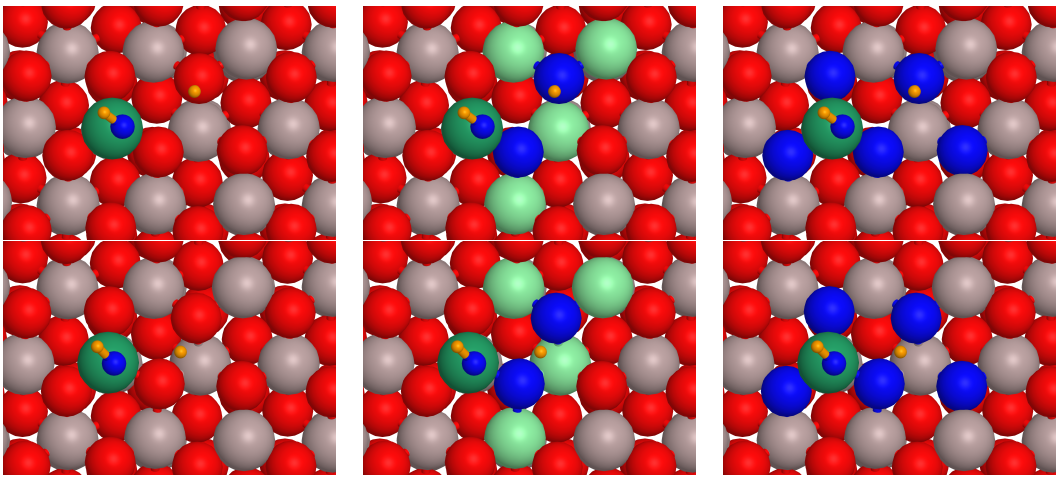

Figure 3.32: Top view of the surface with the oxygen atoms belonging to fragment 1 (left), fragment 2 (middle) and fragment 3 (right) colored in blue. The adsorbed oxygen (reduced in size) is also part of the cluster. The dark green aluminum atom is part of the minimal PAO domain, while the light green aluminum atoms are part of the extended virtual domains for fragment 2.
The top row shows the 1–4 position, while the bottom row depicts the transition state.

orthogonal and in general over-complete set, since there are by construction as many PAOs as AOs. Before the in-fragment canonicalization, the virtual manifold is orthogonalized and near-linear dependencies are removed based on the overlap threshold.

Fragment	1	2	2*	3
No. of occ. orbitals	4	12	12	24
No. of PAO atoms	4	6	10	9
VTZ				
No. of PAOs	97	157	313	247
No. of orthog. orbitals	94	151	301	236
(A)VTZ				
No. of PAOs	121	205		331
No. of orthog. virtuals	118	199		320

Table 3.5: Summary of the occupied and virtual spaces for the different fragments under consideration. Fragment 2* has an extended virtual space.

	ΔE_{HF}	$\delta^{\mathrm{sing}}\Delta E_{\mathrm{HF}}$	$\Delta E_{\mathrm{HF}} + \delta^{\mathrm{sing}}\Delta E_{\mathrm{HF}}$
(A)VTZ	1.166	-0.029	1.137
(aug-)cc-pVTZ			
Fragment 1	1.165	-0.025	1.140
Fragment 2	1.170	-0.037	1.133
Fragment 3	1.166	-0.029	1.137
(aug-)cc-pVQZ			
Fragment 1	1.166	-0.018	1.149
Fragment 2	1.161	-0.011	1.150
Fragment 3	1.156	-0.028	1.129

Table 3.6: Summary of the periodic Hartree-Fock energy barrier ΔE_{HF} obtained using different basis sets and fragment sizes. All values are given in eV.

3.3.4 Results and Discussion

Periodic HF Energies We begin the discussion of the various error contributions by discussing the periodic Hartree-Fock energies obtained using different basis sets. A summary is given in table 3.6. As mentioned in section 3.3.3.1, the contribution of the additional diffuse basis functions placed on the fragment atoms is evaluated after HF converged and is estimated via the singles corrections $\delta^{\mathrm{sing}}\Delta E_{\mathrm{HF}}$ (eq. (3.10)).

As is immediately obvious, the HF energy does not notably depend on the basis set size and the correction via the singles is always of the same magnitude, however there is non-systematic scattering of these values with an uncertainty of about 0.02 eV. Our best estimate for the HF energy is thus taken to be the one obtained using the (aug-)cc-pVQZ basis for fragment 3 (and (A)VTZ for the environment), amounting to $\Delta E_{\mathrm{HF}} = 1.13\,\mathrm{eV}$ with an uncertainty of about $\pm 0.02\,\mathrm{eV}$.

Correlation partitioning Next, we focus on the LMP2 correlation contribution to the energy barrier. As a first step, we examine the correlation partitioning according to eqs. (3.12) to (3.15) into intra-fragment, extra-fragment and inter-fragment-environment contributions. The obtained values are plotted in fig. 3.33 for the three fragments under consideration.

For fragment 1, there is virtually no change in the barrier, which suggests that the correlation contribution originating from the orbitals located at the OH group do not influence the diffusion barrier notably. However, for fragments 2 and 3, the dominant part almost entirely stems from intra-fragment contributions, suggesting that fragment 2 is already sufficiently large to model the overall description.

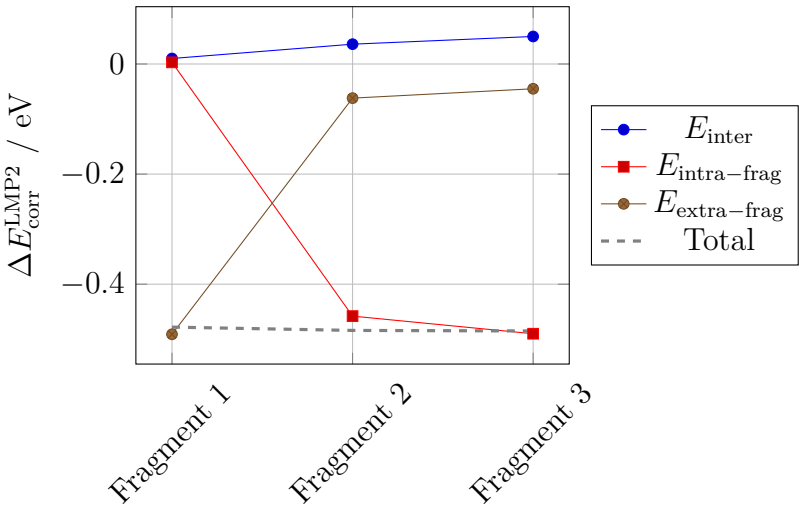

Figure 3.33: Partitioning of the LMP2(OSV)/(A)VTZ correlation energy contribution to the barrier into intra-fragment, extra-fragment and inter-fragment-environment contributions.

$R_{\text{max}}^{\text{intra-frag}}$	$R_{\text{max}}^{\text{extra-frag}}$	$R_{\text{max}}^{\text{inter}}$	$\Delta E_{\text{corr}}^{\text{LMP2}}$
6	2	2	-0.727
8	4	4	-0.541
10	6	6	-0.546
12	8	12	-0.547

Table 3.7: Influence of the cut-off radii for the pair lists on the LMP2(OSV)/(A)VTZ correlation energy contribution to the diffusion barrier. All radii are given in Å.

Pair List In a next step, we investigate the pair list truncation by successively increasing the cut-off radii for the allowed distance between two functions. The results are summarized in table 3.7.

It becomes apparent, that the correction to the barrier converges quickly and that the pair approximation will not introduce errors of considerable extent. Excluding the smallest cut-off, the energy only marginally fluctuates.

Domain List and Basis Set Extrapolation The next approximation to be investigated is the domain list approximation, which has the same origin as the basis set incompleteness error, as they are both restricting the virtual space. For this reason, we are treating them together.

At first glance, one can see from the compiled values in table 3.8, that the

	Fragment 1	Fragment 2	Fragment 3
$\Delta E_{\text{corr}}^{\text{LMP2}}$(PAO) / eV	-0.549	-0.536	-0.536
$\Delta E_{\text{corr}}^{\text{LMP2}}$(OSV) / eV	-0.555	-0.544	-0.542

Table 3.8: Basis set limit extrapolated values for $\Delta E_{\text{corr}}^{\text{LMP2}}$ computed using PAOs (iext=2) and OSVs using the (aug-)cc-pVTZ and (aug-)cc-pVQZ basis set for the fragment atoms. The rest of the atoms are modeled using the (A)VTZ quality basis.

extrapolated values for $\Delta E_{\text{corr}}^{\text{LMP2}}$ only depend very weakly on the fragment size on which the (aug-)cc-pVTZ and (aug-)cc-pVQZ functions are placed, especially in case of the OSV basis. On the other hand, the extrapolated values depend much stronger on the PAO domain size. Figure 3.34 plots the dependence of the computed correlation correction to the LMP2 barrier in dependence of the domain sizes together with the explicitly correlated LMP2-F12 and the extrapolated OSV results.

As becomes immediately obvious, the results depend strongly on the domain size and for fragments 1 and 2 also on the chosen method. For the largest domains all methods agree on the magnitude of the correction, indicating that large domains (iext=2) are required for a reliable description of the system. According to our findings, the reason for this is not the finite basis set, but rather an imbalance between the virtual spaces of the 1–4 and TS structure. This is corroborated by the fact that the basis set extrapolation correction on top of the (A)VTZ basis value is a mere 0.003 eV. Since the OSV approach is less prone to these issues, we use the OSV (aug-)cc-pV(TQ)Z extrapolated value as our reference MP2 value. Again, there is uncertainty between the different methods results of about 0.02 eV and our best estimate amounts to $\Delta E_{\text{corr}}^{\text{LMP2}} = -0.54\,\text{eV}$.

Frozen Core Next, we are concerned with the contribution resulting from the frozen core approximation. Table 3.9 summarizes the computed correction to the LMP2 energy barrier for the (C)VTZ and (AC)VTZ basis sets using PAOs and OSVs. As can be seen, the core correlation correction amounts to about 0.06 eV, regardless if PAOs or OSVs are used or which basis is employed. Considering the accuracy aimed for, this correction is non-negligible and indicates that for benchmarking barriers it needs to be considered in the methodology.

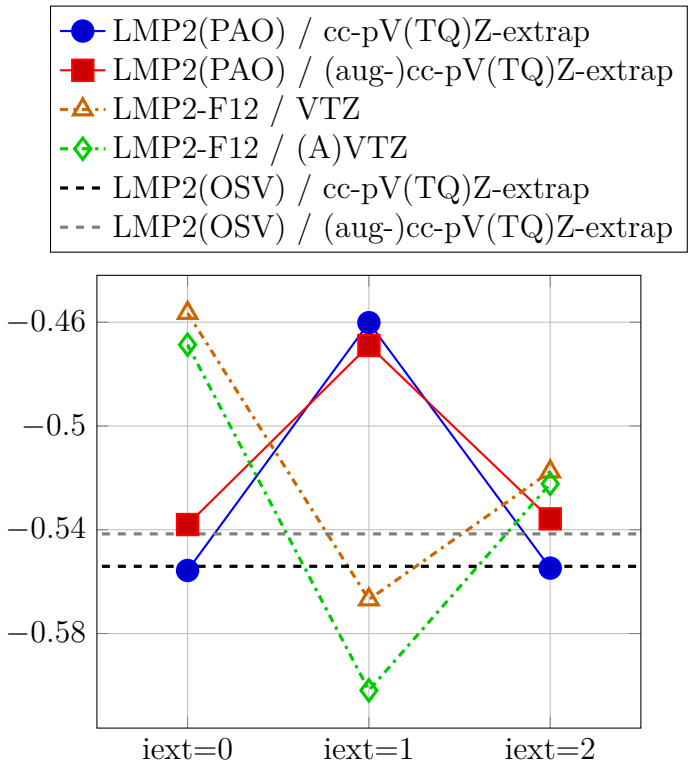

Figure 3.34: Basis set extrapolated values for $\Delta E_{\text{corr}}^{\text{LMP2}}$ obtained using the extended basis sets on the fragment atoms, as well as the explicitly correlated periodic LMP2-F12 method.

	PAO (iext=1)	PAO (iext=2)	OSV
(C)VTZ	0.058	0.059	0.063
(AC)VTZ	0.059		0.058

Table 3.9: The core correlation correction $\delta^{\text{core}}\Delta E_{\text{corr}}^{\text{LMP2}}$ computed using two different core correlation basis sets. All values are given in eV.

Method	Basis	Frag. 1	Frag. 2	Frag. 2*	Frag. 3
CCSD	VTZ	-0.002	0.140	0.141	0.150
	(A)VTZ	-0.002	0.143		0.155
DCSD	VTZ	-0.001	0.100	0.101	0.107
	(A)VTZ	-0.001	0.102		0.113
SCS-DCSD	VTZ	0.000	0.064	0.065	0.067
	(A)VTZ	0.000	0.066		0.073
CCSD(T)	VTZ	-0.001	0.072	0.071	0.073
	(A)VTZ	-0.001	0.072		0.073

Table 3.10: CCSD, DCSD, SCS-DCSD and CCSD(T) method correction to the $\Delta E_{\text{corr}}^{\text{LMP2}}$ barrier computed using the embedded fragment approach for the different fragments under consideration. All values given in eV. The asterisk on fragment 2^* indicates an extended virtual space.

LMP2 Method Error In the last step, we investigate the correction that stems from the LMP2 method error itself by employing the CCSD(T) embedded fragment method for the three fragments defined above. Table 3.10 summarizes the correction to the LMP2 barrier at the CCSD(T) level of theory, as well as the CCSD, DCSD and SCS-DCSD results. As a first observation, one may note that fragment 1 is obviously not large enough and cannot capture the additional correlation effects. For fragments 2 and 3 on the other hand, the obtained energies are consistent for both basis sets used. The CCSD method performs poorest, while the DCSD method, especially so for the spin-component scaled version, agrees very well with the CCSD(T) value of 0.07 eV. The CCSD(T) method correction to the LMP2 barrier is of the same sign as the frozen core correction as well as of comparable magnitude, rendering these the most substantial corrections in our scheme.

Summary Having examined all the relevant error sources that may contribute to our calculated diffusion barrier energy, we are now able to provide a benchmark value on the CCSD(T)-embedded fragment/periodic LMP2 level of theory with extrapolated basis set, correlated core correction, as well as converged pair and domain lists of $\Delta E^{\text{CCSD(T)}} = 0.72\,\text{eV}$. In table 3.11 we summarize our final results and compare them to the previously obtained DFT values using various flavors of exchange-correlation treatment.

The HF value is, as expected, much too large. The MP2 value, especially when adding the frozen core correction, is reasonably close to our final benchmark.

Method	ΔE / eV
HF	1.13
MP2(FC)	0.59
MP2	0.65
CCSD	0.81
DCSD	0.76
SCS-DCSD	0.72
CCSD(T)	0.72
B3LYP-D3	0.69
B3LYP	0.65
HSE06	0.42
PBE-D2	0.44

Table 3.11: Electronic energy barriers for the diffusion of hydrogen from the 1–4 position to the 1–2 position as described in Section 3.3.2 for various flavors of post-HF and DFT methods. The HF value corresponds to the periodic calculation with basis set extrapolated values to the (aug-)cc-pV(TQ)Z limit for fragment 3 and addition of the single correction. MP2(FC) denotes the periodic MP2 result with the 2s2p core correlation correction added. Further information is provided in the text.
DFT values are taken from reference [44].

Both the frozen core and CCSD(T) correction to the LMP2 method error are of the same sign and accumulate. GGA DFT methods noticeably underestimate the barrier as expected, while hybrid-functionals including portions of Hartree-Fock type exchange notably improve the results. The result for the B3LYP-D3 hybrid-functional is very close to our final CCSD(T) benchmark value.

3.3.5 Conclusion

This study had a twofold goal: On the one hand, we were able to supply a benchmark value for the diffusion of hydrogen on α-Al_2O_3(0001) for the step under consideration. We were able to demonstrate, that both the frozen core (especially so, when metal atoms are present) and the LMP2 method error contribute non-negligibly and accumulatively, reducing the LMP2 energy barrier by 0.14 eV.

The largest source of uncertainty remains from the basis set extrapolation, which could not be reduced below 0.02 eV, both for HF and MP2. Nonetheless, these errors do not exceed the goal of 1 $\frac{\text{kcal}}{\text{mol}}$. When comparing our benchmark result to values obtained via DFT calculations, it is apparent that the self-interaction and self-correlation error present in GGAs renders a value that is much too low. Hybrid functionals, in conjunction with empirical dispersion correction are largely able to correct for these errors, with B3LYP-D3 performing the best in this case. While we do not have any specific experimental reference to compare our results against, our results can actually be seen as a reference for experiment. Nevertheless, the fact that hydrogen atoms have been observed in the 1–4 position via means of IR spectroscopy, corroborates the fact that there exists a substantial barrier for the diffusion and hydrogen indeed remains sufficiently long at this site to be observed.[208]

On the other hand, we demonstrated a protocol for the systematic computation of high-accuracy correlated electronic energies for non-metallic, periodic systems. From our results, we expect the LMP2/(A)VTZ method to be of reasonable quality for the type of system investigated. The results obtained using OSV virtual spaces are much less prone to inconsistencies in the domains for different points on the potential energy surface than the ones obtained with PAOs. It is possible to calculate the basis set limit either using OSV-LMP2 based on the Dunning basis sets or via the periodic LMP2-F12 method. When using PAOs with the LMP2-F12 method, one should use very large domains (iext=2), or the results obtained may be unbalanced. When reaching for high accuracy, the CCSD(T) correction to the LMP2 energy is essential and can be calculated efficiently using an embedded fragment approach for a spatially localized part of the system, since then the correlation contribution from the environment is expected to cancel in energy differences.

The established hierarchical treatment offers a recipe for acquiring highly accurate electronic energies and energy barriers for non-metallic, periodic systems, an area of surface science that still lacks sufficiently capable methodologies.

4 Summary and Conclusions

The goal of this thesis was to obtain fundamental insights into the interaction of hydrogen with solid surfaces and materials. We developed the mathematical formalism required to obtain quantum mechanical insights extended to thermodynamic and kinetic properties of the system under consideration. While from a fundamental point of view:

> *"The underlying physical laws necessary for the mathematical theory of a large part of physics and the whole of chemistry are thus completely known, and the difficulty is only that the exact application of these laws leads to equations much too complicated to be soluble."*
>
> Paul Dirac,[209] 1929

As was demonstrated in this thesis, while this quote still being true, the development of numerical methods to efficiently solve approximations of various extent to the Schrödinger equation has enabled researchers to continuously penetrate deeper into the realm of purley *ab-initio* methods. With the Hartree-Fock algorithm (and subsequent post-HF methods) as well as density functional theory, two powerful workhorses have been established which can be adjusted in their complexity to fit the task at hand. Increasing computational power and more and more efficient implementations allow to successively lift imposed approximations and converge towards fully quantum-mechanical treatments. These tools can be used not only to complement experimental observations, but also to predict new materials and properties as well as to unravel information, which is not accessible by any other means.

The first topic, the formation of water from oxygen and hydrogen on a ruthenium surface, was investigated from a theoretical point of view using the DFT level of theory. The system was subjected to spatial confinement by deposition of a crystalline silica bilayer over the surface and detailed studies of the potential energy surface confirmed that the unconfined process is controlled by the kinetic

barrier posed by the addition of hydrogen and oxygen to form OH groups. Even though the chemistry itself is unchanged, the picture changes considerably upon confinement, as both hydrogen and water are hampered in their ability to reach and leave the surface. This opens the possibility of employing these ultra-thin films as molecular sieves, for example in gas purification. Ultra-thin silica films are versatile, as their synthesis is unproblematic and their chemical robustness allows them to be employed under physically demanding conditions. In addition, they lend themselves as prime candidates for experimental as well as theoretical studying. Our employed model successfully reproduces the experimental findings and it may further be applied to study similar systems. However, it should be noted that the employed methods, that is DFT at the GGA level in conjunction with the harmonic approximation and the Eyring equation to predict rate constants, are limited in their accuracy. Further improvement upon these points may yield even more insights that have escaped our treatment.

In general, the ability to control the chemical properties of surfaces by willfully introducing defects, as well as altering or introducing functional groups for further reactions is of tremendous importance. As the potential of the ultra-thin silica films for surface applications was already demonstrated in the first part, it will be of large interest to determine in which ways one can specifically design these films to fit specific purposes. One of the ways that was studied in this thesis is the exposure of the prepared film to hydrogen plasma. While itself being composed of highly reactive species, this approach does not require aggressive temperatures or chemicals and thus offers a way of introducing a controlled amount of defects without deteriorating the structure itself. Our research shows, that heterolytic splitting of silanol bonds via the addition of an activated hydrogen molecule leads to dispersed OH groups throughout the layer and a particular candidate structure as the most probable defect type was identified. We concluded that it is the inter-layer bonds between the two silica sheets that are the most susceptible to hydrogen addition and that the resulting hydroxyl group is located in the top layer. The hydroxylation of the bilayer paves the way for the toolbox of organic synthesis to further introduce desired groups and properties into the structure and therefore may yield new applications in chemistry, medicine and industrial environments. Additionally, the ability to study the system under highly controlled conditions renders it an excellent candidate for further model-system studies, both from an experimental as well as a theoretical point of view.

These two topics investigating the properties of the silica bilayer and its effect upon surface reactions nicely underline the power that is inherent when quantum mechanical methods are combined with experimental observations to interpret and predict new properties of materials and subsequent applications. The complexity of real-world applications requires the use of such model systems, however they inevitably also introduce limitations due to the differences to realistic systems. DFT has proven itself to be a reliable tool to investigate these tasks, however certain drawbacks, such as the fact that there is no clear hierarchical way of improving on the existing exchange-correlation functionals have to be taken into account.

In the last part, we examined the typical approximations that are made when modeling solid surfaces with quantum mechanical methods. As was outlined, the availability of high accuracy ab-intio methods is particularly demanded in the solid state community. By establishing a systematic error correction scheme and applying it to the example case of hydrogen diffusion on α-Al_2O_3, we were able to successively lift the imposed approximations up to the CCSD(T) level of theory and determine the magnitude of different contributions to the error. Our results show that the fully periodic local MP2 method using atomic orbitals now presents a viable alternative to DFT methods when it comes to modeling non-metallic surfaces. Additionally, we demonstrated that the embedded fragment approach is a powerful way of reaching even higher accuracy for periodic systems with localized features of interest, such as the diffusion of atoms and molecules on surfaces. As a result, we are able to supply a benchmark value of chemical accuracy quality, that may both be used to verify the precision of other methods such as DFT based approaches, as well as experimental findings.

I'd like to conclude this thesis by expressing my admiration for the many centuries of work that have gone and still go into the elucidation of scientific principles. None of the great theories that govern what we understand to be physics today would have been possible without long and laborious research of many great minds, including many hours which did not lead to any conclusions whatsoever. Of course, the same holds for any natural science discipline.

List of Figures

List of Tables

References

(1) Lindberg, D. C., *The beginnings of Western science: The European scientific tradition in philosophical, religious, and institutional context, prehistory to AD 1450*; University of Chicago Press: Chicago, 2010.

(2) Gershoni, H. E. I., *The Nile: histories, cultures, myths*; Lynne Rienner Publishers: 2000.

(3) Popper, K., *Conjectures and refutations: The growth of scientific knowledge*; Routledge and Kegan Paul: London, UK, 1963.

(4) Thony, C. Calendrical confusion or just when did Newton die? `https://thonyc.wordpress.com/2015/03/20/calendrical-confusion-or-just-when-did-newton-die/` (accessed 01/04/2022).

(5) Needham, J., *Science and Civilisation in China: Volume 3, Mathematics and the Sciences of the Heavens and the Earth*; Science and Civilisation in China; Cambridge University Press: 1959.

(6) Zilsel, E. The Sociological Roots of Science. *Am. J. Soc.* **1942**, *47*, 544–562.

(7) Sanford, V. La Disme of Simon Stevin – The First Book on Decimals. *The Mathematics Teacher MT* **1921**, *14*, 321–333.

(8) Gaßner, J. M.; Müller, J., *Können wir die Welt verstehen? - Meilensteine der Physik von Aristoteles zur Stringtheorie*; S. Fischer Verlag: Berlin, 2019.

(9) Bennett, G. W. et al. Measurement of the Negative Muon Anomalous Magnetic Moment to 0.7 ppm. *Phys. Rev. Lett.* **2004**, *92*, 161802.

(10) Carr, B. J.; Giddings, S. B. Quantum Black Holes. *Sci. Am.* **2005**, *292*, 48–55.

(11) Grommet, A. B.; Feller, M.; Klajn, R. Chemical reactivity under nanoconfinement. *Nature Nano.* **2020**, *15*, 256–271.

(12) Somorjai, G. A. The Evolution of Surface Chemistry. A Personal View of Building the Future on Past and Present Accomplishments. *J. Phys. Chem. B* **2002**, *106*, 9201–9213.

(13) Duke, C. B. The birth and evolution of surface science: Child of the union of science and technology. *Proc. Natl. Acad. Sci. U.S.A.* **2003**, *100*, 3858–3864.

(14) Somorjai, G. A. Modern Surface Science and Surface Technologies: An Introduction. *Chem. Rev.* **1996**, *96*, 1223–1236.

(15) Binder, K., *Monte Carlo simulation in statistical physics: an introduction*; Springer-Verlag: Heidelberg New York, 2010.

(16) Stampfl, C.; Veronica Ganduglia-Pirovano, M.; Reuter, K.; Scheffler, M. Catalysis and corrosion: the theoretical surface-science context. *Surf. Sci.* **2002**, *500*, 368–394.

(17) Aharonov, D.; Vazirani, U. In *Computability: Turing, Gödel, Church, and Beyond*; MIT Press: 2013.

(18) Crispino, L.; Kennefick, D. A hundred years of the first experimental test of general relativity. *Nature Phys.* **2019**, *15*, 416–419.

(19) Bagrov, V. G.; Gitman, D., *The Dirac Equation and its Solutions*; De Gruyter: 2014.

(20) Grosse, H.; Martin, A. J., *Particle physics and the Schrödinger equation*; Cambridge Univ. Press: 1997.

(21) Holland, P. A quantum of history. *Contemp. Phys.* **2011**, *52*, 355–358.

(22) Landau, L. D.; Lifschitz, E. M., *Lehrbuch der theoretischen Physik - in 10 Bänden. Quantenmechanik 4*; Akademie-Verlag Berlin: 1979.

(23) Sen, D. The uncertainty relations in quantum mechanics. *Curr. Sci.* **2014**, *107*, 203–218.

(24) Szabo, A.; Ostlund, N. S., *Modern Quantum Chemistry: Introduction to Advanced Electronic Structure Theory*; Dover Publications, Inc.: Mineola, 1996.

(25) Shull, H.; Hall, G. G. Atomic Units. *Nature* **1959**, *184*, 1559–1560.

(26) Gerlach, W.; Stern, O. Über die Richtungsquantelung im Magnetfeld. *Ann. Phys.* **1924**, *379*, 673–699.

(27) Pauli, W. Über den Zusammenhang des Abschlusses der Elektronengruppen im Atom mit der Komplexstruktur der Spektren. *Z. Phys.* **1925**, *31*, 765–783.

(28) Altunbulak, M.; Klyachko, A. The Pauli Principle Revisited. *Commun. in Math. Phys.* **2008**, *282*, 287–322.

(29) Combes, J. M.; Duclos, P.; Seiler, R. In *Rigorous Atomic and Moloecular Physics*, Velo, G., Wightman, A. S., Eds.; Springer US: Boston, MA, 1981, pp 185–213.

(30) Hartree, D. R. The Wave Mechanics of an Atom with a Non-Coulomb Central Field. Part II. Some Results and Discussion. *Math. Proc. Camb. Philos. Soc.* **1928**, *24*, 111–132.

(31) Fock, V. Näherungsmethode zur Lösung des quantenmechanischen Mehrkörperproblems. *Z. Phys.* **1930**, *61*, 126–148.

(32) Rosenbrock, H. H. A variational principle for quantum mechanics. *Phys. Lett. A* **1985**, *110*, 343–346.

(33) Slater, J. C. The Theory of Complex Spectra. *Phys. Rev.* **1929**, *34*, 1293–1322.

(34) Condon, E. U. The Theory of Complex Spectra. *Phys. Rev.* **1930**, *36*, 1121–1133.

(35) Löwdin, P.-O. Quantum Theory of Many-Particle Systems. III. Extension of the Hartree-Fock Scheme to Include Degenerate Systems and Correlation Effects. *Phys. Rev.* **1955**, *97*, 1509–1520.

(36) Boyd, R. J.; Coulson, C. A. The Fermi hole in atoms. *J Phys. B: Atomic and Mol. Phys.* **1974**, *7*, 1805–1816.

(37) Hepburn, J.; Scoles, G.; Penco, R. A simple but reliable method for the prediction of intermolecular potentials. *Chem. Phys. Lett.* **1975**, *36*, 451–456.

(38) Gill, P. M. W.; Johnson, B. G.; Pople, J. A. Two-electron repulsion integrals over Gaussians functions. *Int. J. Quantum Chem.* **1991**, *40*, 745–752.

(39) Roothaan, C. C. J. New Developments in Molecular Orbital Theory. *Rev. Mod. Phys.* **1951**, *23*, 69–89.

(40) Hall, G. G.; Lennard-Jones, J. E. The molecular orbital theory of chemical valency VIII. A method of calculating ionization potentials. *Proc. Math. Phys. Eng. Sci.* **1951**, *205*, 541–552.

(41) Helgaker, T.; Jorgensen, P.; Olsen, J., *Molecular electronic-structure theory*; John Wiley & Sons: Chichester, England, 2000.

(42) Kvasnička, V.; Laurinc, V.; Biskupič, S. Wigner's (2n+1) rule in MBPT. *Mol. Phys.* **1980**, *39*, 143–161.

(43) Ab Initio Methods for Electron Correlation in Molecules, Vol. 3, Modern Methods and Algorithms of Quantum Chemistry - Proceedings, Vol. 3, John von Neumann Institute for Computing: 2000, pp 97–179.

(44) Heiden, S.; Usvyat, D.; Saalfrank, P. Theoretical Surface Science Beyond Gradient-Corrected Density Functional Theory: Water at α-Al_2O_3(0001) as a Case Study. *J. Phys. Chem. C* **2019**, *123*, 6675–6684.

(45) Leininger, M. L.; Allen, W. D.; Schaefer, H. F.; Sherrill, C. D. Is Møller–Plesset perturbation theory a convergent ab initio method? *J. Chem. Phys.* **2000**, *112*, 9213–9222.

(46) Zalesny, R.; Papadopoulos, M.; Mezey, P.; Leszczynski, J., *Linear-Scaling Techniques in Computational Chemistry and Physics: Methods and Applications*, 2011.

(47) Pulay, P. Localizability of dynamic electron correlation. *Chem. Phys. Lett.* **1983**, *100*, 151–154.

(48) Pipek, J.; Mezey, P. G. A fast intrinsic localization procedure applicable for ab initio and semiempirical linear combination of atomic orbital wave functions. *J. Chem. Phys.* **1989**, *90*, 4916–4926.

(49) Foster, J. M.; Boys, S. F. Canonical Configurational Interaction Procedure. *Rev. Mod. Phys.* **1960**, *32*, 300–302.

(50) Werner, H.-J.; Pflüger, K. In *Annual Reports in Computational Chemistry*; Annual Reports in Computational Chemistry, Vol. 2; Elsevier: 2006, pp 53–80.

(51) Usvyat, D.; Maschio, L.; Pisani, C.; Schütz, M. In *Progress in Physical Chemistry Volume 3: Modern and Universal First-principles Methods for Many-electron Systems in Chemistry and Physics*, Dolg, F. M., Ed.; Oldenbourg Wissenschaftsverlag: 2011, pp 151–164.

(52) Kurashige, Y.; Yang, J.; Chan, G. K.-L.; Manby, F. R. Optimization of orbital-specific virtuals in local Møller-Plesset perturbation theory. *J. Chem. Phys.* **2012**, *136*, 124106.

(53) Whitten, J. L. Coulombic potential energy integrals and approximations. *J. Chem. Phys.* **1973**, *58*, 4496–4501.

(54) Dunlap, B. I.; Connolly, J. W. D.; Sabin, J. R. On first-row diatomic molecules and local density models. *J. Chem. Phys.* **1979**, *71*, 4993–4999.

(55) Vahtras, O.; Almlöf, J.; Feyereisen, M. Integral approximations for LCAO-SCF calculations. *Chem. Phys. Lett.* **1993**, *213*, 514–518.

(56) Skylaris, C.-K.; Gagliardi, L.; Handy, N.; Ioannou, A.; Spencer, S.; Willetts, A. On the resolution of identity Coulomb energy approximation in density functional theory. *J. Mol. Strut.* **2000**, *501-502*, 229–239.

(57) Eichkorn, K.; Treutler, O.; Öhm, H.; Häser, M.; Ahlrichs, R. Auxiliary basis sets to approximate Coulomb potentials. *Chem. Phys. Lett.* **1995**, *242*, 652–660.

(58) Weigend, F. Accurate Coulomb-fitting basis sets for H to Rn. *Phys. Chem. Chem. Phys.* **2006**, *8*, 1057–1065.

(59) Werner, H.-J.; Manby, F. R.; Knowles, P. J. Fast linear scaling second-order Møller-Plesset perturbation theory (MP2) using local and density fitting approximations. *J. Chem. Phys.* **2003**, *118*, 8149–8160.

(60) Reine, S.; Tellgren, E.; Krapp, A.; Kjærgaard, T.; Helgaker, T.; Jansik, B.; Høst, S.; Salek, P. Variational and robust density fitting of four-center two-electron integrals in local metrics. *J. Chem. Phys.* **2008**, *129*, 104101.

(61) Milko, M.; Noga, J.; Varga, Š. Accuracy of density fitting in calculation of two-electron repulsion integrals in periodic systems. *Int. J. Quantum. Chem.* **2007**, *107*, 2158–2168.

(62) Schütz, M.; Werner, H.-J. Local perturbative triples correction (T) with linear cost scaling. *Chem. Phys. Lett.* **2000**, *318*, 370–378.

(63) Schütz, M.; Hetzer, G.; Werner, H.-J. Low-order scaling local electron correlation methods. I. Linear scaling local MP2. *J. Chem. Phys.* **1999**, *111*, 5691–5705.

(64) Menezes, F.; Kats, D.; Werner, H.-J. Local complete active space second-order perturbation theory using pair natural orbitals (PNO-CASPT2). *J. Chem. Phys.* **2016**, *145*, 124115.

(65) Ma, Q.; Werner, H.-J. Scalable Electron Correlation Methods. 2. Parallel PNO-LMP2-F12 with Near Linear Scaling in the Molecular Size. *J. Chem. Theory Comput.* **2015**, *11*, 5291–5304.

(66) Krause, C.; Werner, H.-J. Comparison of explicitly correlated local coupled-cluster methods with various choices of virtual orbitals. *Phys. Chem. Chem. Phys.* **2012**, *14*, 7591–7604.

(67) Thomas, L. H. The calculation of atomic fields. *Math. Proc. Camb. Philos. Soc.* **1927**, *23*, 542–548.

(68) Eschrig, H., *The fundamentals of density functional theory*; Edition am Gutenbergplatz: Leipzig, 2003.

(69) Hohenberg, P.; Kohn, W. Inhomogeneous Electron Gas. *Phys. Rev.* **1964**, *136*, B864–B871.

(70) Levy, M. Universal variational functionals of electron densities, first-order density matrices, and natural spin-orbitals and solution of the v-representability problem. *Proc. Natl. Acad. Sci. U.S.A.* **1979**, *76*, 6062–6065.

(71) Kohn, W.; Sham, L. Self-Consistent Equations Including Exchange and Correlation Effects. *Phys. Rev.* **1965**, *140*, A1133–A1138.

(72) Harrison, W., *Solid State Theory*; Dover Books on Physics; Dover Publications: 1980.

(73) Jones, R. O.; Gunnarsson, O. The density functional formalism, its applications and prospects. *Rev. Mod. Phys.* **1989**, *61*, 689–746.

(74) Mardirossian, N.; Head-Gordon, M. Thirty years of density functional theory in computational chemistry: an overview and extensive assessment of 200 density functionals. *Mol. Phys.* **2017**, *115*, 2315–2372.

(75) Cohen, A. J.; Handy, N. C. Assessment of exchange correlation functionals. *Chem. Phys. Lett.* **2000**, *316*, 160–166.

(76) Scuseria, G. E.; Staroverov, V. N. In *Theory and Applications of Computational Chemistry*, Dykstra, C. E., Frenking, G., Kim, K. S., Scuseria, G. E., Eds.; Elsevier: Amsterdam, 2005, pp 669–724.

(77) Putz, M. V. Density Functionals of Chemical Bonding. *Int. J. Mol. Sci.* **2008**, *9*, 1050–1095.

(78) Perdew, J.; Burke, K.; Ernzerhof, M. Generalized Gradient Approximation Made Simple. *Phys. Rev. Lett.* **1996**, *77*, 3865–3868.

(79) Perdew, J. P.; Yue, W. Accurate and simple density functional for the electronic exchange energy: Generalized gradient approximation. *Phys. Rev. B* **1986**, *33*, 8800–8802.

(80) Burke, K.; Perdew, J. P.; Ernzerhof, M. Why the generalized gradient approximation works and how to go beyond it. *Int. J. Quantum Chem.* **1997**, *61*, 287–293.

(81) Boese, A. D.; Doltsinis, N. L.; Handy, N. C.; Sprik, M. New generalized gradient approximation functionals. *J. Chem. Phys.* **2000**, *112*, 1670–1678.

(82) Bao, J. L.; Gagliardi, L.; Truhlar, D. G. Self-Interaction Error in Density Functional Theory: An Appraisal. *J. Phy. Chem. Lett.* **2018**, *9*, 2353–2358.

(83) Maier, T. M.; Arbuznikov, A. V.; Kaupp, M. Local hybrid functionals: Theory, implementation, and performance of an emerging new tool in quantum chemistry and beyond. *WIREs Comput. Mol. Sci.* **2018**, *9*, 1378.

(84) Corà, F.; Alfredsson, M.; Mallia, G.; Middlemiss, D. S.; Mackrodt, W. C.; Dovesi, R.; Orlando, R. In *Principles and Applications of Density Functional Theory in Inorg. Chem. II*; Springer Berlin Heidelberg: Berlin, Heidelberg, 2004, pp 171–232.

(85) Goerigk, L.; Grimme, S. Double-hybrid density functionals. *WIREs Comput. Mol. Sci.* **2014**, *4*, 576–600.

(86) Martin, J. M. L.; Santra, G. Empirical Double-Hybrid Density Functional Theory: A 'Third Way' in Between WFT and DFT. *Isr. j. Chem.* **2020**, *60*, 787–804.

(87) Baer, R.; Livshits, E.; Salzner, U. Tuned Range-Separated Hybrids in Density Functional Theory. *Annu. Rev. Phys. Chem.* **2010**, *61*, 85–109.

(88) Henderson, T. M.; Janesko, B. G.; Scuseria, G. E. Range Separation and Local Hybridization in Density Functional Theory. *J. Phys. Chem. A* **2008**, *112*, 12530–12542.

(89) Grimme, S.; Antony, J.; Ehrlich, S.; Krieg, H. A consistent and accurate ab initio parametrization of density functional dispersion correction (DFT-D) for the 94 elements H-Pu. *J. Chem. Phys.* **2010**, *132*, 154104.

(90) Tkatchenko, A.; Scheffler, M. Accurate Molecular Van Der Waals Interactions from Ground-State Electron Density and Free-Atom Reference Data. *Phys. Rev. Lett.* **2009**, *102*, 073005.

(91) Lin, I.-C.; Seitsonen, A. P.; Tavernelli, I.; Rothlisberger, U. Structure and Dynamics of Liquid Water from ab Initio Molecular Dynamics—Comparison of BLYP, PBE, and revPBE Density Functionals with and without van der Waals Corrections. *J. Chem. Theory Comput.* **2012**, *8*, 3902–3910.

(92) Medvedev, M. G.; Bushmarinov, I. S.; Sun, J.; Perdew, J. P.; Lyssenko, K. A. Density functional theory is straying from the path toward the exact functional. *Science* **2017**, *355*, 49–52.

(93) Bloch, F. Über die Quantenmechanik der Elektronen in Kristallgittern. *Z. Phys.* **1929**, *52*, 555–600.

(94) Casassa, S.; Halo, M.; Maschio, L.; Roetti, C.; Pisani, C. Beyond a Hartree–Fock description of crystalline solids: the case of lithium hydride. *Theor. Chem. Acc.* **2007**, *117*, 781–791.

(95) Christlmaier, E. M.; Kats, D.; Alavi, A.; Usvyat, D. Full Configuration Interaction Quantum Monte Carlo treatment of fragments embedded in a periodic mean field (submitted). *J. Chem. Phys.* **2022**.

(96) Cheng, K. C. Historical Development of the Theory of Heat and Thermodynamics: Review and Some Observations. *Heat Transf. Eng.* **1992**, *13*, 19–37.

(97) Clausius, R. I. On the moving force of heat, and the laws regarding the nature of heat itself which are deducible therefrom. *Lond. Edinb. Dublin Philos. Mag. J. Sci.* **1851**, *2*, 1–21.

(98) Gibbs, J. W. A method of geometrical representation of the thermodynamic properties by means of surfaces. *Trans. Conn. Acad.* **1873**, 382–404.

(99) Sharp, K.; Matschinsky, F. Translation of Ludwig Boltzmann's Paper "On the Relationship between the Second Fundamental Theorem of the Mechanical Theory of Heat and Probability Calculations Regarding the Conditions for Thermal Equilibrium" Sitzungberichte der Kaiserlichen Akademie der Wissenschaften. Mathematisch-Naturwissen Classe. Abt. II, LXXVI 1877, pp 373-435 (Wien. Ber. 1877, 76:373-435). Reprinted in Wiss. Abhandlungen, Vol. II, reprint 42, p. 164-223, Barth, Leipzig, 1909. *Entropy* **2015**, *17*, 1971–2009.

(100) Wedler, G.; Freund, H., *Lehrbuch der physikalischen Chemie*; Wiley VCH Lehrbuchkollektion 1; Wiley-VCH: 2012.

(101) Chorkendorff, I.; Niemantsverdriet, J. W. In *Concepts of Modern Catalysis and Kinetics*; John Wiley & Sons, Ltd: 2003.

(102) Koopmans, T. Über die Zuordnung von Wellenfunktionen und Eigenwerten zu den Einzelnen Elektronen Eines Atoms. *Physica* **1934**, *1*, 104–113.

(103) Tardio, S.; Cumpson, P. J. Practical estimation of XPS binding energies using widely available quantum chemistry software. *Surf. Interface Anal.* **2018**, *50*, 5–12.

(104) Salmeróna, M.; Gale, R. J.; Somorjai, G. A. A modulated molecular beam study of the mechanism of the H_2–D_2 exchange reaction on Pt(111) and Pt(332) crystal surfaces. *J. Chem. Phys.* **1979**, *70*, 2807–2818.

(105) Robertson, A. J. B. The Early History of Catalysis. *Platin. Met. Rev.* **1975**, *19*, 64–69.

(106) Von Lothar, D. Das Portrait: Wilhelm Ostwald (1853-1932). *Chemie Unserer Zeit* **1982**, *16*, 186–196.

(107) Roskoski, R. In *Reference Module in Biomedical Sciences*; Elsevier: 2015.

(108) Bligaard, T.; Bullock, R. M.; Campbell, C. T.; Chen, J. G.; Gates, B. C.; Gorte, R. J.; Jones, C. W.; Jones, W. D.; Kitchin, J. R.; Scott, S. L. Toward Benchmarking in Catalysis Science: Best Practices, Challenges, and Opportunities. *ACS Catal.* **2016**, *6*, 2590–2602.

(109) Ertl, G.; Freund, H.-J. Catalysis and Surface Science. *Physics Today* **1999**, *52*, 32–38.

(110) Humphreys, J.; Lan, R.; Tao, S. Development and Recent Progress on Ammonia Synthesis Catalysts for Haber–Bosch Process. *Advanced Energy and Sustainability Research* **2021**, *2*, 2000043.

(111) Jiou, J.; Chiravuri, K.; Gudapati, A.; J. Gassensmith, J. The Chemistry of Confined Spaces. *Curr. Org. Chem.* **2014**, *18*, 2002–2009.

(112) Rouhi, A. M. BOXED IN: CHEMISTRY IN CONFINED SPACES. *Chem. Eng. News* **2000**, *78*, 40–47.

(113) Dhakshinamoorthy, A.; Asiri, A. M.; Garcia, H. Catalysis in Confined Spaces of Metal Organic Frameworks. *ChemCatChem* **2020**, *12*, 4732–4753.

(114) Fu, Q.; Bao, X. Surface chemistry and catalysis confined under two-dimensional materials. *Chem. Soc. Rev.* **2017**, *46*, 1842–1874.

(115) Boscoboinik, J. A. Chemistry in confined space through the eyes of surface science—2D porous materials. *J. Phys. Condens. Matt.* **2018**, *31*, 063001.

(116) Gardeniers, H. J. G. E. Chemistry in nanochannel confinement. *Anal. Bioanal. Chem.* **2009**, *394*, 385–397.

(117) Goettmann, F.; Sanchez, C. How does confinement affect the catalytic activity of mesoporous materials? *J. Mat. Chem.* **2007**, *17*, 24–30.

(118) Luisi, P. L.; Straub, B., *Reverse micelles: biological and technological relevance of amphiphilic structures in apolar media*; Springer: 1984.

(119) Shen, F.; Pompano, R. R.; Kastrup, C. J.; Ismagilov, R. F. Confinement Regulates Complex Biochemical Networks: Initiation of Blood Clotting by "Diffusion Acting". *Biophys. J.* **2009**, *97*, 2137–2145.

(120) Tang, J.; Yao, C.; Gu, Z.; Jung, S.; Luo, D.; Yang, D. Super-Soft and Super-Elastic DNA Robot with Magnetically Driven Navigational Locomotion for Cell Delivery in Confined Space. *Ang. Chem. Int. Ed.* **2020**, *59*, 2490–2495.

(121) Grotberg, J. B. Respiratory fluid mechanics. *Phys. Fluids* **2011**, *23*, 021301.

(122) Desgranges, C.; Delhommelle, J. Nucleation of Capillary Bridges and Bubbles in Nanoconfined CO_2. *Langmuir* **2019**, *35*, 15401–15409.

(123) Leenders, S. H. A. M.; Gramage-Doria, R.; de Bruin, B.; Reek, J. N. H. Transition metal catalysis in confined spaces. *Chem. Soc. Rev.* **2015**, *44*, 433–448.

(124) Guo, C.; Xiao, J. Towards unifying the concepts of catalysis in confined space. *Comput. Mat. Sci.* **2019**, *161*, 58–63.

(125) Andronescu, C.; Masa, J.; Tilley, R. D.; Gooding, J. J.; Schuhmann, W. Electrocatalysis in confined space. *Curr. Opin. Electrochem.* **2021**, *25*, 100644.

(126) Shifa, T. A.; Vomiero, A. Confined Catalysis: Progress and Prospects in Energy Conversion. *Adv. Energy Mat.* **2019**, *9*, 1902307.

(127) Sing, K. S. W. Reporting physisorption data for gas/solid systems with special reference to the determination of surface area and porosity (Recommendations 1984). *Pure Appl. Chem.* **1985**, *57*, 603–619.

(128) Coudert, F.-X. Microscopic structure of a zeolite (mordenite) framework `https://en.wikipedia.org/wiki/Zeolite#/media/File:Zeolite_structure_as_an_assembly_of_tetrahedra.png` (accessed 11/20/2021).

(129) Lin, C. C. H.; Dambrowitz, K. A.; Kuznicki, S. M. Evolving applications of zeolite molecular sieves. *Can. J. of Chem. Eng.* **2012**, *90*, 207–216.

(130) Prieto, M. J.; Klemm, H. W.; Xiong, F.; Gottlob, D. M.; Menzel, D.; Schmidt, T.; Freund, H.-J. Water Formation under Silica Thin Films: Real-Time Observation of a Chemical Reaction in a Physically Confined Space. *Ang. Chem. Int. Ed.* **2018**, *57*, 8749–8753.

(131) Lewandowski, A. L.; Tosoni, S.; Gura, L.; Yang, Z.; Fuhrich, A.; Prieto, M. J.; Schmidt, T.; Usvyat, D.; Schneider, W.-D.; Heyde, M.; Pacchioni, G.; Freund, H.-J. Growth and Atomic-Scale Characterization of Ultrathin Silica and Germania Films: The Crucial Role of the Metal Support. *Chem. Eur. J.* **2021**, *27*, 1870–1885.

(132) Hutchings, G. S.; Jhang, J.-H.; Zhou, C.; Hynek, D.; Schwarz, U. D.; Altman, E. I. Epitaxial NixPd1–x (111) Alloy Substrates with Continuously Tunable Lattice Constants for 2D Materials Growth. *ACS App. Mat. Interfaces* **2017**, *9*, 11266–11271.

(133) Shekunov, B. Kinetics of Crystallization and Glass Transition in Amorphous Materials. *Cryst. Growth Des.* **2020**, *20*, 95–106.

(134) Koch, M.; Jakob, P.; Menzel, D. The influence of steps on the water-formation reaction on Ru(001). *Surf. Sci.* **1996**, *367*, 293–306.

(135) Prieto, M. J.; Mullan, T.; Schlutow, M.; Gottlob, D. M.; Tănase, L. C.; Menzel, D.; Sauer, J.; Usvyat, D.; Schmidt, T.; Freund, H.-J. Insights into Reaction Kinetics in Confined Space: Real Time Observation of Water Formation under a Silica Cover. *J. Am. Chem. Soc.* **2021**, *143*, 8780–8790.

(136) Held, G.; Menzel, D. Isotope effects in structure and kinetics of water adsorbates on Ru(001). *Surf. Sci.* **1995**, *327*, 301–320.

(137) Meyer, B.; Private Communication.

(138) Arblaster, J. Crystallographic Properties of Ruthenium. *Platin. Met. Rev.* **2013**, *57*, 127–136.

(139) Yang, B.; Kaden, W.; Yu, X.; Boscoboinik, J.; Martynova, Y.; Lichtenstein, L.; Heyde, M.; Sterrer, M.; Włodarczyk, R.; Sierka, M.; Sauer, J.; Shaikhutdinov, S.; Freund, H.-J. Thin silica films on Ru(0001): monolayer, bilayer and three-dimensional networks of SiO_4 tetrahedra. *Phys. Chem. Chem. Phys.* **2012**, *14*, 11344–11351.

(140) Hafner, J. Ab-initio simulations of materials using VASP: Density-functional theory and beyond. *J. Comput. Chem.* **2008**, *29*, 2044–2078.

(141) Giannozzi, P. et al. QUANTUM ESPRESSO: a modular and open-source software project for quantum simulations of materials. *J. Phys. Condens. Matt.* **2009**, *21*, 395502.

(142) Monkhorst, J.; Pack, D. Special points for Brillouin-zone integrations. *Phys. Rev. B* **1976**, *13*, 5188–5192.

(143) Henkelman, G.; Uberuaga, B. P.; Jónsson, H. A climbing image nudged elastic band method for finding saddle points and minimum energy paths. *J. Chem. Phys.* **2000**, *113*, 9901–9904.

(144) Henkelman, G.; Jónsson, H. A dimer method for finding saddle points on high dimensional potential surfaces using only first derivatives. *J. Chem. Phys.* **1999**, *111*, 7010–7022.

(145) Feulner, P.; Menzel, D. The adsorption of hydrogen on ruthenium (001): Adsorption states, dipole moments and kinetics of adsorption and desorption. *Surf. Sci.* **1985**, *154*, 465–488.

(146) Jeffrey, H.; Scott, T.; Manos, M. Atomic and molecular adsorption on Ru(0001). *Surf. Sci.* **2013**, *614*, 64–74.

(147) Stampfl, C.; Scheffler, M. Theoretical study of O adlayers on Ru(0001). *Phys. Rev. B: Cond. Matt.* **1996**, *54*, 2868–2872.

(148) Michaelides, A.; Alavi, A.; King, D. Different Surface Chemistries of Water on Ru{0001}: From Monomer Adsorption to Partially Dissociated Bilayers. *J. Am. Chem. Soc.* **2003**, *125*, 2746–2755.

(149) Marin, G., *Kinetics of chemical reactions: decoding complexity*; Wiley-VCH: Weinheim, Germany, 2019.

(150) Prieto, M. J.; Mullan, T.; Wana, W.; Tănasea, L. C.; de Souza Caldasa, L.; Shaikhutdinova, S.; Sauer, J.; Usvyat, D.; Schmidt, T.; Cuenya, B. R. Plasma functionalization of silica bilayer polymorphs (submitted). *ACS Appl. Mater. Interfaces* **2022**.

(151) Ren, B.; Wang, Y.; Ou, J. Z. Engineering two-dimensional metal oxides via surface functionalization for biological applications. *J. Mat. Chem. B* **2020**, *8*, 1108–1127.

(152) Rimola, A.; Costa, D.; Sodupe, M.; Lambert, J.-F.; Ugliengo, P. Silica Surface Features and Their Role in the Adsorption of Biomolecules: Computational Modeling and Experiments. *Chem. Rev.* **2013**, *113*, 4216–4313.

(153) Wang, L.; Guan, E.; Wang, Y.; Wang, L.; Gong, Z.; Cui, Y.; Meng, X.; Gates, B. C.; Xiao, F.-S. Silica accelerates the selective hydrogenation of CO_2 to methanol on cobalt catalysts. *Nature Commun.* **2020**, *11*, 1033.

(154) Wachs, I. E. Catalysis science of supported vanadium oxide catalysts. *Dalton Trans.* **2013**, *42*, 11762–11769.

(155) Saleh, R. Y.; Wachs, I. E.; Chan, S. S.; Chersich, C. C. The interaction of V_2O_5 with TiO_2 (anatase): Catalyst evolution with calcination temperature and O-xylene oxidation. *J. Catal.* **1986**, *98*, 102–114.

(156) Haber, J.; Machej, T.; Czeppe, T. The phenomenon of wetting at solid/solid interface. *Surf. Sci.* **1985**, *151*, 301–310.

(157) Haber, J.; Machej, T.; Serwicka, E. M.; Wachs, I. E. Mechanism of surface spreading in vanadia-titania system. *Catal. Lett.* **1995**, *32*, 101–114.

(158) Feher, F. J.; Walzer, J. F. Synthesis and characterization of vanadium-containing silsesquioxanes. *Inorg. Chem.* **1991**, *30*, 1689–1694.

(159) Sauer, J.; Döbler, J. Structure and reactivity of V_2O_5: bulk solid, nanosized clusters, species supported on silica and alumina, cluster cations and anions. *Dalton Trans.* **2004**, 3116–3121.

(160) Duval, Y.; Mielczarski, J. A.; Pokrovsky, O. S.; Mielczarski, E.; Ehrhardt, J. J. Evidence of the Existence of Three Types of Species at the Quartz–Aqueous Solution Interface at pH 0–10: XPS Surface Group Quantification and Surface Complexation Modeling. *J. Phys. Chem. B* **2002**, *106*, 2937–2945.

(161) Brown, M. A.; Beloqui Redondo, A.; Sterrer, M.; Winter, B.; Pacchioni, G.; Abbas, Z.; van Bokhoven, J. A. Measure of Surface Potential at the Aqueous–Oxide Nanoparticle Interface by XPS from a Liquid Microjet. *Nano Lett.* **2013**, *13*, 5403–5407.

(162) Yu, X.; Emmez, E.; Pan, Q.; Yang, B.; Pomp, S.; Kaden, W. E.; Sterrer, M.; Shaikhutdinov, S.; Freund, H.-J.; Goikoetxea, I.; Wlodarczyk, R.; Sauer, J. Electron stimulated hydroxylation of a metal supported silicate film. *Phys. Chem. Chem. Phys.* **2016**, *18*, 3755–3764.

(163) Methfessel, M.; Paxton, A. T. High-precision sampling for Brillouin-zone integration in metals. *Phys. Rev. B* **1989**, *40*, 3616–3621.

(164) Löffler, D.; Uhlrich, J. J.; Baron, M.; Yang, B.; Yu, X.; Lichtenstein, L.; Heinke, L.; Büchner, C.; Heyde, M.; Shaikhutdinov, S.; Freund, H.-J.; Włodarczyk, R.; Sierka, M.; Sauer, J. Growth and Structure of Crystalline Silica Sheet on Ru(0001). *Phys. Rev. Lett.* **2010**, *105*, 146104.

(165) Fournier, R. P.; Savoie, R.; The, N. D.; Belzile, R.; Cabana, A. Vibrational Spectra of SiH_4 and SiD_4–SiH_4 Mixtures in the Condensed States. *Can. J. Chem.* **1972**, *50*, 35–42.

(166) Hu, W.; Lin, L.; Yang, C. DGDFT: A massively parallel method for large scale density functional theory calculations. *J. Chem. Phys.* **2015**, *143*, 124110.

(167) Sato, F.; Shigemitsu, Y.; Okazaki, I.; Yahiro, S.; Fukue, M.; Kozuru, S.; Kashiwagi, H. Development of a new density functional program for all-electron calculation of proteins. *Int. J. Quantum Chem.* **1997**, *63*, 245–256.

(168) Oliphant, N.; Bartlett, R. J. A systematic comparison of molecular properties obtained using Hartree–Fock, a hybrid Hartree–Fock density-functional-theory, and coupled-cluster methods. *J. Chem. Phys.* **1994**, *100*, 6550–6561.

(169) Chang, T. C.; Habitz, P.; Pittel, B.; Schwarz, W. H. E. Accuracy and limitations of the pseudopotential method. *Theor. Chim. Acta* **1974**, *34*, 263–275.

(170) Karttunen, A. J.; Usvyat, D.; Schütz, M.; Maschio, L. Dispersion interactions in silicon allotropes. *Phys. Chem. Chem. Phys.* **2017**, *19*, 7699–7707.

(171) Usvyat, D.; Maschio, L.; Schütz, M. Periodic and fragment models based on the local correlation approach. *WIREs Comput. Mol. Sci.* **2018**, *8*, e1357.

(172) Grüneis, A.; Marsman, M.; Harl, J.; Schimka, L.; Kresse, G. Making the random phase approximation to electronic correlation accurate. *J. Chem. Phys.* **2009**, *131*, 154115.

(173) Ladik, J. J., *Quantum Theory of Polymers as Solids*; Springer Science & Business Media: Berlin Heidelberg, 2012.

(174) Sun, J.-Q.; Bartlett, R. J. Second-order many-body perturbation-theory calculations in extended systems. *J. Chem. Phys.* **1996**, *104*, 8553–8565.

(175) Hirata, S.; Iwata, S. Analytical energy gradients in second-order Møller–Plesset perturbation theory for extended systems. *J. Chem. Phys.* **1998**, *109*, 4147–4155.

(176) Ayala, P. Y.; Kudin, K. N.; Scuseria, G. E. Atomic orbital Laplace-transformed second-order Møller–Plesset theory for periodic systems. *J. Chem. Phys.* **2001**, *115*, 9698–9707.

(177) Del Ben, M.; Hutter, J.; VandeVondele, J. Second-Order Møller–Plesset Perturbation Theory in the Condensed Phase: An Efficient and Massively Parallel Gaussian and Plane Waves Approach. *J. Chem. Theory Comput.* **2012**, *8*, 4177–4188.

(178) Del Ben, M.; Hutter, J.; VandeVondele, J. Electron Correlation in the Condensed Phase from a Resolution of Identity Approach Based on the Gaussian and Plane Waves Scheme. *J. Chem. Theory Comput.* **2013**, *9*, 2654–2671.

(179) Del Ben, M.; Hutter, J.; VandeVondele, J. Forces and stress in second order Møller-Plesset perturbation theory for condensed phase systems within the resolution-of-identity Gaussian and plane waves approach. *J. Chem. Phys.* **2015**, *143*, 102803.

(180) Booth, G. H.; Tsatsoulis, T.; Chan, G. K.-L.; Grüneis, A. From plane waves to local Gaussians for the simulation of correlated periodic systems. *J. Chem. Phys.* **2016**, *145*, 084111.

(181) McClain, J.; Sun, Q.; Chan, G. K.-L.; Berkelbach, T. C. Gaussian-Based Coupled-Cluster Theory for the Ground-State and Band Structure of Solids. *J. Chem. Theory Comput.* **2017**, *13*, 1209–1218.

(182) Stoll, H. Correlation energy of diamond. *Phys. Rev. B* **1992**, *46*, 6700–6704.

(183) Stoll, H. The correlation energy of crystalline silicon. *Chem. Phys. Lett.* **1992**, *191*, 548–552.

(184) Stoll, H. On the correlation energy of graphite. *J. Chem. Phys.* **1992**, *97*, 8449–8454.

(185) Lee, S. J. R.; Welborn, M.; Manby, F. R.; Miller, T. F. Projection-Based Wavefunction-in-DFT Embedding. *Acc. Chem. Res.* **2019**, *52*, 1359–1368.

(186) Manby, F. R.; Stella, M.; Goodpaster, J. D.; Miller, T. F. A Simple, Exact Density-Functional-Theory Embedding Scheme. *J. Chem. Theory Comput.* **2012**, *8*, 2564–2568.

(187) Alessio, M.; Bischoff, F. A.; Sauer, J. Chemically accurate adsorption energies for methane and ethane monolayers on the MgO(001) surface. *Phys. Chem. Chem. Phys.* **2018**, *20*, 9760–9769.

(188) Tuma, C.; Sauer, J. Treating dispersion effects in extended systems by hybrid MP2:DFT calculations—protonation of isobutene in zeolite ferrierite. *Phys. Chem. Chem. Phys.* **2006**, *8*, 3955–3965.

(189) Alessio, M.; Usvyat, D.; Sauer, J. Chemically Accurate Adsorption Energies: CO and H_2O on the MgO(001) Surface. *J. Chem. Theory Comput.* **2019**, *15*, 1329–1344.

(190) Kirsch, H.; Wirth, J.; Tong, Y.; Wolf, M.; Saalfrank, P.; Campen, R. K. Experimental Characterization of Unimolecular Water Dissociative Adsorption on α-Alumina. *J. Phys. Chem. C* **2014**, *118*, 13623–13630.

(191) Dovesi, R.; Orlando, R.; Erba, A.; Zicovich-Wilson, C. M.; Civalleri, B.; Casassa, S.; Maschio, L.; Ferrabone, M.; De La Pierre, M.; D'Arco, P.; Noël, Y.; Causà, M.; Rérat, M.; Kirtman, B. CRYSTAL14 : A program for the ab initio investigation of crystalline solids. *Int. J. Quantum. Chem.* **2014**, *114*, 1287–1317.

(192) Dunning, T. H. Gaussian basis sets for use in correlated molecular calculations. I. The atoms boron through neon and hydrogen. *J. Chem. Phys.* **1989**, *90*, 1007–1023.

(193) Wolinski, K.; Pulay, P. Second-order Møller–Plesset calculations with dual basis sets. *J. Chem. Phys.* **2003**, *118*, 9497–9503.

(194) Kendall, R. A.; Dunning, T. H.; Harrison, R. J. Electron affinities of the first-row atoms revisited. Systematic basis sets and wave functions. *J. Chem. Phys.* **1992**, *96*, 6796–6806.

(195) Usvyat, D.; Civalleri, B.; Maschio, L.; Dovesi, R.; Pisani, C.; Schütz, M. Approaching the theoretical limit in periodic local MP2 calculations with atomic-orbital basis sets: The case of LiH. *J. Chem. Phys.* **2011**, *134*, 214105.

(196) Peterson, K. A.; Dunning, T. H. Accurate correlation consistent basis sets for molecular core–valence correlation effects: The second row atoms Al–Ar, and the first row atoms B–Ne revisited. *J. Chem. Phys.* **2002**, *117*, 10548–10560.

(197) Yang, J.; Chan, G. K.-L.; Manby, F. R.; Schütz, M.; Werner, H.-J. The orbital-specific-virtual local coupled cluster singles and doubles method. *J. Chem. Phys.* **2012**, *136*, 144105.

(198) Usvyat, D.; Maschio, L.; Schütz, M. Periodic local MP2 method employing orbital specific virtuals. *J. Chem. Phys.* **2015**, *143*, 102805.

(199) Usvyat, D. Linear-scaling explicitly correlated treatment of solids: Periodic local MP2-F12 method. *J. Chem. Phys.* **2013**, *139*, 194101.

(200) Manby, F. R.; Knowles, P. J. Poisson Equation in the Kohn-Sham Coulomb Problem. *Phys. Rev. Lett.* **2001**, *87*, 163001.

(201) Manby, F. R.; Knowles, P. J.; Lloyd, A. W. The Poisson equation in density fitting for the Kohn-Sham Coulomb problem. *J. Chem. Phys.* **2001**, *115*, 9144–9148.

(202) Manby, F., *Accurate condensed-phase quantum chemistry*; CRC Press: Boca Raton, FL, 2011.

(203) Wilson, A. K.; Dunning Jr., T. H. Benchmark calculations with correlated molecular wave functions. X. Comparison with "exact" MP2 calculations on Ne, HF, H2O, and N2. *J. Chem. Phys.* **1997**, *106*, 8718–8726.

(204) Werner, H.-J. et al. The Molpro quantum chemistry package. *J. Chem. Phys.* **2020**, *152*, 144107.

(205) Knowles, P. J.; Handy, N. C. A determinant based full configuration interaction program. *Comput. Phys. Comm.* **1989**, *54*, 75–83.

(206) Kats, D.; Manby, F. R. Communication: The distinguishable cluster approximation. *J. Chem. Phys.* **2013**, *139*, 021102.

(207) Kats, D. Improving the distinguishable cluster results: spin-component scaling. *Mol. Phys.* **2018**, *116*, 1435–1442.

(208) Kirsch, H.; Wirth, J.; Tong, Y.; Wolf, M.; Saalfrank, P.; Campen, R. K. Experimental Characterization of Unimolecular Water Dissociative Adsorption on α-Alumina. *J. Phys. Chem. C* **2014**, *118*, 13623–13630.

(209) Dirac, P.; Dalitz, R., *The Collected Works of P. A. M. Dirac: Volume 1: 1924-1948*; The Collected Works of P.A.M. Dirac; Cambridge University Press: 1995.